Dopamine signals integrate innate and learnt valences to regulate memory dynamics

Mark Schnitzer (mschnitz@stanford.edu)
HHMI / Stanford University https://orcid.org/0000-0002-1431-8533
Cheng Huang
https://orcid.org/0000-0001-9936-4813
Junjie Luo
Stanford University
Seung Je Woo
Stanford University
Lucas Roitman
Stanford University
Jizhou Li
Stanford University
Vincent Pieribone
Pierce Laboratory
Madhuvanthi Kannan
John Pierce Laboratory/ Yale University
Ganesh Vasan
John Pierce Laboratory/ Yale University

Biological Sciences - Article

Keywords:

Posted Date: August 11th, 2022

DOI: https://doi.org/10.21203/rs.3.rs-1915648/v1

Dopamine signals integrate innate and learnt valences to regulate memory dynamics

Cheng Huang[1,2*†], Junjie Luo[1,3†], Seung Je Woo[1], Lucas A. Roitman[1], Jizhou Li[3,4,#], Vincent A. Pieribone[5,6], Madhuvanthi Kannan[5,6*], Ganesh Vasan[5,6*], and Mark J. Schnitzer[1–4,7*]

[1]*James Clark Center,* [2]*Department of Biology,* [3]*Howard Hughes Medical Institute,*
[4]*CNC Program, Stanford University, Stanford, CA, USA.*
[5]*The John B. Pierce Laboratory,* [6]*Department of Cellular and Molecular Physiology, Yale University, New Haven, CT, USA.*
[7]*Department of Applied Physics, Stanford University, Stanford, CA, USA.*

[†]*These authors contributed equally to this work.*

[#]*Present address: Stanford Synchrotron Radiation Lightsource, SLAC National Accelerator Laboratory, Menlo Park, CA, USA.*

***Correspondence: huangch@stanford.edu; mschnitz@stanford.edu; m.kannan@yale.edu; g.vasan@yale.edu**

To survive in dynamic environments, animals make behavioral decisions based on innate and learnt information about the valences of sensory cues. In the brains of multiple species, innate and learnt sensory valence signals are initially encoded by distinct neural populations[1–7] but then reconverge in downstream brain structures that guide behavioral choices[6–9]. This reconvergence hinges on the prior acquisition of learnt valence information, which in turn might depend upon innate valence signals. However, it remains unknown whether and how innate sensory valence cues shape the acquisition of learnt valence information. Here we show that in the fruit fly brain, interactions between innate and learnt sensory valence signals within interconnected short- and long-term memory units of the mushroom body jointly regulate memory formation and expression via modulation of dopamine teaching signals. By using time-lapse, *in vivo* optical voltage imaging to record

neural spiking with millisecond-resolution in flies undergoing olfactory associative conditioning, we found that PPL1 dopamine neurons (PPL1-DANs) heterogeneously and bi-directionally encode punishment, reward, and innate and learnt odor-valence cues. Learning modulates these representations in a way that combines innate and learnt valence information and allows the PPL1-DANs to regulate memory storage in their downstream targets, mushroom body output neurons (MBONs). PPL1-γ1pedc and PPL1-γ2α'1 neurons control short-term memory formation. After repeated conditioning, feedback signals carrying short-term memory data from MBON-γ1pedc>α/β to PPL1-α'2α2 and PPL1-α3 allow these dopamine cells to encode previously learnt valences and promote long-lasting memory formation. A computational model constrained by the mushroom body connectome and our spiking data explains how dopamine signals integrate innate and learnt valence data to regulate memory storage, extinction, and the interactions between short- and long-term memory traces. The model yields non-intuitive predictions about the effects of different training protocols, which our experiments confirm. Overall, the mushroom body achieves flexible learning through dopamine-mediated integration of innate and learnt valences in parallel sets of DAN/MBON learning units with feedback interconnections. This hybrid physiologic-anatomic mechanism may be a general means by which ecological information regulates learning and memory in other species and brain structures relying on dopaminergic signaling, including the vertebrate basal ganglia[10].

Introduction

When navigating changing environments, animals evaluate the innate valences of sensory cues against learnt valence information acquired from past experiences. Innate valence data convey predictions, such as about predatory threats or food sources, that are usually trustworthy and

often vital to survival. Learnt valence information arises through experiences that modify a sensory cue's innate valence[11]. In many species, innate and learnt valence data are processed by distinct neural pathways, an arrangement that may benefit the reliability and flexibility of animal behavior[1–7]. For example, in flies and mice, early-stage olfactory centers send odor information to separate higher-order centers that control innate and learnt behaviors; these are, respectively, the lateral horn and mushroom body in the fly brain[7,12,13] and the olfactory amygdala and piriform cortex in the mouse brain[1,2,4,14]. However, it remains unknown whether innate valence data also shape the acquisition of learnt valence information, and, if so, what functional benefits this interaction between innate and learnt data might provide.

One plausible way by which innate valence data could modulate learning is via dopamine teaching signals that may carry both innate and learnt information. Mammalian dopamine neurons (DANs) often respond to reward-predicting cues and signal reward prediction errors that encode the discrepancies between expected and received rewards[15–18]. However, some DANs encode the novelty or identities of unfamiliar cues, showing that the mammalian learning system represents certain innate facets of sensory cues[16,19–21].

Likewise, in *Drosophila*, the dopamine learning system also processes innate and learnt valence data. Two distinct clusters of DANs (PPL1 and PAM) send negative and positive reinforcement signals, respectively, to the mushroom body (MB) where they drive learning[22,23]. For instance, the co-activation of DANs and MB Kenyon cells receiving odor information induces olfactory learning via synaptic plasticity in compartmentalized MB axonal regions[24,25]. However, as in mammals, the DANs respond to more than just aversive or rewarding stimuli. Notably, in naïve flies, most DANs respond to odor cues[20,26–28], and some respond preferentially

to attractive or repulsive odors[26]. These innate odor responses may be driven, at least in part, by both Kenyon cell inputs and feedback signals coming from within the MB itself[29,30,31].

Supporting this idea, the connections between DANs and MB output neurons (MBONs) form a parallel-recurrent circuit comprising multiple learning units working in parallel but with widespread recurrent feedback[22,29,30] (**Fig. 1a**). This architecture implies that multiple memory traces exist in parallel across the different learning units. In each learning unit, a single or small cluster of DANs selectively controls plasticity in one or a few MB compartments. However, no learning unit works in isolation, since the DANs also receive recurrent feedback signals from the MBONs that convey learnt valence information[8,29,30,32]. This combination of parallel processing and recurrence is striking and naturally prompts the hypothesis that the DANs integrate innate valence signals coming from the sensory system (via the MB) together with learnt valence data stored in memory (by the MBONs).

Here, we tested this hypothesis by using a chronic preparation for long-term *in vivo* optical voltage imaging in behaving flies[33]. Unlike neural Ca^{2+} imaging[34], voltage imaging reports individual action potentials with millisecond-resolution and bi-directional modulations of neural spiking (*i.e.*, both excitations and suppressions of spiking)[35,36]. This approach enabled us to study how PPL1-DAN teaching signals encode and integrate innate and learnt valence cues and to uncover how this valence integration allows short-term memories to shape the formation of long-term memories via recurrent feedback signals within the MB. We then constructed and tested a computational model of the parallel-recurrent MB circuitry by using recent data on the connectivity of the MB and our imaging data to constrain the model's structure and dynamics. Notably, this model and its multiple interesting predictions could not have been attained through Ca^{2+} imaging, as declines in spiking activity below baseline levels are crucial in the model but

poorly reported via Ca^{2+} dynamics. Altogether, our results reveal how innate valence information regulates memory dynamics and how the integration of innate and learnt valences within dopamine signals leads to complex interactions between short- and long-term memory traces.

Long-term voltage imaging of neural spiking with 1-ms-resolution in behaving flies

To observe neural spiking dynamics in the PPL1-DAN/MBON circuit with sub-millisecond resolution, nearly all of our studies used a novel indicator, pAce, in the FRET-opsin class of fluorescent protein voltage indicators[37,38]. Like the widely used FRET-opsin, Ace-mNeon[37], pAce is a fusion of the *Acetabularia* rhodopsin and mNeonGreen, but, unlike Ace-mNeon, pAce has a positive voltage-sensitivity and responds to membrane polarization by increasing its fluorescence emissions[39]. To identify short- (<3 hr) and long-lasting (>24 hr) neural plasticity, we sought to image odor-evoked neural dynamics before, during, and at least 24 hr after an olfactory associative conditioning. Thus, we first needed to establish experimental protocols for long-term voltage imaging in awake behaving flies[33,40,41] (**Fig. 1a,b; Movie 1; Methods**). For these initial validations and all subsequent studies, we used a set of split-GAL4 fly lines[22] that allowed us to express pAce in 11 different neuron-types, namely 5 subtypes of PPL1-DANs (PPL1-γ1pedc, -γ2α’1, -α’2α2, -α3 and -α’3) and 6 subtypes of downstream MBONs (MBON-γ1pedc>α/β, -γ2α’1, -α2sc, -α’2, -α3 and -α’3) (**Extended Data Fig. 1a–i**; **Extended Data Table 1**).

Using these fly lines and high-speed (1 kHz) imaging of MB compartments innervated by PPL1-DANs axons and MBON dendritic arbors, we first recorded spontaneous activity in all 11 neuron-types at single-spike resolution (**Fig. 1c; Extended Data Fig. 1a–i**). Across all 11 neuron-types, the PPL1-DANs and MBONs showed variable rates of spontaneous spiking and bursting (**Fig. 1d,e**). To characterize the reliability of spike detection in the different cell-types, we used the spike detection fidelity, d', a signal detection theory metric that is often used to

assess voltage imaging performance[37,42] (**Methods**). Using pAce, PPL1-DANs exhibited *d′* values of 7.1–9.5, implying spike-detection error rates of 0.04–0.2 s^{-1} (**Extended Data Fig. 1j,k**). MBONs had *d′* values of 5.0–8.4 and inferred spike-detection error rates of 0.06–1.8 s^{-1}. MBON-γ2α'1, MBON-α'2, and MBON-α'3m had lower *d′* values than other MBONs and PPL1-DANs (**Extended Data Fig. 1j,k**), most likely due to previously identified differences in the peak depolarization levels of action potentials in the different MBON-types[24] (**Fig. 1f**). Notably, in MBONs, there were backpropagating spikes that traveled retrogradely from axonal regions into the dendritic arbors (**Extended Data Fig. 2; Movie 2**). Further investigation of these retrograde signals was outside the scope of our study, but they might facilitate spike-timing dependent plasticity, as do backpropagating spikes in mammalian neurons[43,44].

PPL1 dopamine cells encode innate valences in a heterogeneous, bi-directional manner.

To characterize the coding properties of PPL1-DANs, we tracked their evoked responses to various sensory stimuli, including punishment (electric shock), reward (sugar water), and a range of aversive, attractive and neutral odors. Electric-shock pulses to the fly thorax elevated the spiking rates of PPL1-γ1pedc, -γ2α'1 and -α3 neurons after shock onset; spike rates then gradually declined after shock offset (**Fig. 2a**). During a shock, spike rates of PPL1-γ1pedc, -γ2α'1 and -α3 cells rose respectively to 307% ± 52%, 364% ± 49%, and 157% ± 23% of their baseline rates (mean ± s.e.m.; **Fig. 2b**). However, the firing rates of PPL1-α'2α2 and -α'3 were unchanged during shocks (**Fig. 2b**).

Next, we tested how PPL1-DANs respond to sucrose intake, which is widely used for reward-based, appetitive conditioning[45–47]. In contrast to the spiking excitation induced in PPL1-DANs by electric shocks, when the fly's proboscis contacted sucrose water and initiated feeding, spiking was suppressed in the PPL1-γ1pedc, PPL1-γ2α'1, -α'2α2 and -α3 neurons (**Fig.**

2c). Their spike rates during the 5-s sucrose exposure declined significantly to 82% ± 5%, 49% ± 6%, 74% ± 5% and 62% ± 7% of their baseline values (mean ± s.e.m.; **Fig. 2d**).

To study the relationship between the innate valence of an odor and its neural representation, we tested flies' behavioral odor preferences while also imaging the odor-evoked spiking dynamics of PPL1-DAN and MBON neurons. As a fly walked or ran in place on a trackball with two degrees of rotational freedom, we delivered odors from either the front left or front right side of the fly. In response to each odor, flies typically made approaching or avoidance movements by changing their walking direction either towards or away from the odor (**Fig. 2e,f**). In particular, we found a set of 5 odors that collectively induced behavioral responses ranging from vigorous approach to vigorous avoidance (**Fig. 2g,h; Extended Data Fig. 3b,c**). The nearly evenly spaced set of evoked behavioral responses suggests that these 5 odors have a corresponding, evenly spaced set of innate odor valences.

Using the same 5 odors, we next tracked odor-evoked spiking in PPL1-DANs and their downstream MBONs. Strikingly, unlike the odor-evoked patterns of neural excitation that have been reported in prior Ca^{2+}-imaging studies in flies[25,26,48], voltage imaging showed that PPL1-DANs have either excitatory or inhibitory innate responses to odor presentation (**Extended Data Fig. 3a**). Similarly to the flies' odor-evoked behavioral responses, 4 types of PPL1-DANs showed corresponding, bi-directional spiking changes that ranged from excitation to inhibition (**Fig. 2i; Extended Data Fig. 3d–g**). An exception was PPL1-α'3 DAN, which showed chiefly excitatory responses (**Extended Data Fig. 3h**). By comparison, the downstream MBONs uniformly showed odor-evoked excitation, with response amplitudes that were independent of innate odor valences (**Extended Data Fig. 4**), in accord with past results from Ca^{2+} imaging[49].

Notably, cells in the two subsets, PPL1-DANs and MBONs, had odor-evoked responses that were strongly correlated across the 5 odors tested to the responses of other cell-types in the same subset, but negatively correlated to those of cells in the other subset (**Fig. 2j**). An exception was the MBON-α2sc neuron, whose odor-evoked responses closely resembled those of the PPL1-DANs (**Fig. 2j**). Further, the mean odor-evoked firing rates of PPL1-DANs were strongly correlated to the flies' behavioral responses to the same odors, with the exception of PPL1-α'3 (**Fig. 2j,k**). The odor-evoked spiking responses of MBONs were more variable across animals and more weakly correlated with the flies' behavioral responses (**Fig. 2j,k**).

To evaluate and compare odor representations in PPL1-DANs and MBONs, we conducted a classification analysis using the odor-evoked spiking rates measured across these two neural populations (**Methods**). The responses of both cell populations enabled successful odor categorization at above-chance rates; this shows that each cell population signals information about odor identity or valence, although PPL1-DAN signals enabled greater classification accuracies than those of MBONs (**Fig. 2l**). Overall, PPL1-DANs exhibited accurate, bi-directional representations of innate odor-valence at the single cell and population levels. This contrasts with the variable and limited coding capacities of MBONs[49], notwithstanding that both MBONs and PPL1-DANs receive olfactory signals from the same sets of MB Kenyon cells[29].

Learning induces distributed and bidirectional plasticity in PPL1-DANs and MBONs.

Recent connectomic and computational studies of the adult fly brain suggest that PPL1-DANs receive both direct and indirect feedback inputs from downstream MBONs[29,30,50–54]. These feedback connections may have important roles in shaping the predictive, dopaminergic teaching signals that guide learning and MB plasticity. To probe the neural changes in the MB that

influence learning, we developed an olfactory aversive conditioning paradigm for head-fixed flies that could walk in place on a trackball as we performed high-speed voltage imaging of neural activity (**Methods**). Like the traditional T-maze learning assay for flies[47,55–57], our assay involved 6 training bouts, each with sequential exposures to a pair of conditioned (CS^+ and CS^-) odors; to induce associative conditioning, in each training bout we paired CS^+ odor delivery with an electric shock to the fly (**Fig. 3a–e**). To capture the time course of learning, we measured the fly's behavioral or neural responses to the CS^+ and CS^- at multiple time points before, during and after conditioning—instead of assessing the fly's conditioned response at only one time-point as in the classic T-maze assay[55]. After conditioning with CS^+ and CS^- odors that were both initially attractive (apple cider vinegar and 1% ethyl acetate), flies reduced their approaches towards the CS^+ but not the CS^- odor; this CS^+-specific reduction lasted ≥1 hr (**Fig. 3b,c**).

Next, we systematically evaluated how neural spiking responses were altered by aversive, associative conditioning using CS^+ and CS^- odors that were both initially attractive. CS^--evoked responses in all 5 PPL1-DANs were statistically unaltered by conditioning (**Fig. 3f; Extended Data Fig. 5**). However, the CS^+-evoked responses of PPL1-α'2α2 and -α3 evolved across 3–6 training bouts from inhibitory to excitatory and then back to their initial inhibitory forms after 1 h of rest (**Fig. 3f**). The CS^+-evoked responses of PPL1-γ1pedc remained inhibitory at all time-points, with significant amplitude changes at 5 min but not 1 hr after conditioning, whereas the responses of PPL1-γ2α'1 and -α'3 were unaffected by conditioning (**Fig. 3f**). At each testing time-point, we calculated the differences in the spiking rates induced by CS^+ and CS^- odors, normalized these values to the pre-training responses in each individual fly, and termed the resultant the 'relative CS^+/CS^- bias' index (**Methods**). This bias index resembles the two-way choice index that is commonly used to characterize flies' responses in the T-maze behavioral

assay[55]. The bias index showed that, after training, spiking responses became biased to the CS^+ odor in PPL1-α'2α2 and -α3 but not in PPL1-γ1pedc, -γ2α'1 and -α'3 (**Fig. 3f**).

Unlike the DANs, after training the MBONs-γ1pedc>α/β and -γ2α'1 showed decreased CS^+-evoked responses (**Fig. 3e,g**; **Extended Data Fig. 6**), which returned to baseline values after 1 hr of rest, consistent with prior electrophysiological recordings[19]. In contrast, MBON-α3 exhibited decreased CS+-evoked responses for at least 1 hr after conditioning. However, in MBON-α2sc, -α'2 and -α'3m neurons, odor-induced spiking was statistically unchanged by training (**Fig. 3g; Extended Data Fig. 6**).

MBON-α3 plasticity is crucial for long-lived memory and depends on innate odor valence. Prior behavioral studies have suggested that the γ and α compartments of the MB have distinct roles in the regulation of short- and long-term memories[23,58–62]. To assess the duration of learning-induced plasticity, we performed voltage-imaging at 3 hr, 24 hr and 48 hr after associative conditioning. The resulting data revealed that conditioning led to a short-lasting depression (<1 hr duration) of the CS^+-evoked responses of the γ MBONs, as well as a long-lasting depression of the CS^+-evoked responses of MBON-α3 that persisted for >3 hr and in some flies for 24–48 hr (**Extended Data Fig. 7a**). To test the necessity of this long-lasting plasticity for long-lasting memory, we used the tetanus toxin light chain (TnT)[63] to block synaptic vesicle release from MBON-α3; this impaired memory performance at 3 hr but not 5 min post-training, showing the selective importance of MBON-α3 for long-lasting memory (**Extended Data Fig. 7b–e**).

Next, we examined how innate odor valences influence the long-lasting plasticity in MBON-α3 by comparing flies trained with an attractive CS^+/CS^- odor pair (ACV and 1% EtA) to those trained with repulsive odors (1% OCT and 0.3% BEN) (**Fig. 4a–d**). In flies trained with

attractive odors, after 3 training bouts the CS^+-evoked responses of MBON-α3 switched from spiking increases to spiking decreases, which became further pronounced after another 3 bouts of training (**Fig. 4a,c**). This spiking plasticity gradually decayed with time but still remained at 24 hr after training. By comparison, CS^--evoked responses remained stable throughout (**Fig. 4a,c**). In accord with these results, after training the CS^+/CS^- bias index was significantly below its pre-training level for all post-conditioning time points, except at 24 hr afterward (**Fig. 4c**).

Notably, MBON-α3 plasticity was very different in flies trained with repulsive odor pairs. CS^+ and CS^- presentations both evoked marked suppressions of spiking after only 3 training bouts, and these effects persisted for at least 3 hr (**Fig. 4b,d**). CS^+ presentations induced significant suppressions of spiking even at 24 hr post-conditioning, whereas CS^--evoked responses became excitatory again by 3 hr post-conditioning, albeit not at baseline levels (**Fig. 4b,d**). Due to the concurrent declines in CS^+- and CS^-- evoked responses, the CS^+/CS^- response bias was unchanged until 24 hr after training (**Fig. 4d**). Taken together with the results obtained using attractive odor pairs, these findings show that innate odor valence greatly influences MBON-α3 spiking dynamics and plasticity.

Feedback from MBON-γ1pedc>α/β to PPL1-α3 sculpts long-lasting plasticity in MBON-α3.

To better understand the plasticity of MBON-α3, we studied the dopamine teaching signals it receives from PPL1-α3 that bi-directionally signal punishment, reward, and both innate and learnt odor valences (**Fig. 2b,d,i; Fig. 3f**). First, we tested how PPL1-α3 responds to pairs of concurrently presented sensory stimuli with valences of either the same or opposite sign. Paired presentations of electric shocks (5× 0.2-s pulses; 0.5 Hz; 60V) and odor (10-s-presentations of either attractive ACV or repulsive 1% OCT) evoked PPL1-α3 spiking dynamics that combined the responses elicited by the odor or shocks individually (**Fig. 4e–h**). The onset and offset times

of the odor presentation, as well as the pulsatile spiking responses to the individual shock pulses, were all visible in the spiking responses to the paired presentations (**Fig. 4e,g**). The presence of attractive odor reduced the mean spiking rate evoked by the shock pulses, whereas repulsive odor had the opposite effect, and the magnitudes of these effects were consistent with PPL1-α3 linearly summing its responses to the individual stimuli (**Fig. 4e–h**). These observations suggest that spiking and dopamine teaching signals from PPL1-α3 convey the net valence of jointly presented stimuli, which explains why associative conditioning with attractive versus repulsive odor pairs leads to very different plasticity in MBON-α3.

The finding that PPL1-α3 conveys the net valence of two concurrently presented stimuli led us to consider the possible circuit mechanisms that shape how PPL1-α3 encodes valence. The neural connectome of the adult fly brain[30] shows that PPL1-α3 receives inhibitory feedback from the GABAergic MBON-γ1pedc>α/β neuron, excitatory feedback from the cholinergic MBON-α2sc and MBON-α3 neurons, and a glutamatergic feedback signal from the MBON-β1>α neuron that is putatively inhibitory[64]. We hypothesized that, among these feedback connections, the inhibitory feedback from MBON-γ1pedc>α/β was likely to have a central role in the regulation of innate and learnt odor-valence coding by PPL1-α3. The main clue motivating this hypothesis was the observation that the learning-induced depression in MBON-γ1pedc>α/β's odor-evoked responses and the short-lasting potentiation of PPL1-α3's odor-evoked responses seem matched in duration (**Fig. 3f,g**). This temporal concordance is consistent with the idea that a depression of the inhibitory feedback from MBON-γ1pedc>α/β disinhibits PPL1-α3's odor-evoked responses.

We first tested this idea in the context of innate valence coding by using RNAi to downregulate the expression of the GABA-A receptor in PPL1-α3. This manipulation disrupted

the dynamic range and bi-directional coding of innate odor valence in PPL1-α3 (**Extended Data Fig. 8a–d**). Odor-evoked spiking was generally increased, especially for attractive odors (**Extended Data Fig. 8e**), whereas spontaneous spiking was unaltered (**Extended Data Fig. 8f**).

Next, we tested the role of feedback inhibition from MBON-γ1pedc>α/β in the context of associative conditioning. We used two distinct expression systems (GAL/UAS and LexA/LexAop) to block neurotransmission from MBON-γ1pedc>α/β as we imaged PPL1-α3's spiking dynamics during training with attractive odors (**Fig. 4i**). With MBON-γ1pedc>α/β signaling blocked, PPL1-α3 exhibited slight increases in spiking in response to odor presentation, and these spiking responses were unaffected by training (**Fig. 4j**). These results stand in sharp contrast to those from control flies, which exhibited the normal reduction in PPL1-α3 spiking in response to attractive odors and temporary conversion of these responses to odor-evoked spiking increases after associative conditioning (**Fig. 4k**). These results suggest that, during learning, the rapidly induced depression of CS^+-evoked responses in MBON-γ1pedc>α/β increases the CS^+-evoked responses of PPL1-α3, which in turn shape the formation of long-lasting plasticity in MBON-α3 and therefore long-lasting memory.

To test this interpretation, we used optogenetic excitation of MBON-γ1pedc>α/β to artificially maintain its inhibitory feedback signals at a high level during conditioning with an attractive odor pair (**Fig. 4l**). Although the control groups showed reduced attraction to the CS^+ odor at 5-min and 3-hr after training (**Fig. 4m,n**), flies in which MBON-γ1pedc>α/β was activated during conditioning had a subsequent, selective memory impairment at 3 hr after training (**Fig. 4m**). This delayed memory impairment shows that removal of the strong feedback from MBON-γ1pedc>α/β is indeed crucial for the formation of a long-lasting memory.

A computational model captures valence integration and memory trace interactions.

To capture the interaction dynamics of innate and learnt valence signals, we created a computational model with 3 interconnected DAN/MBON learning modules (γ1, α2, and α3) that exhibited both short- and long-term plasticity (**Methods; Fig. 5a**), jointly constrained by the fly connectome[30] and our voltage-imaging results. We excluded DANs and MBONs in the γ2 and α'3 modules as well as the MBON-α'2 neuron from the model, because they do not directly connect to the 3 interconnected learning modules.

The model has 9 different types of neurons (open circles; **Fig. 5a**): Dγ1, Dα2, Dα3, Mγ1, Mα2, and Mα3, which respectively represent PPL1-γ1pedc, PPL1-α'2α2, PPL1-α3, MBON-γ1pedc>α/β, MBON-α2sc, and MBON-α3; Kenyon cells (KC1 and KC2) that receive olfactory CS^+ and CS^- signals and transmit them to downstream DANs and MBONs via KC→DAN and KC→MBON connections; and a shock-sensing neuron (SN) that sends electric shock-related input to Dγ1 and Dα3. The DANs integrate this shock-related input with olfactory signals arriving via the KC→DAN connections and feedback signals sent via the MBON→DAN connections. We set the signs of the various neural inputs according to the neurotransmitters used in actuality by each neuron.

To depict neural plasticity in the MB, the concurrent activation of a KC and its postsynaptic DAN in the model modifies the synaptic weight of the KC→MBON connection according to an anti-Hebbian learning rule (**Supplementary Appendix; Fig. 5b**). The initial connection strengths of the KC→DAN and MBON→DAN connections determine the innate representations of odor valence in the DANs. The learning-induced changes of the KC→MBON weights allow learnt valence information to influence DAN dynamics via the MBON→DAN feedback inputs. To determine the values of all model parameters, including those setting the

rates of plasticity, we optimized the model to fit our voltage-imaging measurements of neural spike rates across multiple time points in the learning process (**Supplementary Appendix; Fig. 5c; Extended Data Fig. 9a,b**).

We first assessed how the innate valences of hypothetical odors influence plasticity and the efficiency of learning in the 3 different MBONs of the model. We quantified the innate valence of each hypothetical odor via the change in DAN spiking that it evoked prior to conditioning; thus, hypothetical odors that inhibited spiking were considered attractive, whereas those that increased spiking represented repulsive odors. As in our real experiments, we studied associative conditioning using odors of equal innate valences prior to conditioning. After a single bout of associative conditioning, all 3 model MBONs exhibited plasticity in their responses to both CS^+ and CS^- odors. Simulated conditioning with attractive odors led to a weak depression or even a potentiation of the odor-evoked responses of all 3 MBONs. Simulated conditioning with repulsive odors led to more substantial depressions of odor-evoked MBON spiking (**Fig. 5d**). Consistent with these initial findings of innate valence-dependent conditioning, the model exhibited valence-dependent plasticity dynamics across the immediate 24 hr after 6 bouts of conditioning. This valence dependence was especially notable in the dynamics of the CS^+ *vs.* CS^- response biases of MBON-α2sc and -α3 (**Extended Data Fig. 9c; Extended Data Fig. 10**). Thus, in the model, as in the empirical results, innate odor valences regulate the efficiency of neural plasticity.

Next, we explored how learnt odor valences in the model influence subsequent bouts of conditioning. As in our experiments, we were particularly interested in the role of inhibitory feedback from MBON-γ1pedc>α/β to the DANs. We used the bias of CS^+- and CS^--evoked MBON spiking as a measure of plasticity, and we determined bias values in the model after

varying numbers of training bouts (3–15) in the presence or absence of the MBON-γ1pedc>α/β feedback (**Fig. 5e**). In the absence of this feedback, plasticity in MBON-γ1pedc>α/β fell by only 3–9%, but in MBON-α2sc it was fully eliminated (**Fig. 5e**). In MBON-α3, there were time-dependent plasticity effects; a lack of feedback from MBON-γ1pedc>α/β reduced plasticity by 0.1–27% at 15-min after conditioning and by 33–58% at 3 hr after conditioning (**Fig. 5f**). Thus, in the model as in the real data, previously learnt odor valences facilitate the formation of long-lasting plasticity in MBON-α3 owing to feedback signals from MBON-γ1pedc>α/β.

In addition to replicating key experimental findings, the model also yielded several unexpected but experimentally testable predictions. First, the model predicted that the magnitudes of learning-induced depressions in MBONs should depend on the inter-stimulus interval (ISI) between conditioning stimuli; this prediction resembles the 'spacing effect' that has been observed in many memory tasks and animal species, such that learning protocols that are repeated at greater temporal separations are more effective in inducing long-term memories[65]. In our model, when we increased the training ISI from 60 s to 900 s, the amplitude of short-term (5-min) depression in MBON-γ1pedc>α/β gradually declined. Moreover, the model exhibited a striking ISI-dependence of plasticity in MBON-α2sc and MBON-α3 at 3 hr and 24 hr after conditioning, with the greatest levels of plasticity induced by an ISI of about 360 s (**Fig. 5g; Extended Data Fig. 9d**). This effect was greatest in MBON-α3 and depended upon the MBON-γ1pedc>α/β feedback (**Extended Data Fig. 9e,f**). To test this prediction of the model, we verified experimentally that 6 bouts of training using an ISI of 360 s induced significantly stronger depression at 24-hr depression in MBON-α3 than training with an ISI of 60 s (**Fig. 5h**), showing the embodiment of the 'spacing effect' within the neural activity of the long-term memory module of the MB.

The model also predicted that the extinction of plasticity in MBON-α3 should depend on innate odor valence as well as the elapsed time since conditioning. After repeated pairings of odor and shock, the CS^+-evoked responses of PPL1-α3 in the model initially increased but then gradually faded away by 1 hr after conditioning. In other words, within the first hour after conditioning, the CS^+ has not only been associated with the US within the short-term learning unit but also acts like a reinforcer in the long-term learning units (**Extended Data Fig. 10c,e**). Consequently, re-exposures to the CS^+ and CS^- odors at different time points after conditioning differentially influenced the plasticity of MBON-α3 (**Fig. 5i,j; Extended Data Fig. 9g**). For simulated attractive odors, extinction sessions starting within 30 min after training led to little to no effect on MBON-α3 plasticity levels, whereas extinction sessions that started at 60 min or longer after training successfully erased the training-induced depression in MBON-α3 (**Fig. 5j; Extended Data Fig. 9g; Extended Data Fig. 11**). This effect depended on the feedback from MBON-γ1pedc>α/β (**Extended Data Fig. 9g**). In contrast, for simulated repulsive odors, extinction sessions led to only modest and transient changes in the CS^+ *vs.* CS^- response bias of MBON-α3 that recovered soon afterward (**Fig. 5j; Extended Data Fig. 9g; Extended Data Fig. 11**). To test these predictions, we experimentally measured the CS^+ *vs.* CS^- response biases of conditioned flies that received no extinction sessions and those of flies that had extinction sessions at 10 min or 2 h after conditioning. The results were strikingly consistent with those from the model and revealed both the predicted valence- and time-dependent aspects of extinction (**Fig. 5k**). Overall, the model's quantitative, non-intuitive predictions that are experimentally verifiable show the power of jointly using voltage-imaging and connectomic data to construct neural circuit models whose dynamics capture essential features of learning and memory.

Discussion

Our results show that the fly MB uses a dopamine-based valence integration mechanism to actively modulate the efficiency of memory formation and extinction. The impact is most pronounced for the regulation of long-term memories, which makes sense from a functional perspective, as it helps reserve long-lasting memories (which may be costly energetically[66]) for associations that may be highly reliable and occur frequently in an animal's environment.

To enable this active regulation of memory, dopamine signals from PPL1-DANs encode the summed value of jointly presented stimuli. This net value comprises innate and learnt valences and can be positive or negative, contrary to prior descriptions of PPL1-DANs that emphasized their signaling of negatively-valued stimuli[67–70]. During initial cycles of associative conditioning, PPL1-DANs sum the innate valences of both the cue and the reinforcer; this leads to depression of KC→MBON connections, especially in the faster-acting, short-term (γ1 and γ2) learning units of the MB. The use of the net valence as the teaching signal limits learning about contradictory cue-reinforcer associations that may not be ecologically reliable—*e.g.* an innately attractive cue paired with a punishment—since such pairings evoke smaller dopamine signals that are less effective at driving KC→MBON plasticity. Whereas, pairing an innately aversive cue with a punishment will evoke greater dopamine signals that drive greater plasticity levels.

After repeated conditioning cycles, attenuation of feedback inhibition from the γ1 short-term learning unit allows the PPL1-DANs of the slower-acting, long-term (α2 and α3) learning units to undergo a short-lived potentiation of their sensory-evoked responses, which encodes the acquired valence of the CS^+ and promotes the formation of long-lasting memory traces in the α2 and α3 compartments. Thus, the MB circuit architecture enacts a feedback by which short-term memory traces gate the formation of long-term memory traces, thereby

ensuring that only repeated and reliable associations induce stable long-lasting memories. Future work should test if the PAM-DAN/MBON system, which has mainly been implicated in the learning of rewarding associations[23,71,72], operates according to analogous principles.

While our data show the importance of sensory cues' innate valences to memory formation, it remains unclear how PPL1-DANs gain their representations of innate odor valence. Multiple neuron-types send olfactory data to PPL-DANs, including MB anterior paired lateral neurons, olfactory projection neurons, Kenyon cells and MBONs[22,29,30,32], suggesting innate valence coding might arise from an elegant balance of multiple excitatory and inhibitory inputs.

Longstanding conceptions of dopamine-driven learning in the mammalian brain posit that dopamine teaching signals convey reward prediction errors[15–18]. Recent work suggests that dopamine may also encode information about value[73], not just errors in value prediction. Most models of dopamine-based learning in the *Drosophila* MB involve synaptic plasticity rules in which plasticity of KC→MBON connections is gated by coincident activations of KC and DAN neurons in the same MB compartment[74–76]. Several models also incorporate reward prediction error signaling via MBON→DAN feedback connections[8,50–52]. However, no prior model has fully explained MB neural dynamics or provided quantitative, testable predictions.

Our computational model is constrained by the fly connectome plus our spike imaging data. It quantitatively captures the dynamics of 3 MB compartments, makes novel predictions, reveals key features of the parallel-recurrent PPL1-DAN/MBON learning system, and incorporates a hybrid of two different dopamine-mediated learning rules. First, there is a coincidence-based learning rule that operates within a fast-acting, short-term (γ1) learning module; within this module, dopamine signaling is not changed across learning. Second, there is a prediction-driven learning rule that operates within two slower-acting, long-term (α2 and α3)

learning modules; in these modules, dopamine signals rise over repeated cycles of conditioning to convey the learnt valence of the CS^+. The model shows how the joint encoding of innate and learnt valences in the long-term memory units shapes memory dynamics, yielding non-intuitive predictions about long-lasting plasticity that we subsequently verified experimentally.

First, the model predicts that long-lasting plasticity is enhanced when association events are spaced at certain optimal time intervals, rather than massed in quick succession. This 'spacing effect' has been observed in behavioral studies of many different memory tasks[77–79] and animal species[80,81], including *Drosophila*[56,82]. Our modeling and imaging results reveal a neural embodiment of this 'spacing effect' and open the door to finer dissections of its underlying mechanisms. Second, the model shows that the successful extinction of long-lasting plasticity depends on both the timing of extinction bouts and the innate valence of the sensory cue. Illustrating this point, in flies that had been conditioned with attractive odors, the timing of subsequent unpaired re-exposures to the CS^+ odor strongly influenced the level of plasticity in MBON-α3 at 3 hr after conditioning, such that extinction bouts at 10 min but not 2 hr after conditioning were ineffective. This difference in efficacy arises from a dynamic competition between the innate appetitive and learnt aversive odor valences, which are both encoded by PPL1-α3 but at relative amplitudes that vary over time and different phases of learning.

Notably, in contrast to prior models of the MB[8,50–54,83], our model could not have been constructed based on Ca^{2+} imaging data. Unlike Ca^{2+} imaging[34], voltage imaging allows high-fidelity detection of individual action potentials and reports rises and declines in spiking equally well[35,36]. Using FRET-opsin voltage indicators[39], we uncovered the decreases in PPL1-DAN spiking evoked by attractive odors and food rewards, neither of which had been seen in Ca^{2+} imaging studies[25,26]. Our own Ca^{2+} imaging studies did reveal the encoding of stimulus

valence by PPL1-DANs, but the Ca^{2+} responses poorly reported spiking decreases and the encoding of net valences when two stimuli were present concurrently (**Extended Data Fig. 12a–h**). Thus, constructing our model based directly on observations of neural spiking was important for the model to be able to provide its quantitative, empirically verifiable predictions.

Overall, the parallel-recurrent DAN/MBON learning system uses dopamine-based valence integration to dynamically regulate memory formation and extinction in a way that accounts for both the innate and learnt valences of sensory stimuli. Within the MB circuitry, the interactions between sensory data, a heterogeneous set of dopamine teaching signals, and both short- and long-term memory traces collectively allow complex memory dynamics to emerge (**Extended Data Fig. 12i**). The resulting stored memories guide downstream circuits to enact efficient and flexible decision-making over multiple time-scales. Given the many facets of dopamine-based learning systems that were preserved across evolution, the circuit and computational mechanisms used by the MB may provide key insights into how heterogenous dopamine signaling within recurrent neural architectures, such as in the vertebrate basal ganglia[10], shape learning and memory dynamics in other species.

Acknowledgements

We gratefully acknowledge research grants from the NIH BRAIN Initiative (U01NS120822; MJS, GV) and the NSF NeuroNex Program (DBI-1707261; MJS, K. Deisseroth). We thank J. Li, Y. Gong, J. Savall and S. Sinha for technical assistance. We thank the Janelia Research Campus, R. Davis (Scripps Institute), and D. Anderson (Caltech) for gifts of fly strains.

Figure 1

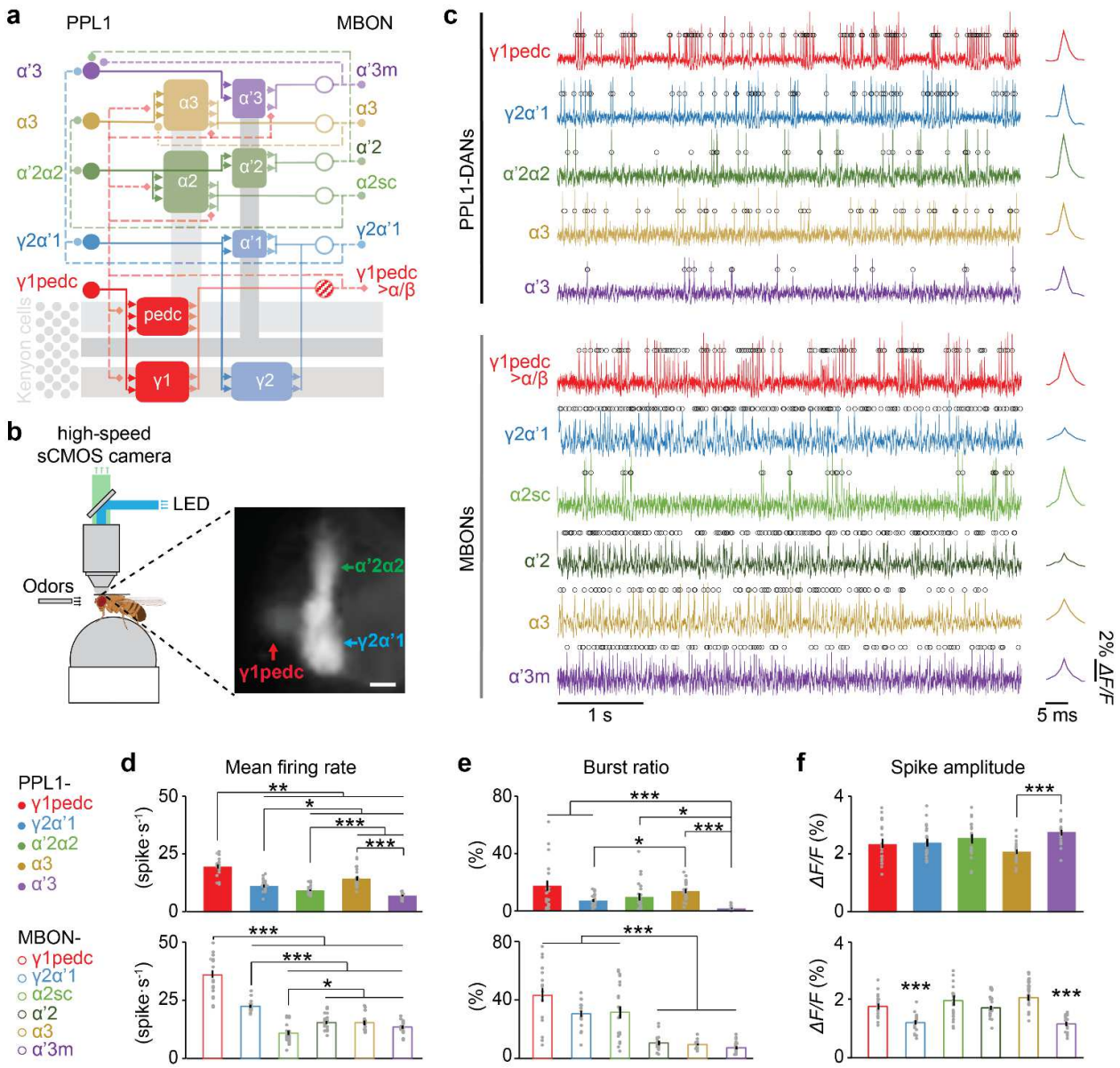
a
PPL1
MBON
α'3
α3
α'2α2
γ2α'1
γ1pedc
Kenyon cells
α3
α'3
α2
α'2
α'1
pedc
γ1
γ2
α'3m
α3
α'2
α2sc
γ2α'1
γ1pedc >α/β
b
high-speed sCMOS camera
LED
Odors
α'2α2
γ2α'1
γ1pedc
c
PPL1-DANs
γ1pedc
γ2α'1
α'2α2
α3
α'3
MBONs
γ1pedc >α/β
γ2α'1
α2sc
α'2
α3
α'3m
1 s
5 ms
2% ΔF/F
PPL1-
γ1pedc
γ2α'1
α'2α2
α3
α'3
MBON-
γ1pedc
γ2α'1
α2sc
α'2
α3
α'3m
d
Mean firing rate
(spike·s⁻¹)
e
Burst ratio
(%)
f
Spike amplitude
ΔF/F (%)

Fig. 1 | *In vivo* voltage imaging of PPL1-DANs and downstream MBONs in *Drosophila*.

a) A diagram of PPL1-DAN/MBON connectivity, showing the parallel-recurrent structure. The 5 PPL1-DANs innervate 8 compartments, synapse onto MB axons, and thereby modulate the 6 downstream MBONs. 5 parallel learning modules are shown in different colors. Kenyon cells and their axons are shown in gray. Solid lines indicate feedforward connections; dashed lines indicate feedback connections.

b) *Left,* Schematic of the high-speed optical voltage imaging setup for awake behaving flies. The flies are free to walk or run on a trackball, which records their locomotor responses before, during and after odor delivery. *Right,* A mean fluorescence image, averaged over 15 s of a voltage movie, showing the pAce voltage indicator expressed in the PPL1-γ1pedc, -γ2α'1, and -α'2α2, neurons (*MB504C-GAL4* fly line). Scale bar: 10 μm.

c) *Left,* Example optical voltage traces from live flies, showing spontaneously fired action potentials in individual PPL1-DANs and MBONs. Black open circles mark identified spikes. *Right,* Mean optical waveforms for the spikes in each individual cell.

d–f) Mean firing rates, **d**, spontaneous burst ratios, **e**, and optical spike amplitudes, **f**, from PPL1-DANs (*top graphs*) and MBONs (*bottom graphs*). Burst ratio was computed as the number of spikes occurring <20 ms after the preceding spike, divided by the total number of spikes in the trial. Data are shown as mean ± s.e.m. Gray dots denote data from individual flies. Kruskal-Wallis ANOVA showed that all 6 graphs exhibited significant differences across neuron-types (n = 20 flies per neuron-type). Horizontal lines and asterisks mark specific pairwise comparisons that yielded significant differences in post-hoc Mann-Whitney U-tests performed with a Holm-Bonferroni correction for multiple comparisons (*P<0.05, **P<0.01, and ***P<0.001).

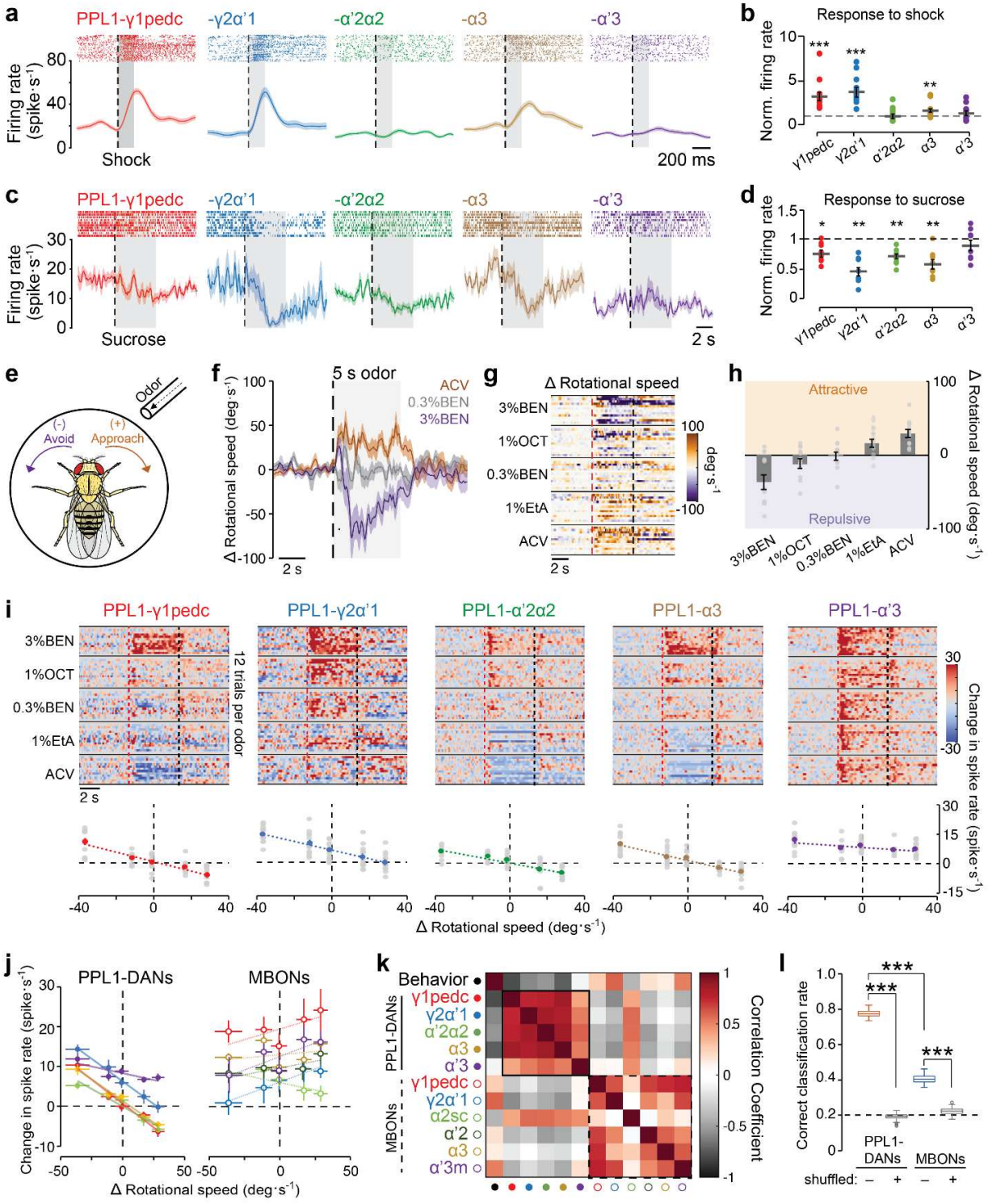
a
PPL1-γ1pedc
-γ2α'1
-α'2α2
-α3
-α'3
Firing rate (spike·s⁻¹)
Shock
200 ms
b
Response to shock
Norm. firing rate
γ1pedc
γ2α'1
α'2α2
α3
α'3
c
Sucrose
2 s
d
Response to sucrose
e
Odor
(-) Avoid
(+) Approach
f
5 s odor
ACV
0.3%BEN
3%BEN
Δ Rotational speed (deg·s⁻¹)
g
Δ Rotational speed
3%BEN
1%OCT
0.3%BEN
1%EtA
ACV
deg·s⁻¹
h
Attractive
Repulsive
i
PPL1-γ1pedc
PPL1-γ2α'1
PPL1-α'2α2
PPL1-α3
PPL1-α'3
12 trials per odor
Change in spike rate (spike·s⁻¹)
Δ Rotational speed (deg·s⁻¹)
j
PPL1-DANs
MBONs
k
Behavior
γ1pedc
γ2α'1
α'2α2
α3
α'3
α2sc
α'2
α'3m
Correlation Coefficient
l
Correct classification rate
PPL1-DANs
MBONs
shuffled: – + – +

Fig. 2 | PPL1-DANs heterogeneously and bidirectionally encode punishment, reward, and odor valence.

a) *Top*, Raster plots of spiking by individual PPL1-DANs on 36 different trials (n = 12 flies per neuron-type, 3 trials per fly) on which the fly received a 20-V-electric shock. Vertical dashed line: shock onset. Gray shading covers the 200-ms-duration of the shock. *Bottom,* Traces showing the time-dependent mean spiking rates before, during and after the shock, averaged over all 36 trials. Shading on the time traces: s.e.m.

b) Mean spiking rates of each type of PPL1-DAN during the 200-ms-electric-shock, normalized to the baseline rates of spiking in the same individual neurons. Dashed horizontal line denotes baseline spiking rates ($y = 1$). (Data are shown as mean ± s.e.m.; $^{**}P<0.01$, $^{***}P<0.001$; n = 12 flies per neuron-type; Wilcoxon signed-rank test comparison of the shock-evoked to baseline spiking rates in each neuron).

c) *Top*, Raster plots of spiking by individual PPL1-DANs on 10 different trials (n = 10 flies per neuron-type, 1 trial per fly) on which the fly received a 5 s sucrose feeding. Vertical dashed line: Onset of sucrose availability. Gray shading covers the 5-s-duration of the feeding. *Bottom,* Traces showing the time-dependent mean spiking rates before, during and after feeding, averaged over all 10 trials. Shading on the time traces: s.e.m.

d) Mean spiking rates of each type of PPL1-DAN during the 5-s-sucrose-feeding, normalized to the baseline rates of spiking in the same individual neurons. Dashed horizontal line denotes baseline spiking rates ($y = 1$). (Data are shown as mean ± s.e.m.; $^{*}P<0.05$, $^{**}P<0.01$; n = 10 flies per neuron-type; Wilcoxon signed-rank test comparison of the feeding-evoked to baseline spiking rates in each neuron).

e) A schematic showing the measurement of a fly's odor-evoked behavioral responses using a

trackball. We delivered odors to the fly's antenna at a 45 deg. angle in the horizontal plane. The sign and amplitude of the fly's evoked rotational motion indicate either approach behavior to an odor of positive valence or avoidance behavior in response to an odor of negative valence.

f) Mean changes in rotational speed of wild-type flies (w^{1118}) in response to 3 different odors (either apple cider vinegar (ACV) or 0.3% or 3% benzaldehyde dissolved in mineral oil), each presented for a duration of 5 s. Shading on the time traces: s.e.m. over 36 total trials in 12 flies. Dashed vertical line: onset of odor delivery. Gray shading covers the duration of odor delivery.

g) Fly's rotational responses to odor delivery. Each row in the plot shows an individual fly's change in rotational speed (averaged over 3 trials per odor; plotted using 50-ms time bins and smoothed with a rolling averaging over 6 time bins) for the 5 specific odors shown (n = 12 flies). Dashed lines mark odor delivery onset (*red line*) and offset (*black line*). 1%OCT: 1% 3-octanol in mineral oil. 1%EtA: 1% ethyl acetate in mineral oil. In this plot and panel **i**, odors are arranged from top to bottom progressing from the most aversive to the most appetitive odor, respectively.

h) Mean ± s.e.m. changes in rotational speed in response to the same 5 odors as in **g**, averaged over the 5 s of odor presentation and 36 trials per odor (n = 12 flies, 3 trials per fly). Individual points denote data from individual flies. Odor data are plotted in order from left to right on the *x*-axis from the most repulsive to the most attractive odor.

i) *Top*, Odor-evoked changes in spike rates in PPL1-DANs, relative to the mean baseline spiking rate on each trial (averaged over the 5 s on each trial prior to odor delivery; n =12 flies, 1 trial per odor per fly). Dashed lines mark odor delivery onset (*red line*) and offset (*black line*). *Bottom*, Scatter plots of the mean ± s.e.m. changes in spike rates measured during odor exposure (5 s duration) relative to baseline spike rates (data and flies from above graphs), plotted as a function

of the mean ± s.e.m. odor-induced changes in rotational speed (data and flies of **h**. Gray circles show data from individual flies. As in **h**, odor data are plotted from left to right on the *x*-axis from the most repulsive to the most attractive odor. Dashed lines are linear regressions (R = 0.79, 0.72, 0.77, 0.8 and 0.40 for PPL1-γ1pedc, -γ2α'1, -α'2α2, -α3 and -α'3 respectively; $P = 1 \times 10^{-14}$–2×10^{-3}). **Extended Data Fig. 4** has comparable data for the MBONs.

j) Odor-evoked behavior *vs.* odor-evoked neural activity tuning curves for the different types of PPL1-DANs (*left*) and MBONs (*right*), with the data for each cell-type shown in a distinct color (colors are the same as those in panel **k**). Each data point is for a given odorant. As in **h** and **i**, odor data are plotted from left to right on the *x*-axis from the most repulsive to the most attractive odor. Mean odor-induced changes in neural spiking rate (*y*-axis) for each cell-type and odorant are plotted against the flies' mean changes in rotational speed induced by the same odorant (*x*-axis). Solid and dashed lines: Linear regressions for PPL1-DANs and MBONs, respectively. Error bars: s.e.m.; n = 12 flies per cell-type; R = 0.99, 0.99, 0.97, 0.99, 0.85 for PPL1-γ1pedc, -γ2α'1, -α'2α2, -α3 and -α'3 respectively, $P = 3 \times 10^{-4}$–0.07; R = 0.73, 0.97, 0.78, 0.81, 0.29, 0.82 for MBON-γ1pedc>α/β, -γ2α'1, -α2sc, -α'2, -α3 and -α'3m, respectively; P = 0.005–0.64).

k) A 12 × 12 matrix of correlation coefficients, computed across the different neuron-types using either each of the 11 neuron-types' mean odor-evoked responses to the same 5 odors used in panel **i**, or the flies' mean rotational response to each of the 5 odors (data from panel **h**).

l) To estimate the extent to which a fly might be able to distinguish the different odorants used in our study based solely on the odor-evoked patterns of neural activity across the 5 PPL1-DANs or 6 MBONs, we performed a classification analysis using a collection of neural recordings from 117 total flies, in which the dynamics of each neuron-type was recorded in 12 different flies (Some fly lines allowed us to record from more than 1 cell-type at once; **Methods**; **Extended**

Data Table 1). The box-and-whisker plot shows the accuracy of odor classification using the set of mean odor-evoked changes in neural activity across either the 5 PPL1-DANs or the 6 MBONs. Notwithstanding that there are fewer PPL1-DANs than MBONs, odor classification was significantly more accurate based on PPL1-DAN activity patterns. We compared the results to those attained using shuffled datasets, in which odor identities were randomly permuted. Boxes span the 25th–75th percentiles, horizontal lines denote median values, whiskers span 1.5 times the interquartile distance, and circles are outlier data points. Gray dashed line indicates chance level (***$P < 0.001$; Wilcoxon ranked sum test).

Figure 3

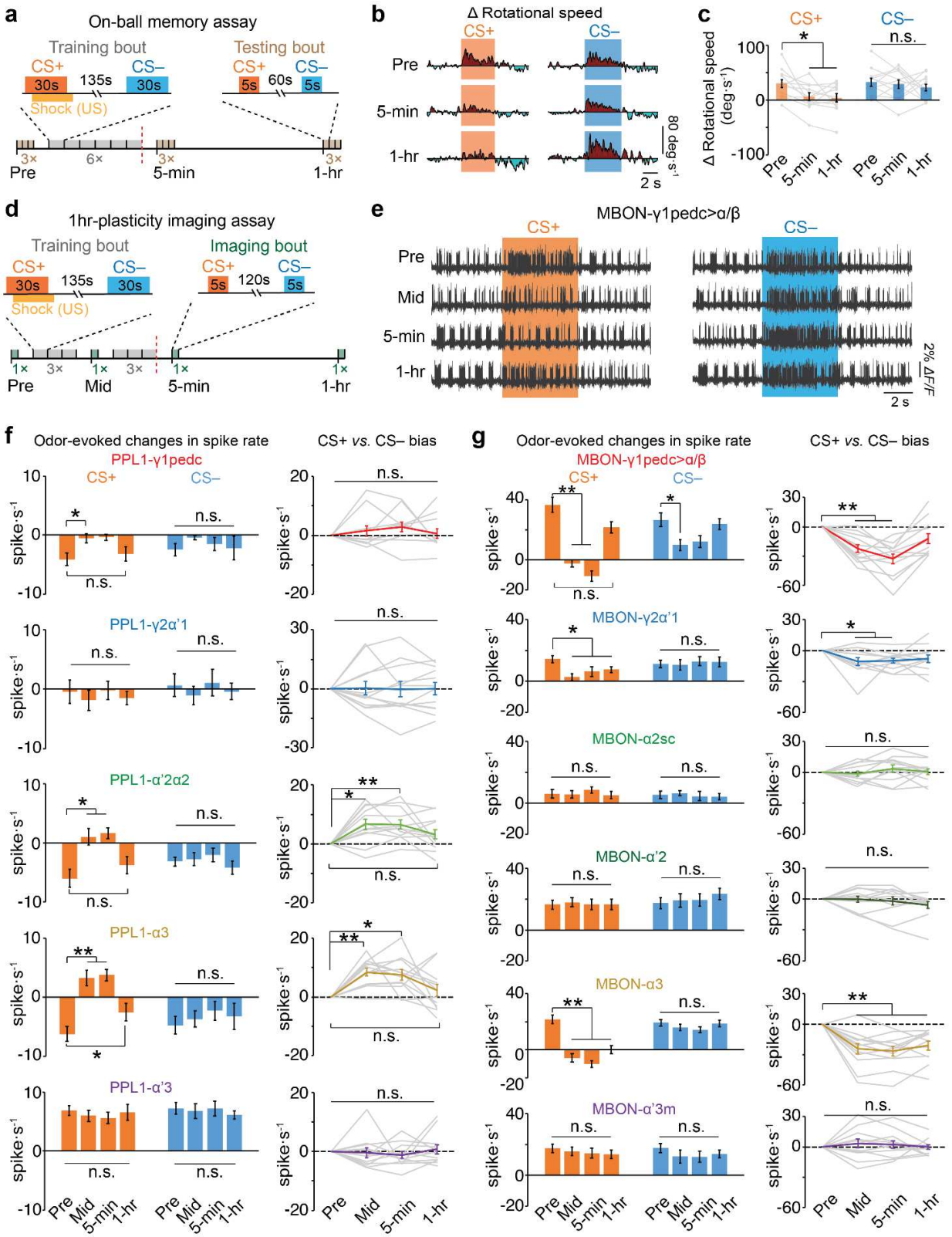
a
On-ball memory assay
Training bout
Testing bout
CS+
CS–
30s
135s
30s
Shock (US)
5s
60s
5s
3×
6×
3×
3×
Pre
5-min
1-hr
b
Δ Rotational speed
CS+
CS–
Pre
5-min
1-hr
80 deg·s⁻¹
2 s
c
CS+
CS–
*
n.s.
Δ Rotational speed (deg·s⁻¹)
100
0
-100
Pre
5-min
1-hr
Pre
5-min
1-hr
d
1hr-plasticity imaging assay
Training bout
Imaging bout
CS+
CS–
30s
135s
30s
Shock (US)
5s
120s
5s
1×
3×
1×
3×
1×
1×
Pre
Mid
5-min
1-hr
e
MBON-γ1pedc>α/β
CS+
CS–
Pre
Mid
5-min
1-hr
2% ΔF/F
2 s
f
Odor-evoked changes in spike rate
CS+ vs. CS– bias
PPL1-γ1pedc
PPL1-γ2α'1
PPL1-α'2α2
PPL1-α3
PPL1-α'3
spike·s⁻¹
n.s.
*
**
Pre
Mid
5-min
1-hr
g
Odor-evoked changes in spike rate
CS+ vs. CS– bias
MBON-γ1pedc>α/β
MBON-γ2α'1
MBON-α2sc
MBON-α'2
MBON-α3
MBON-α'3m
CS+
CS–
spike·s⁻¹
n.s.
*
**
Pre
Mid
5-min
1-hr

Fig. 3 | Learning induces distributed, bidirectional neural plasticity in PPL1-DANs and MBONs.

a) *Bottom,* Timeline for our behavioral assay of olfactory associative learning and memory, for head-fixed awake flies on a trackball. Each fly first underwent 3 bouts of odor-testing before conditioning (Pre), in which we examined the animal's initial behavioral responses to the 2 odors to be used during conditioning (CS^+ and CS^-). Next, we subjected each fly to 6 bouts of training, in each of which the fly received a paired presentation of the CS^+ and the unconditioned stimulus (US, a pulse-train of electric shocks), plus an unpaired presentation of the CS^-. At 5 min after the end of the last training bout, each fly underwent 3 bouts of testing to assess its odor-evoked behavioral responses post-conditioning. At 1 hr after the end of training, the fly underwent another 3 testing bouts. *Top,* Timelines for individual bouts of training (*left*) and testing (*right*). Both odors were initially attractive and were either apple cider vinegar (ACV) or 1% ethyl acetate; assignments as CS^+ and CS^- were counterbalanced across 12 flies. Red dashed line indicates the end of the training session.

b) Traces showing the mean time-dependent rates of the fly's rotational speed on the trackball, illustrating responses to the CS^+ and CS^- odors for testing bouts pre-training (Pre; top row), at 5 min after conditioning (middle row), and at 1 hr after conditioning (bottom row). Each trace shows the mean response averaged over 12 different flies and the 3 testing bouts within each testing period (see panel **a**).

c) Flies exhibited behavioral conditioning to the CS^+ but not the CS^- odors. Plots show mean ± s.e.m. changes in rotational speed induced by CS^+ and CS^- odors in the pre-training (Pre), 5 min, and 1 hr testing sessions. (*P<0.05; n = 12 female flies; Friedman ANOVA followed by post-hoc Wilcoxon signed-rank tests with Holm-Bonferroni correction). Gray lines denote individual flies.

d) *Bottom,* Timeline for our optical voltage imaging assay of olfactory associative learning and memory in head-fixed awake flies. Each fly first underwent 1 bout of imaging before conditioning (Pre), in which we examined the neuronal spiking responses to the 2 odors to be used during conditioning (CS^+ and CS^-). Next, we subjected each fly to 3 bouts of training, in each of which the fly received a paired presentation of the CS^+ and the unconditioned stimulus (US, a pulse-train of electric shocks), plus an unpaired presentation of the CS^-. At 5 min after the end of the training bouts, each fly underwent a mid-training (Mid) imaging bout to assess the odor-evoked spiking responses. At 5 min after the end of the Mid imaging bout, we subjected each fly to 3 more bouts of training. Then, the fly underwent another 2 imaging bouts at 5 min and 1 hr after the training, respectively. *Top,* Timelines for individual bouts of training (*left*) and imaging (*right*). Both odors were either apple cider vinegar (ACV) or 1% ethyl acetate; assignments as CS^+ and CS^- were counterbalanced across 12 flies. Red dashed line indicates the end of the training session.

e) Example optical voltage traces acquired of MBON-γ1pedc>α/β neuron spiking responses, immediately before, during and after 5-s exposures to either the CS^+ (*orange shading*) or the CS^- (*blue shading*) odors during the pre-training (Pre), mid-training (Mid), 5-min or 1-hr imaging periods (see panel **d**).

f, g) *Left*, Mean ± s.e.m. odor-evoked changes in spike rates of PPL1-DANs (**f**), or MBONs (**g**), induced by the CS^+ and CS^- odors in the pre-training (Pre), mid-training (Mid), 5-min, and 1-hr imaging periods. *Right*, Changes in the CS^+ *vs.* CS^- bias in evoked spiking responses relative to that of the pre-training session (**Methods**). Gray lines denote data from individual flies. (**P*<0.05, ***P*<0.01 and ****P*<0.001; n = 12 flies per neuron-type; Friedman ANOVA followed by post-hoc Wilcoxon signed-rank tests with Holm-Bonferroni correction).

Figure 4

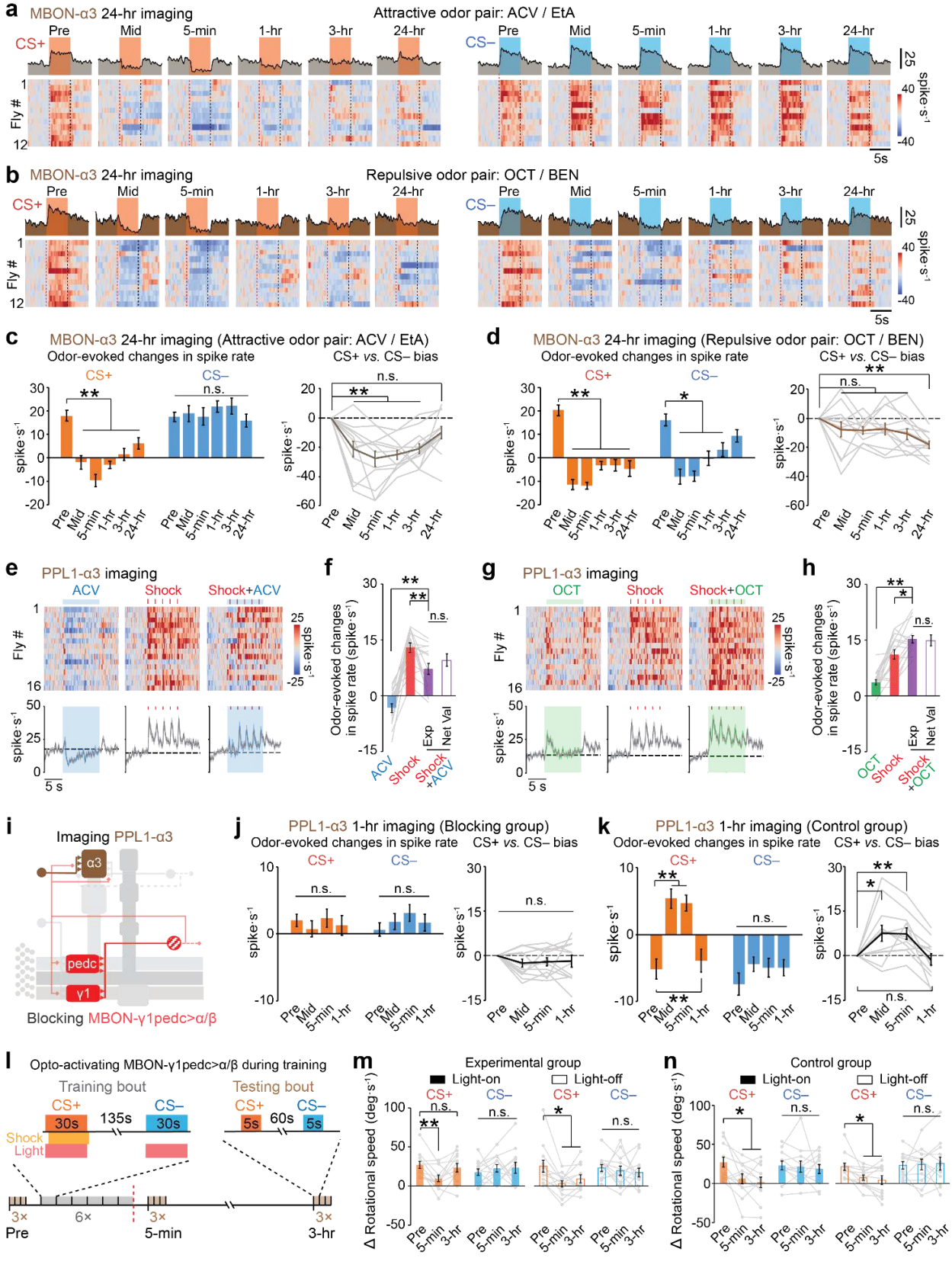
a
MBON-α3 24-hr imaging
Attractive odor pair: ACV / EtA
CS+
CS–
Pre
Mid
5-min
1-hr
3-hr
24-hr
Fly #
spike·s⁻¹
5s
b
MBON-α3 24-hr imaging
Repulsive odor pair: OCT / BEN
c
MBON-α3 24-hr imaging (Attractive odor pair: ACV / EtA)
Odor-evoked changes in spike rate
CS+ vs. CS– bias
d
MBON-α3 24-hr imaging (Repulsive odor pair: OCT / BEN)
e
PPL1-α3 imaging
ACV
Shock
Shock+ACV
f
Odor-evoked changes in spike rate (spike·s⁻¹)
Exp
Net Val
g
PPL1-α3 imaging
OCT
Shock+OCT
h
i
Imaging PPL1-α3
α3
pedc
γ1
Blocking MBON-γ1pedc>α/β
j
PPL1-α3 1-hr imaging (Blocking group)
k
PPL1-α3 1-hr imaging (Control group)
l
Opto-activating MBON-γ1pedc>α/β during training
Training bout
Testing bout
30s
135s
60s
5s
Shock
Light
3×
6×
Pre
5-min
3-hr
m
Experimental group
Light-on
Light-off
Δ Rotational speed (deg·s⁻¹)
n
Control group

Fig. 4 | Both innate and learnt valences influence long-lasting plasticity and behavior.

a, b) Optical voltage imaging reveals plasticity at 24 hr after behavioral conditioning in MBON-α3 neurons trained with a pair of attractive odors, ACV and 1% ethyl acetate (EtA), (**a**), or a pair of repulsive odors, OCT and 0.3% benzaldehyde (BEN), (**b**). We followed the training and imaging protocol of **Fig. 3d,** but with additional imaging sessions at 3 hr and 24 hr post-training. *Top*, Traces show the time-dependent mean spiking rates of MBON-α3, immediately before, during and after 5-s exposures to either the CS^+ (*orange*) or the CS^- (*blue*) odors during the pre-training (Pre), mid-training (Mid), 5-min, 1-hr, 3-hr, and 24-hr imaging sessions. *Bottom*, Odor-evoked changes in spike rates of MBON-α3 neurons, relative to baseline spiking rates, in 12 individual flies. Each row shows a single trial of data from each fly.

c, d) *Left*, Mean ± s.e.m. odor-evoked changes in spike rates (relative to spike rates in the 5 s before odor presentation) of MBON-α3 neurons trained with attractive odors (ACV and EtA), (**c**), or repulsive odors (OCT and BEN), (**d**), induced by the CS^+ and CS^- odors in the pre-training (Pre), mid-training (Mid), 5-min, 1-hr, 3-hr, and 24-hr imaging sessions. *Right*, Changes in the CS^+ *vs.* CS^- bias in evoked spiking responses relative to that of the pre-training session (**Methods**). Gray lines denote data from individual flies. (**P*<0.05 and ***P*<0.01; n = 12 flies per neuron-type; Friedman ANOVA followed by post-hoc Wilcoxon signed-rank tests with Holm-Bonferroni correction).

e) Attractive odor attenuates punishment-induced spiking response in PPL1-α3. *Top*, Changes in spike rates in the PPL1-α3 neuron relative to baseline spiking rates, immediately before, during and after exposures to either 10-s-exposures to apple cider vinegar (ACV; blue shading; *left*), 5 electric-shock pulses (each 0.2 s in duration with 1.8 s interval between pulses; red tick marks; *middle*), or the paired presentation of ACV and shocks (*right*) to n = 16 flies (1 trial per fly for

each of the 3 stimulation conditions). *Bottom*, Traces showing the time-dependent mean spiking rates, averaged over all 16 trials for each stimulus. Dashed lines mark the mean baseline spiking rates, averaged over the first 5 s of recording. Gray shading on the time traces: s.e.m.

f) Mean ± s.e.m. odor-evoked changes in the spike rates of the PPL1-α3 neuron, relative to baseline levels, as measured during 10-s exposures to either ACV (*blue bar*), 5 electric shocks (*red bar*), or the paired presentation of ACV and shocks (*purple solid bar*). (**P<0.01; n = 16 flies; Friedman ANOVA followed by post-hoc Wilcoxon signed-rank tests with Holm-Bonferroni correction). The changes in spiking in response to the paired presentation of ACV and shocks were indistinguishable from the sum of the changes induced by the two stimulus-types, when each was presented independently (*purple hollow bar*; n = 16 flies; Wilcoxon rank sum test). Gray lines denote data from individual flies.

g) Repulsive odor enhances punishment-induced spiking responses in PPL1-α3. *Top*, Changes in spike rates, immediately before, during and after 10-s-exposures to either 1% 3-octanol (OCT; *green shading*), 5 pulses of 200-ms-electric-shock (*red lines*), or the joint presentation of OCT and shock (n =16 flies, 1 trial per fly for each of the 3 stimulation conditions). *Bottom*, Traces showing the time-dependent mean spiking rates, averaged over all 16 trials for each stimulus. Dashed lines: mean baseline spiking rates, averaged over the first 5 s of recording. Gray shading on the time traces: s.e.m.

h) Mean ± s.e.m. odor-evoked changes in the spike rates of PPL1-α3 relative to baseline levels, measured during 10-s exposures to either OCT (*green bar*), electric shocks (*red bar*), or joint presentation of OCT and shocks (*purple solid bar*). (*P<0.05 and **P<0.01; n = 16 flies; Friedman ANOVA followed by post-hoc Wilcoxon signed-rank tests with Holm-Bonferroni correction). The spiking responses to the joint presentation of OCT and shocks were

indistinguishable from the sum of the changes induced by the two stimulus-types, when each was presented independently (*purple hollow bar*) (n = 16 flies; Wilcoxon ranked sum test). Gray lines denote data from individual flies.

i) A connectivity diagram showing the feedback connections from the MBON-γ1pedc>α/β neuron to the PPL1-α3 neuron. To assess the influence of MBON-γ1pedc>α/β feedback on PPL1-α3, we blocked the synaptic transmission of MBON-γ1pedc>α/β neuron by expressing the tetanus toxin light chain and then performing voltage imaging on PPL-α3 using the pAce voltage-indicator ((*TH-LexA/13×LexAop-pAce;MB085C/UAS-TnT*).

j, k) *Left*, Mean ± s.e.m. odor-evoked changes in PPL1-α3 spike rates in the blocking (*TH-LexA/13×LexAop-pAce;MB085C/UAS-TnT*), (**j**), or control (*TH-LexA/13×LexAop-pAce*) groups, (**k**), induced by the CS^+ and CS^- odors in the pre-training (Pre), mid-training (Mid), 5-min, and 1-hr imaging sessions. *Right*, Changes in the CS^+ *vs.* CS^- bias in evoked spiking responses relative to that of the pre-training session (**Methods**). Gray lines denote data from individual flies. (**P*<0.05 and ***P*<0.01; n = 12 flies per neuron-type; Friedman ANOVA followed by post-hoc Wilcoxon signed-rank tests with Holm-Bonferroni correction).

l) *Bottom,* Timeline for 3-hr behavioral assay of memory with optogenetic activation, for 4 distinct groups of head-fixed awake flies on a trackball. An experimental group of flies (*MB085C/UAS-CsChrimson-tdT*) expressed the CsChrimson opsin in MBON-γ1pedc>α/β. Control flies (*MB085C/+*) lacked the opsin. Each of these two genotypes was subdivided into groups that either did (Light-on) or did not (Light-off) receive optogenetic illumination (red shading) during the same period as odor presentation. Each fly first underwent 3 bouts of odor-testing before conditioning (Pre), in which we examined the animal's initial behavioral responses to the 2 odors to be used during conditioning (CS^+ and CS^-). Next, we subjected each

fly to 6 bouts of training, in each of which the fly received a paired presentation of the CS^+ and the unconditioned stimulus (US, a pulse-train of electric shocks), as well as an unpaired presentation of the CS^-. Flies of either genotype in a 'Light-On' group also received 30 pulses of 0.5-s red-light (625 nm, 0.5Hz) during CS^+ and CS^- presentations. At 5 min after the end of the last training bout, each fly underwent 3 bouts of testing to assess its odor-evoked behavioral responses post-conditioning. At 3 hr after the end of training, each fly underwent another 3 bouts of memory testing. *Top,* Timelines for individual bouts of training (*left*) and testing (*right*). Both odors were initially attractive and were either ACV or EtA; assignments as CS^+ and CS^- were counterbalanced across 12 flies. Experimental results are shown in **m, n**. Red dashed line indicates the end of the training session.

m, n) At 3-hr-post-conditioning, flies in the Light-on experimental group (*MB085C/UAS-CsChrimson-tdT*) had impaired 3-hr memory performance as compared to flies with the same genotype in the Light-off group, (**m**). Flies in the control group (*MB085C/+*) had normal memory performance at 3 hr after conditioning, regardless of whether they received optogenetic illumination, (**n**). Plots show mean ± s.e.m. changes in rotational speed induced by CS^+ and CS^- odors in the pre-training (Pre), 5 min, and 1 hr testing sessions. (**P*<0.05; n = 12 flies per neuron-type; Friedman ANOVA followed by post-hoc Wilcoxon signed-rank tests with Holm-Bonferroni correction). Gray lines indicate individual flies. Solid and open bars denote data from the Light-on and Light-off groups, respectively.

Figure 5

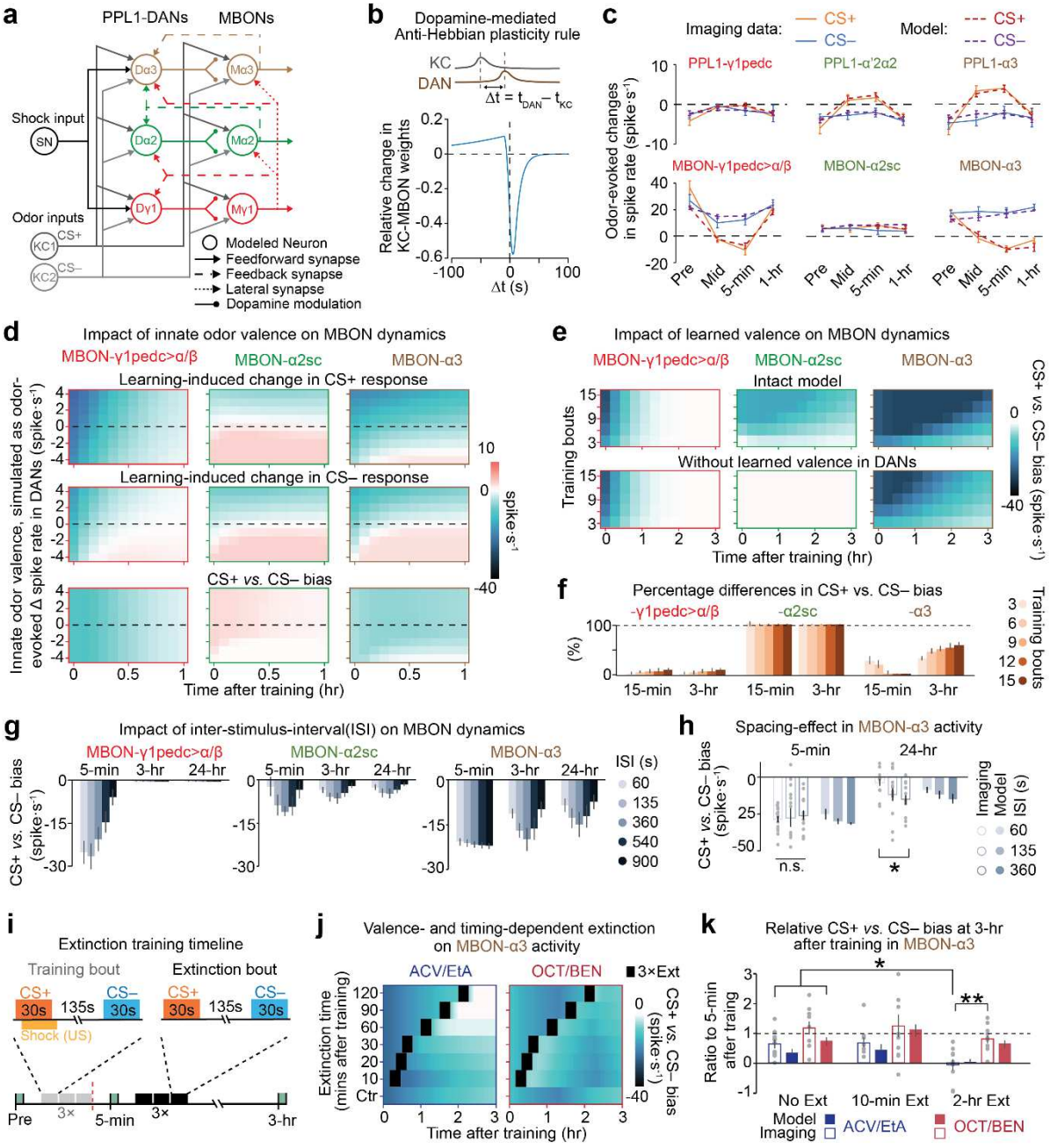
a
PPL1-DANs
MBONs
Shock input
SN
Odor inputs
CS+
CS–
Modeled Neuron
Feedforward synapse
Feedback synapse
Lateral synapse
Dopamine modulation
b
Dopamine-mediated Anti-Hebbian plasticity rule
KC
DAN
Relative change in KC-MBON weights
Δt (s)
c
Imaging data:
Model:
CS+
CS–
PPL1-γ1pedc
PPL1-α'2α2
PPL1-α3
MBON-γ1pedc>α/β
MBON-α2sc
MBON-α3
Odor-evoked changes in spike rate (spike·s⁻¹)
Pre
Mid
5-min
1-hr
d
Impact of innate odor valence on MBON dynamics
Learning-induced change in CS+ response
Learning-induced change in CS– response
CS+ vs. CS– bias
Innate odor valence, simulated as odor-evoked Δ spike rate in DANs (spike·s⁻¹)
Time after training (hr)
spike·s⁻¹
e
Impact of learned valence on MBON dynamics
Intact model
Without learned valence in DANs
Training bouts
Time after training (hr)
CS+ vs. CS– bias (spike·s⁻¹)
f
Percentage differences in CS+ vs. CS– bias
-γ1pedc>α/β
-α2sc
-α3
(%)
15-min
3-hr
Training bouts
g
Impact of inter-stimulus-interval(ISI) on MBON dynamics
5-min
3-hr
24-hr
CS+ vs. CS– bias (spike·s⁻¹)
ISI (s)
h
Spacing-effect in MBON-α3 activity
n.s.
*
Imaging
Model
ISI (s)
i
Extinction training timeline
Training bout
Extinction bout
CS+
CS–
30s
135s
Shock (US)
Pre
3×
5-min
3-hr
j
Valence- and timing-dependent extinction on MBON-α3 activity
ACV/EtA
OCT/BEN
3×Ext
Extinction time (mins after training)
Ctr
Time after training (hr)
CS+ vs. CS– bias (spike·s⁻¹)
k
Relative CS+ vs. CS– bias at 3-hr after training in MBON-α3
Ratio to 5-min after traing
**
No Ext
10-min Ext
2-hr Ext
Model
Imaging
ACV/EtA
OCT/BEN

Fig. 5 | A computational model of the mushroom body constrained by the fly connectome and optical voltage recordings captures the interactions between learning units and yields testable predictions about memory storage and extinction.

a) Diagram showing the connectivity of the 3 interconnected learning modules (γ1, α2 and α3) in our computational model, which is constrained by both the voltage imaging data of this paper and the fly connectome[30]. Each of the 3 modules is shown in a distinct color. There are 9 different types of neurons (open circles) in the model. Solid lines with arrowheads denote feedforward synaptic connections; dashed lines with arrowheads indicate feedback synaptic connections; dotted lines with arrowheads indicate feedback synaptic connections; solid lines with circular heads indicate sites of presynaptic dopaminergic modulation. Kenyon cells (KC1 and KC2) receive olfactory CS^+ and CS^- signals and transmit them to the downstream DANs and MBONs via KC→DAN and KC→MBON connections, respectively. DANs integrate shock input from a shock-sensing neuron (SN), olfactory information conveyed via the KC→DAN connections, and feedback signals from the MBONs via the MBON→DAN connections. Concurrent activation of a KC and its postsynaptic DAN modifies the synaptic weight of the KC→MBON connection according to an anti-Hebbian learning rule (see panel **b** and **Methods**). **Supplementary Table 1** in the **Supplementary Appendix** lists all 25 parameters in the model and the parameter values that led to an optimal fit to the experimental voltage-imaging data taken across multiple time points in the learning process. Specifically, we found the optimal parameter values by fitting the spiking rates in the model to the 64 measurements of mean ± s.e.m spike rates and odor-evoked changes in spiking for the 3 PPL1-DANs and 3 MBONs during pre-training (Pre), mid-training (Mid), 5-min, and 1-hr imaging periods (40 data points from **Fig. 3g,h**) and the 24-hr recordings in MBON-α3 (24 data points from **Fig. 4c,d**). SN: Shock-sensing neuron; KC: Kenyon cell; Dγ1: PPL1-γ1pedc; Dα2: PPL1-α'2α2; Dα3: PPL1-α3;

Mγ1: MBON-γ1pedc>α/β; Mα2: MBON-α2sc; Mα3: MBON-α3.

b) A graph showing the timing dependence of the dopamine-mediated, anti-Hebb rule governing plasticity of the KC→MBON connections in the computational model. Δt denotes the time difference between DAN and KC activation. When a DAN activates before its presynaptic KC, this increases the strength of the downstream KC→MBON synaptic connection. In contrast, when a KC activates before its presynaptic DAN, this decreases the strength of the KC→MBON connection.

c) After finding the optimal parameter values for the computational model, we examined how well the model's predictions matched the data used to train it. We compared the mean ± s.e.m. odor-evoked changes in spiking for the 6 DAN and MBON neuron-types, as found empirically from voltage-imaging data (*solid lines*), to the model predictions (*dashed lines*) for time points before, mid-way through, and at 5 min and 1 hr after associative conditioning. For both the empirical and computational studies, we followed the full protocol for associative conditioning shown in **Fig. 3d**. For the empirical studies, we used two odorants of approximately equal innate valences, ACV and EtA, for the CS^+ and CS^- (with CS^+ and CS^- assignments counterbalanced across 12 flies as in **Fig. 3f,g**). Black horizontal dashed lines mark zero change in spiking upon odor presentation. For the modeling studies, we used CS^+ and CS^- odors of equal valences, matched in value to the average innate valence of ACV and EtA, as determined using odor-evoked changes in DAN spiking prior to conditioning. As the plots show, the model well captures the patterns of odor-evoked spiking at all phases of associative conditioning.

d) We used the optimized computational model to examine how the innate valences of 9 different hypothetical odors influence the learning-induced changes in odor-evoked spiking for the 3 different MBONs in the model. Within each of the individual plots shown, each row presents

data for a single hypothetical odor. The innate valence of each odor is specified by the change in DAN spiking that it evokes (*y*-axis values), relative to baseline spiking levels and prior to any associative conditioning. Using the model, we simulated a single training bout of associative conditioning, according to the protocol of **Fig. 3d**, using each of the 9 odors as either the CS^+ (top 3 plots) or the CS^- (middle 3 plots); these 6 plots show, as a function of time after the training bout, the resulting changes in the odor-evoked rates of MBON spiking. The bottom 3 plots show how the biases between CS^+-evoked and CS^--evoked MBON spiking change as a function of time after the training bout. After a single training bout, all 3 MBONs exhibit plasticity in their responses to both the CS^+ and CS^-. The MBON-γ1pedc>α/β exhibits short-lived depression, MBON-α2sc undergoes longer-lived plasticity that can be either a potentiation or a depression depending on the odor's innate valence, and MBON-α3 exhibits the longest-lasting plasticity, which also can be bi-directional. **Extended Data Fig. 9** has additional results.

e) To explore how neural feedback from MBON-γ1pedc>α/β to the DANs influences the associative conditioning process, we used the optimized model to simulate the biases between CS^+-evoked and CS^--evoked MBON spiking after different numbers of training bouts (*y*-axis values) occurring in immediate succession, with the feedback pathway shown in panel **a** either active (top row of plots) or inactivated (bottom row of plots). These computational studies used hypothetical odors with no innate valence for either the CS^+ or CS^-. The 6 plots show, as a function of time after the last training bout, the resulting biases between CS^+-evoked and CS^--evoked MBON spiking, for simulations with (top row) or without (bottom row) feedback signals from MBON-γ1pedc>α/β. The removal of feedback has little net effect on the plasticity of MBON-γ1pedc>α/β (left column), obliterates the plasticity of MBON-α2sc (middle column),

and decreases the longevity of plasticity in MBON-α3 (right column).

f) To evaluate the functional importance of feedback signals from MBON-γ1pedc>α/β, we used the optimized model to compare the levels of plasticity that arise in each MBON in the presence or absence of the feedback. The differences between these values provide assessments of the feedback's impact. The plot shows the percentage differences in the mean CS^+ *vs.* CS^- spiking bias with *vs.* without MBON-γ1pedc>α/β feedback, for 3–15 training bouts, and at 15-min and 3-hr after the last training bout (n = 10,000 simulations; error bars span the 16%–84% C.I. percentiles).

g) We used the computational model to evaluate how the inter-stimulus-interval (ISI) between CS^+ and CS^- presentations within a training bout influences MBON plasticity at different time points after training. The plots show the mean CS^+ *vs.* CS^- spiking bias in each of the 3 MBONs in the model, at 5 min, 3 hr or 24 hr after 10 bouts of training using different ISI values (n = 10,000 simulations per ISI value; error bars span the 16%–84% C.I. percentiles). These computational studies used hypothetical odors with no innate valence for either the CS^+ or CS^-.

h) To test the model's predictions for the training protocols used in our experiments, we examined how the inter-stimulus-interval (ISI) between CS^+ and CS^- presentations affected MBON plasticity at different time points after 6 training bouts (the protocol of **Fig. 3d**) in both the simulations and the real data. The plot shows model predictions (solid bars; mean values) and measured values (open bars; mean ± s.e.m.) for the CS^+ *vs.* CS^- spiking bias in MBON-α3 at 5 min and 24 hr after the 6th training bout, using an ISI of 60 s, 135 s or 360 s. Gray dots: data from individual flies. Real data: $*P<0.05$; n = 14 flies; Kruskal-Wallis ANOVA followed by post-hoc Mann-Whitney U-tests with Holm-Bonferroni correction. Modeling data: n = 10,000 simulations per ISI value; error bars span the 16%–84% C.I. percentiles.

i) *Bottom,* Timeline for extinction training in both our optical voltage imaging experiments and computational simulations. Each fly first underwent 1 bout of imaging before conditioning (Pre), in which we examined the neuronal spiking responses to the 2 odors to be used during conditioning (CS^+ and CS^-). Next, we subjected each fly to 3 bouts of training, in each of which the fly received a paired presentation of the CS^+ and the unconditioned stimulus (US, a pulse-train of electric shocks), and an unpaired presentation of the CS^-. At 5 min after the end of the training bouts, each fly underwent another imaging bout (5-min) to assess the odor-evoked spiking responses. At different time points after the end of the training bout, we subjected each fly to 3 bouts of extinction, in each of which the fly received CS^+ and CS^- presentation but no shock presentation. Then, the fly underwent another imaging bout at 3 hr after the training. *Top,* Timelines for individual bouts of training (*left*) and extinction (*right*). Red dashed line indicates the end of the training session.

j) To examine the effects of extinction training, we used the optimized model to simulate the effects of extinction training (3 bouts of CS^+ and CS^- presentation but no shock presentation) occurring at different times after the last conditioning bout. The plots show model predictions for the CS^+ *vs.* CS^- spiking bias in MBON-α3 across a 3-hr duration following 3 bouts of classical conditioning; the different rows of each plot show the results for extinction sessions (marked with black squares) occurring at distinct times after the last training bout; the bottom row marks the result has no extinction. The simulations used pairs of odors that both had attractive innate valences (left plot; valences matched to those of apple cider vinegar, ACV, and 1% ethyl acetate, EtA) or both had aversive innate valences (right plot; valences matched to those of 1% 3-octanol, OCT, and 0.3% benzaldehyde, BEN). For the innately attractive odors, extinction training has the greatest effect when it occurs at substantial intervals after the end of conditioning. For the

innately aversive odors, the effect of extinction training is less dependent on its time of occurrence.

k) To test the predictions of panel **j**, we compared the simulated (solid bars; mean values) and experimentally measured (open bars; mean ± s.e.m.) values of the CS^+ *vs.* CS^- spiking bias in MBON-α3 at 3 hr after training, with either no extinction training, or with extinction training (3 bouts) at either 10 min or 2 hr after the end of classical conditioning (3 training bouts). The graph shows these values of the bias, normalized by the bias value at 5 min after classical conditioning. Training and extinction used either innately attractive odors (ACV and EtA; blue data) or repulsive odors (OCT and BEN; red data). Gray dots: data from individual flies. Real data: $*P<0.05$, $**P<0.01$; n = 10 flies; Kruskal-Wallis ANOVA followed by post-hoc Mann-Whitney U-tests with Holm-Bonferroni correction. Modeling data: n = 10,000 simulations per ISI value; error bars span the 16%–84% C.I. percentiles.

Extended Data Fig. 1

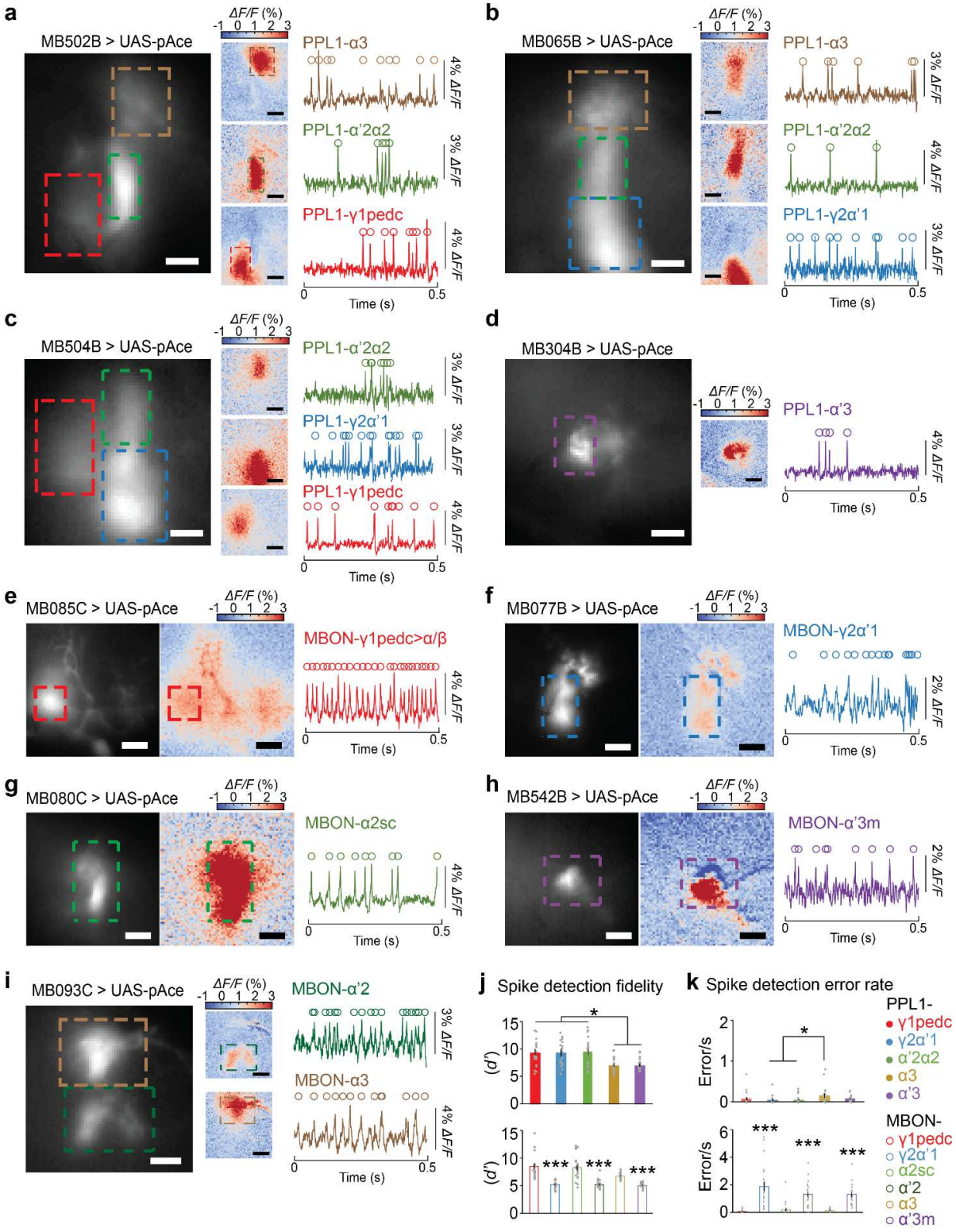

Extended Data Fig. 1 | Voltage imaging of neural spiking activity using split-GAL4 lines to label PPL1-DANs and their downstream MBONs.

a–h) Example data from voltage imaging experiments of 5 different types of PPL1-DANs and 6 different types of MBONs. *Left panels,* Mean fluorescence images (averaged over 15 s of voltage movies), showing the patterns of pAce expression in 9 different split-GAL4 lines. Dashed boxes demarcate regions-of-interest (ROIs) from which we aggregated fluorescence signals to determine fluorescence traces of transmembrane voltage activity in individual neurons. *Middle panels,* Spatial maps of the mean fluorescence responses ($\Delta F/F$) of individual neuron-types at the peaks of their action potentials, averaged over all spikes detected (open circles) within the selected 15-s-intervals. Dashed boxes enclose the same regions as in the left panels. *Right panels,* Traces of each neuron's relative fluorescence changes ($\Delta F/F$) during the same 15-s-intervals used to create the spatial maps. All scale bars are 10 μm.

j,k) Mean ± s.e.m. values of the spike detection fidelity (d'), **j**, and spike detection error rate, **k**, for PPL1-DANs (*top graphs*) and MBONs (*bottom graphs*). For each neuron-type, we collected data from 20 different flies; gray dots are data points from individual flies. All 4 graphs exhibited significant differences across neuron-types (n = 20 flies per neuron-type; Kruskal-Wallis ANOVA). Horizontal lines and asterisks mark pairwise comparisons that yielded significant differences in post-hoc Mann-Whitney U-tests performed with a Holm-Bonferroni correction for multiple comparisons (*P<0.05, **P<0.01, and ***P<0.001).

Extended Data Fig. 2

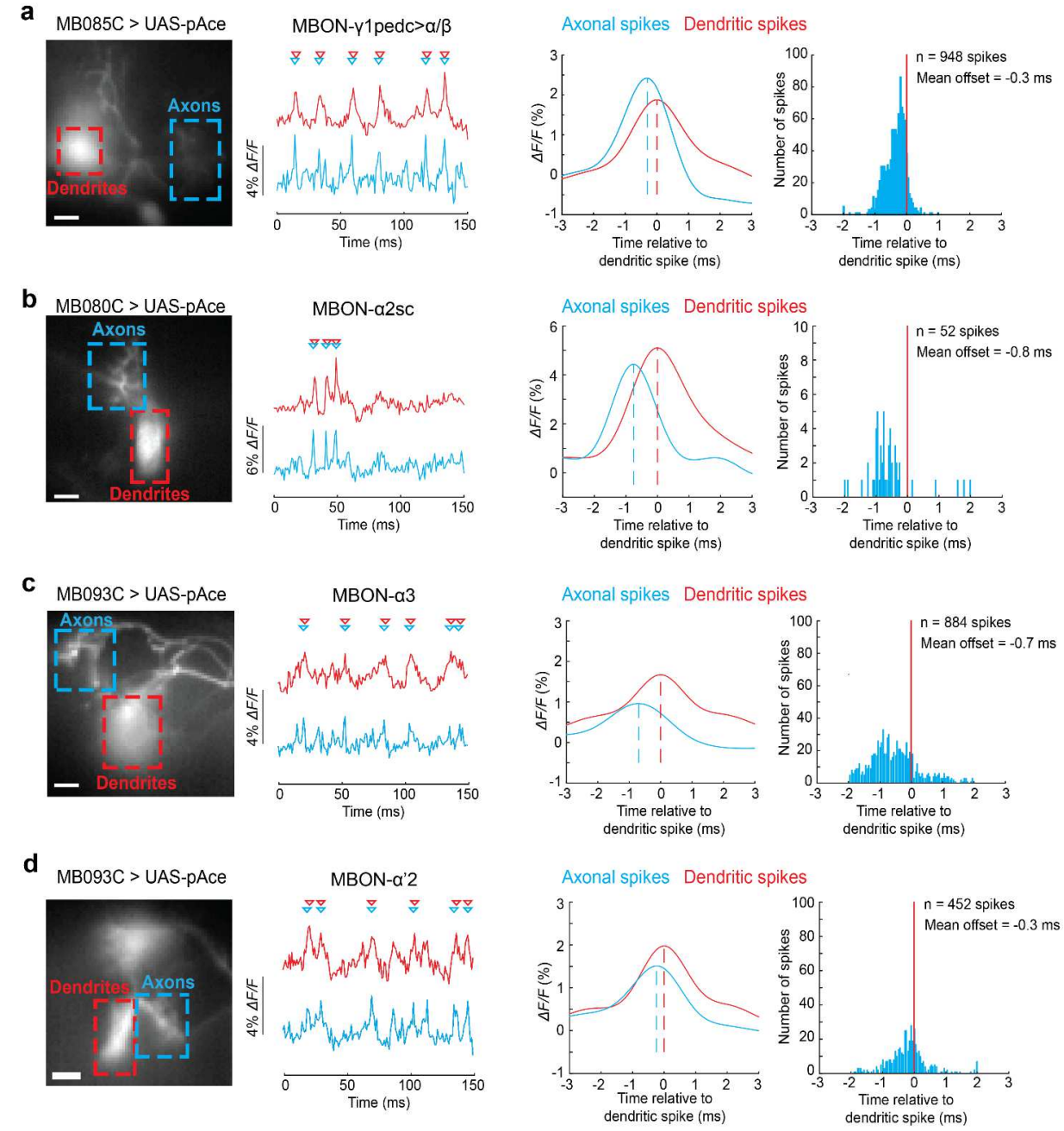

Extended Data Fig. 2 | Axonally initiated spikes in MBONs backpropagate into the dendritic arbors.

a–d) Example data from 4 different types of MBONs showing the backpropagation of spikes into the dendritic tree. *Left panels,* Mean fluorescence images (each an average over a 15-s-interval of a voltage movie), showing the spatial pattern of pAce expression within an individual MBON-type. Dashed boxes demarcate regions-of-interest (ROIs) that enclose either axons (*blue*) or dendrites (*red*) of the selected cell. Scale bars are 10 μm. *Left middle panels,* Fluorescence traces of transmembrane voltage activity from each cell's axonal ROI (blue traces) and dendritic ROI (red traces). Triangles mark the peak of detected action potentials. *Right middle panels,* Mean waveforms of the axonal (blue traces) and dendritic spikes (red traces), computed by spline interpolation of the fluorescence traces determined from the 1-kHz-voltage imaging data. Vertical dashed lines mark the peaks of these spike waveforms and reveal the temporal offsets between axonal and dendritic spikes. *Right panels,* Histograms of the temporal offsets between axonal and dendritic spikes, assessed relative to the time of the dendritic spike.

Extended Data Fig. 3

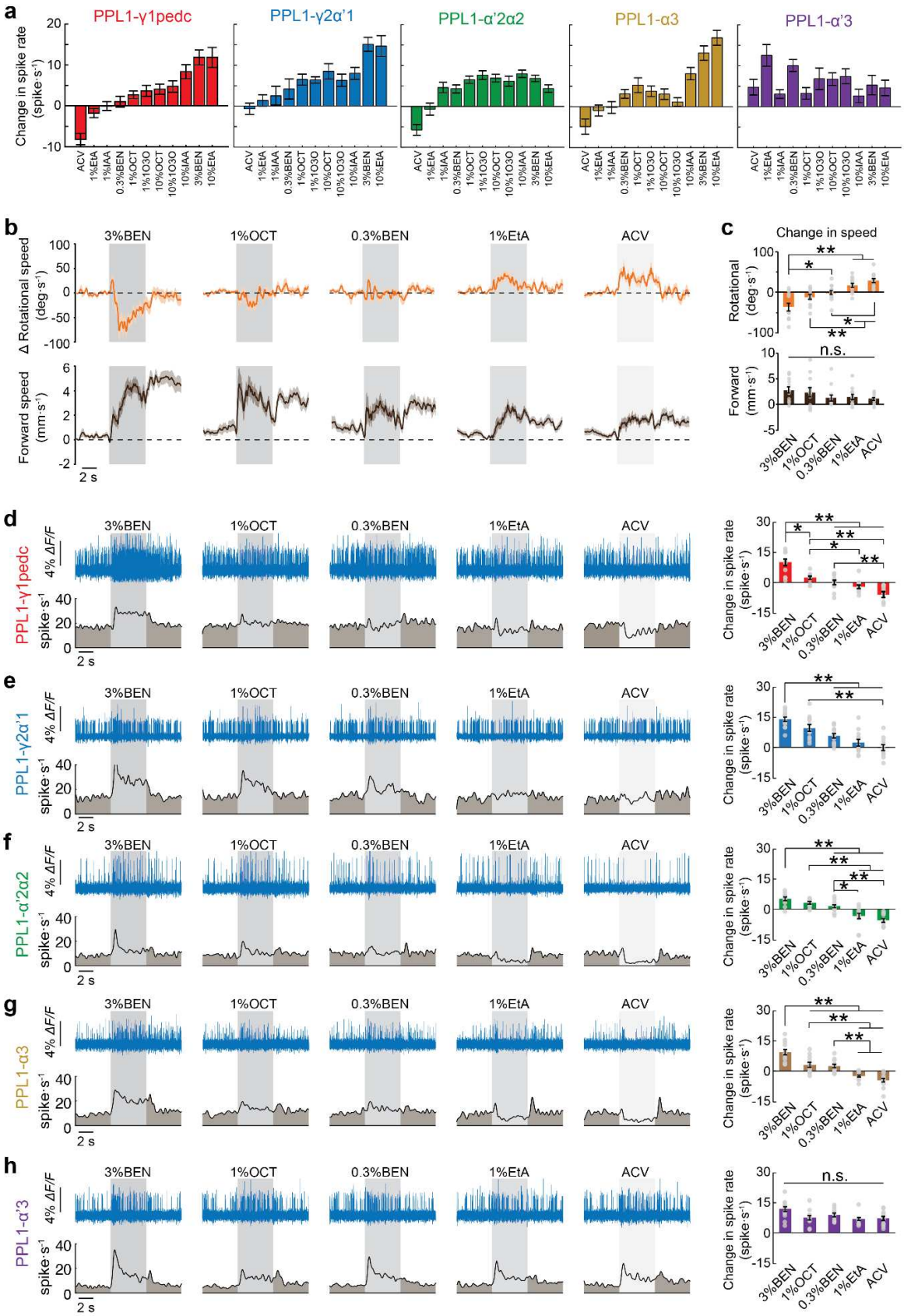

Extended Data Fig. 3 | PPL1-DANs bidirectionally encode innate odor valences.

a) Mean ± s.e.m. changes in spike rates measured during odor exposure (5 s duration), relative to baseline spiking rates, in PPL1-γ1pedc, -γ2α'1, -α'2α2, -α3 and -α'3 neurons (n = 4–6 flies per odor, 2 trials per fly). Odorants: Apple cider vinegar (ACV), 0.3% or 3% benzaldehyde in mineral oil (0.3% or 3% BEN), 1% or 10% 3-octanol in mineral oil (1% or 10% OCT), 1% or 10% ethyl acetate in mineral oil (1% or 10% EtA), 1% or 10% 1-octen-3-ol in mineral oil (1% or 10% 1O3O). The different PPL1-DANs exhibit different degrees of sensitivity to odor valence.

b) Mean time-dependent changes in the rotational (*upper panels*) and forward walking speeds (*lower panels*) of wild-type flies (w^{1118}) in response to 5 different odors (3% BEN, 1% OCT, 0.3% BEN, 1% EtA, and ACV), each presented for a duration of 5 s. Gray shading marks the duration of odor delivery. Shading on the time traces: s.e.m. over 36 total trials in 12 flies.

c) Mean ± s.e.m. changes in the rotational (*upper panel*) and forward walking speeds (*lower panel*) of wild-type flies (w^{1118}) in response to the 5 odors used in **b**, averaged over the 5 s of odor presentation and 36 trials per odor (n = 12 flies, 3 trials per fly). Individual points denote data from individual flies. (*P<0.05 and *P<0.01; n = 12 flies per neuron type; Friedman ANOVA followed by post-hoc Wilcoxon signed-rank tests with Holm-Bonferroni correction)

d–h) *Upper left panels,* Example optical voltage traces showing PPL1-DAN responses to the presentation of the same 5 odors as in **b**. Gray shading covers the duration of odor delivery. *Lower left panels,* Mean time-dependent spike rates in response to each odor, averaged over 12 flies for each neuron-type, 1 trial per odor. *Right panels,* Mean ± s.e.m. odor-evoked changes in spiking rates relative to baseline levels in the different PPL1-types, averaged over 12 flies per neuron-type, 1 trial per odor, and the 5 s of odor presentation. All PPL1-types except for PPL1-α'3 exhibited significantly different responses to the different odors (Friedman ANOVA).

Horizontal lines and asterisks mark pairwise comparisons that were significantly different in post-hoc tests (Wilcoxon signed rank tests with Holm-Bonferroni correction for multiple comparisons; *P<0.05 and *P<0.01).

Extended Data Fig. 4

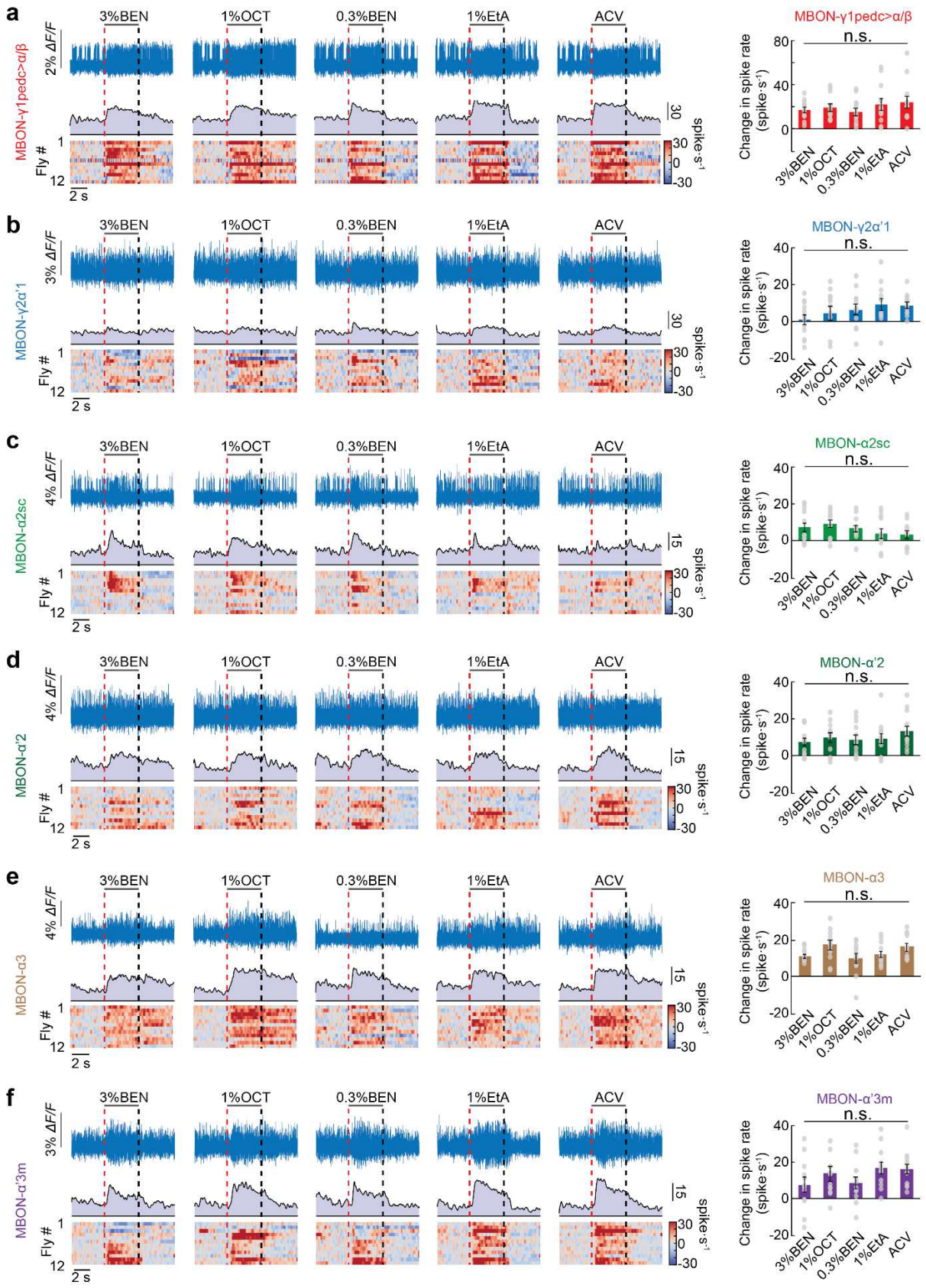

Extended Data Fig. 4 | The odor-evoked responses of MBONs do not vary much across odors with different innate valences.

a–f) *Left panels,* Example fluorescence voltage traces (*top rows*), time-dependent mean spiking rates (*middle rows*), and odor-evoked changes in 12 individual flies' spike rates relative to baseline rates (*bottom rows*), for 6 different MBON-types during 5-s-presentations of 5 different odors. Red vertical dashed lines mark the onsets of odor presentation, and black vertical dashed lines mark the offsets. The mean spike rates shown in each graph of the middle rows are averages over the same 12 flies, for which data is shown individually in the corresponding graph of the bottom row. *Right panels,* Bar graphs showing the mean ± s.e.m. changes in spike rates measured during 5-s-odor presentations, determined relative to baseline spiking rates. None of the bar graphs exhibited significant differences in the MBON responses to different odorants (Friedman ANOVA; $P > 0.05$).

Extended Data Fig. 5

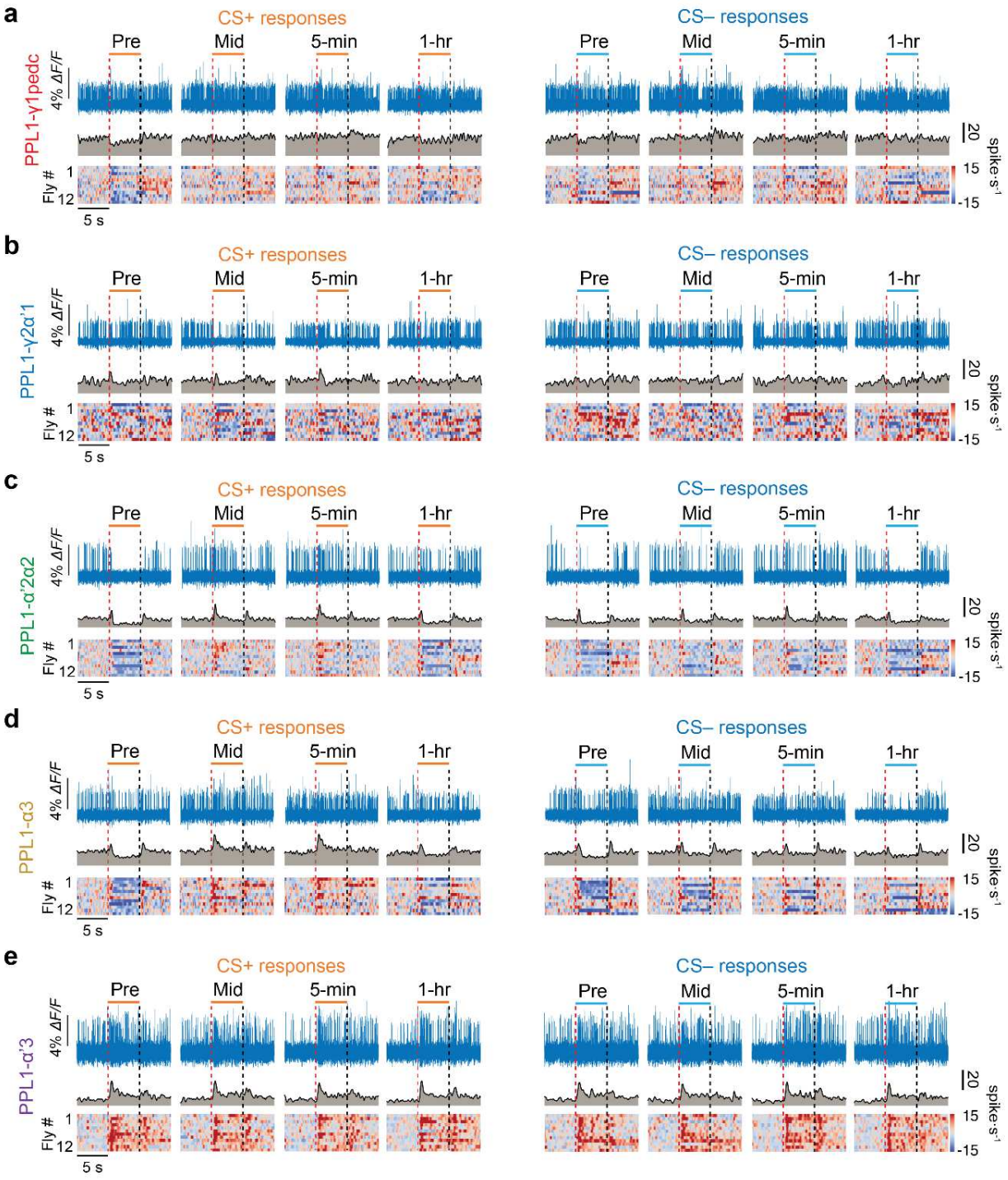

Extended Data Fig. 5 | Olfactory conditioning with an attractive odor pair increases CS^+-evoked responses in PPL1-α'2α2 and PPL1-α3 but not PPL1-γ1pedc, PPL1-γ2α'1 and PPL1-α'3.

a–e) Example fluorescence voltage traces (*top rows*), time-dependent mean spiking rates (*middle rows*), and odor-evoked changes in spike rates relative to baseline rates in 12 individual flies (*bottom rows*) for PPL1-γ1pedc (**a**), PPL1-γ2α'1 (**b**), PPL1-α'2α2 (**c**), PPL1-α3 (**d**), and PPL1-α'3 (**e**) neurons in response to CS^+ and CS^- odors in the pre-training (Pre), mid-training (Mid), 5-min post-training, and 1-hr post-training periods (as defined in **Fig. 3d**). Red vertical dashed lines mark the onsets of odor presentation, and black vertical dashed lines mark the offsets. The mean spike rates shown in each graph of the middle rows are averages over the same 12 flies, for which data is shown individually in the corresponding graph of the bottom row. For each conditioning experiment, we used apple cider vinegar (ACV) and 1% ethyl acetate and assigned them as CS^+ and CS^- in a counterbalanced manner across 12 flies.

Extended Data Fig. 6

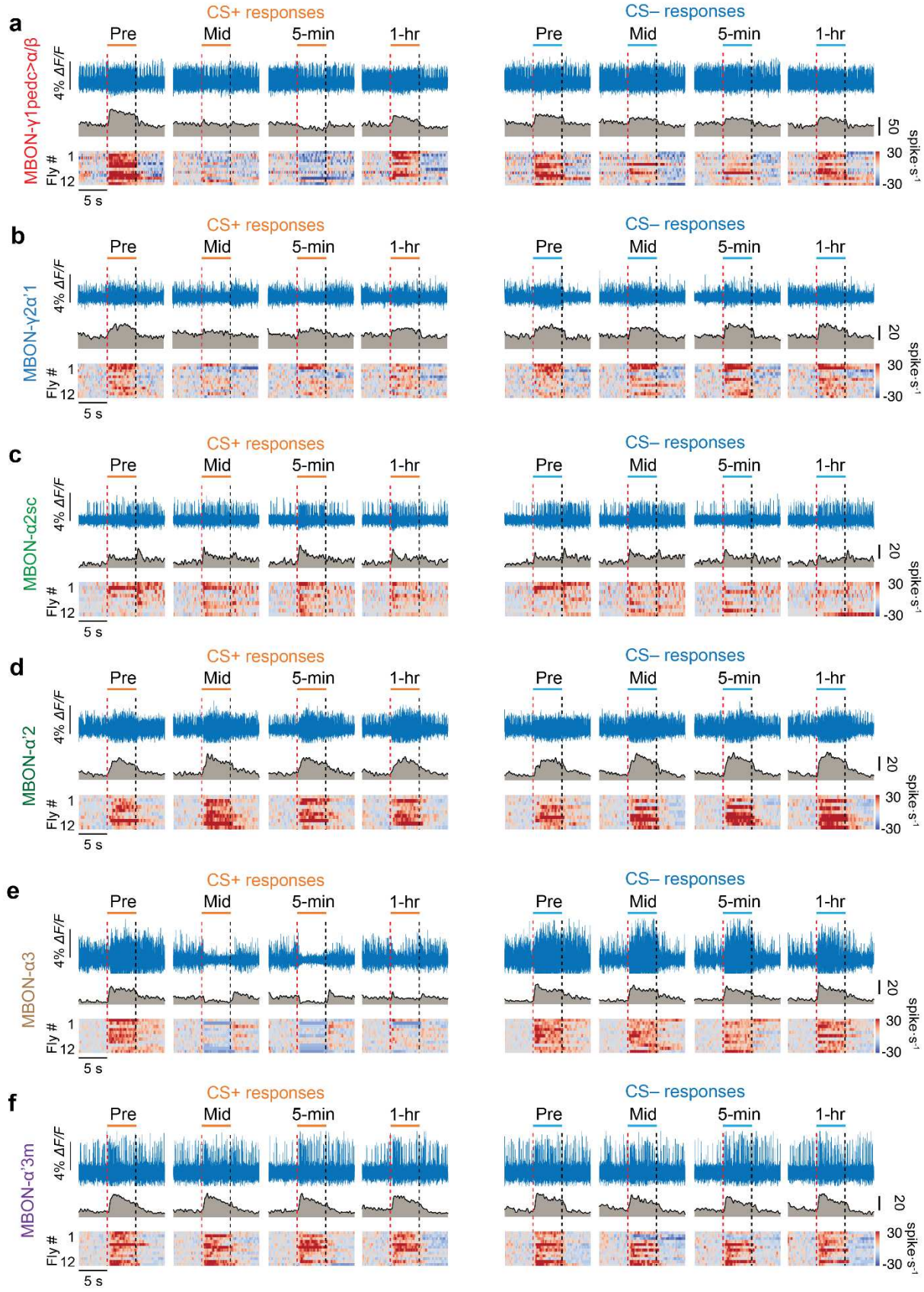

Extended Data Fig. 6 | Olfactory conditioning with an attractive odor pair increases CS^+ responses in MBON-γ1pedc>α/β, MBON-γ2α'1 and MBON-α3.

a–e) Example fluorescence voltage traces (*top rows*), time-dependent mean spiking rates (*middle rows*), and odor-evoked changes in spike rates relative to baseline rates in 12 individual flies (*bottom rows*) for MBON-γ1pedc>α/β (**a**), MBON-γ2α'1 (**b**), MBON-α2sc (**c**), MBON-α'2 (**d**), MBON-α3 (**e**) and MBON-α'3m (**f**) in response to CS^+ and CS^- odors in the pre-training (Pre), mid-training (Mid), 5-min post-training, and 1-hr post-training periods (as defined in **Fig. 3d**). Red vertical dashed lines mark the onsets of odor presentation, and black vertical dashed lines mark the offsets. The mean spike rates shown in each graph of the middle rows are averages over the same 12 flies, for which data is shown individually in the corresponding graph of the bottom row. For each conditioning experiment, we used apple cider vinegar (ACV) and 1% ethyl acetate and assigned them as CS^+ and CS^- in a counterbalanced manner across 12 flies.

Extended Data Fig. 7

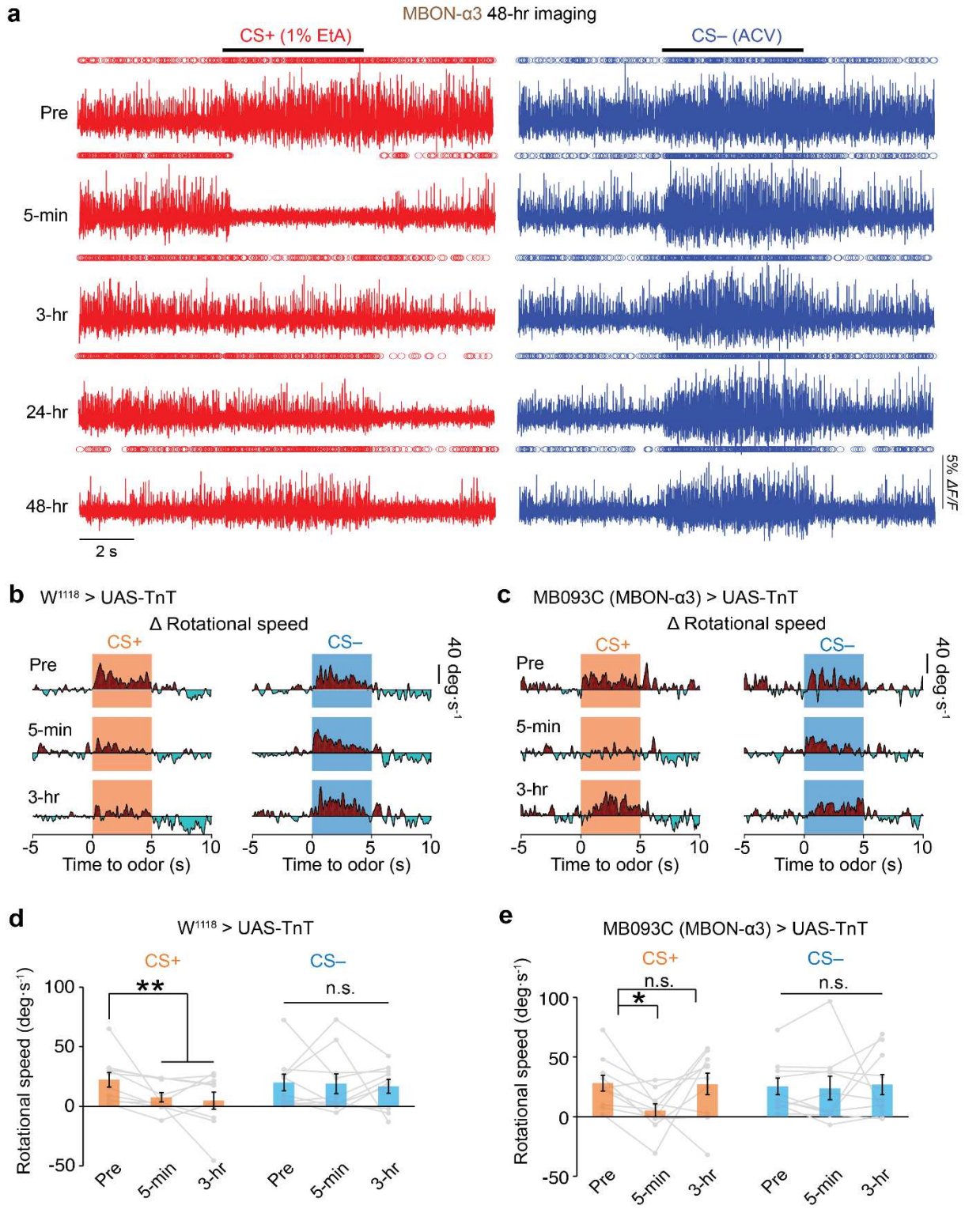

Extended Data Fig. 7 | MBON-α3 exhibits long-lasting plasticity after olfactory conditioning and is required for 3-hr memory.

a) Example fluorescence voltage traces showing odor-evoked spiking responses of MBON-α3 neurons to 5-s presentations of an innately attractive CS^+ (1% ethyl acetate, *red*) or CS^- odor (apple cider vinegar, *blue*) in the pre-training (Pre) period, or at 5-min, 1-hr, 3-hr, 24-hr or 48-hr after aversive olfactory conditioning using the training protocol of **Fig. 3d**.

b, c) Traces showing the mean time-dependent rates of the rotational speed on the trackball for w^{1118}>*UAS-TnT* (**b**) or *MB093C>UAS-TnT* (**c**) flies, illustrating behavioral responses to the CS^+ and CS^- odors during testing bouts pre-training (Pre; top row), and at 5 min (middle row) or 3 hr after conditioning (bottom row). Each trace shows the mean response averaged over 10 different flies and the 3 testing bouts within each testing period (see **Fig. 3a**).

d,e) Plots show mean ± s.e.m. changes in rotational speed induced by CS^+ and CS^- odors in the pre-training (Pre), 5 min and 3 hr testing sessions for w^{1118}>*UAS-TnT* (**d**) or *MB093C>UAS-TnT* (**e**). Both CS^+ and CS^- odors were initially attractive and were either apple cider vinegar (ACV) or 1% ethyl acetate; assignments as CS^+ and CS^- were counterbalanced across 10 flies. w^{1118}>*UAS-TnT* flies exhibited behavioral conditioning to the CS^+ but not the CS^- odors at 5-min and 3-hr after training. (*P<0.05; **P<0.01; n = 10 female flies per genotype; Friedman ANOVA followed by post-hoc Wilcoxon signed-rank tests with Holm-Bonferroni correction). *MB093C>UAS-TnT* flies exhibited behavioral conditioning to the CS^+ odor at 5-min but not at 3-hr after training. Gray lines indicate data from individual flies. Thus, the inhibition of synaptic vesicle release in MBON-α3 impedes the longevity but not the formation of the associative memory.

Extended Data Fig. 8

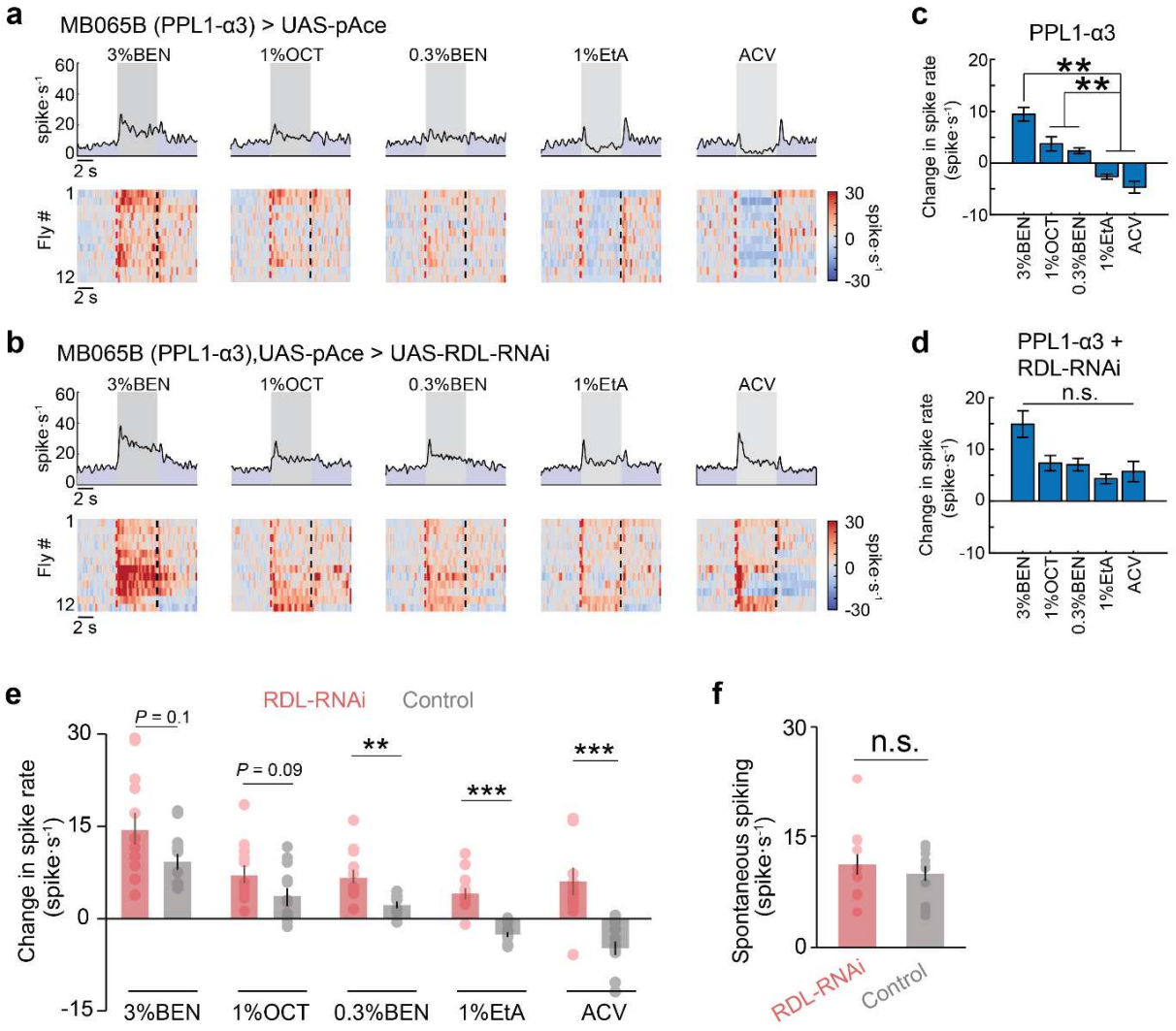

Extended Data Fig. 8 | The GABA-A receptor (RDL) is required for bidirectional encoding of innate odor-valence in the PPL1-α3 neuron.

a, b) *Top panels*, Time-dependent mean spiking rates of the PPL1-α3 neuron in control flies (*MB065B-GAL4>20×UAS-pAce*), **a**, and flies in which expression of the GABA-A receptor was selectively inhibited in PPL1-α3 using RNAi (*MB065B-GAL4,20×UAS-pAce>UAS-RDL-RNAi*), **b**, in response to 5 different odors (3% BEN, 1% OCT, 0.3% BEN, 1% EtA, and ACV). *Bottom panels,* Odor-evoked changes in spike rates, relative to baseline rates, in 12 individual flies, with each row showing single-trial data from an individual fly. Red vertical dashed lines mark the onsets of odor presentation, and the black vertical dashed lines mark the offsets.

c, d) Mean ± s.e.m. changes in spike rates measured during odor exposure (5 s durations) relative to baseline rates in PPL1-α3, in control flies (*MB065B-GAL4>20×UAS-pAce*), **c**, and flies in which GABA-A receptor expression was selectively inhibited in PPL1-α3 using RNAi (*MB065B-GAL4,20×UAS-pAce>UAS-RDL-RNAi*), **d**. (**P<0.05; 12 flies per group; Friedman ANOVA followed by post-hoc Wilcoxon signed-rank tests with Holm-Bonferroni correction).

e) Mean ± s.e.m. changes in spike rates measured during odor presentation (5 s duration) relative to baseline rates in the PPL1-α3 neuron in control flies (*MB065B-GAL4>20×UAS-pAce*) and the RNAi group (*MB065B-GAL4,20×UAS-pAce>UAS-RDL-RNAi*). (**P<0.01 and ***P<0.001; n = 12 flies; Mann-Whitney U-tests). Data points show measurements from individual flies.

f) Rates of spontaneous spiking by PPL1-α3 in the control group of flies (*MB065B-GAL4>20×UAS-pAce*) and the RNAi knockdown group (*MB065B-GAL4,20×UAS-pAce>UAS-RDL-RNAi*). (n.s. implies P > 0.05; n = 12 flies per group; Mann-Whitney U-tests).

Extended Data Fig. 9

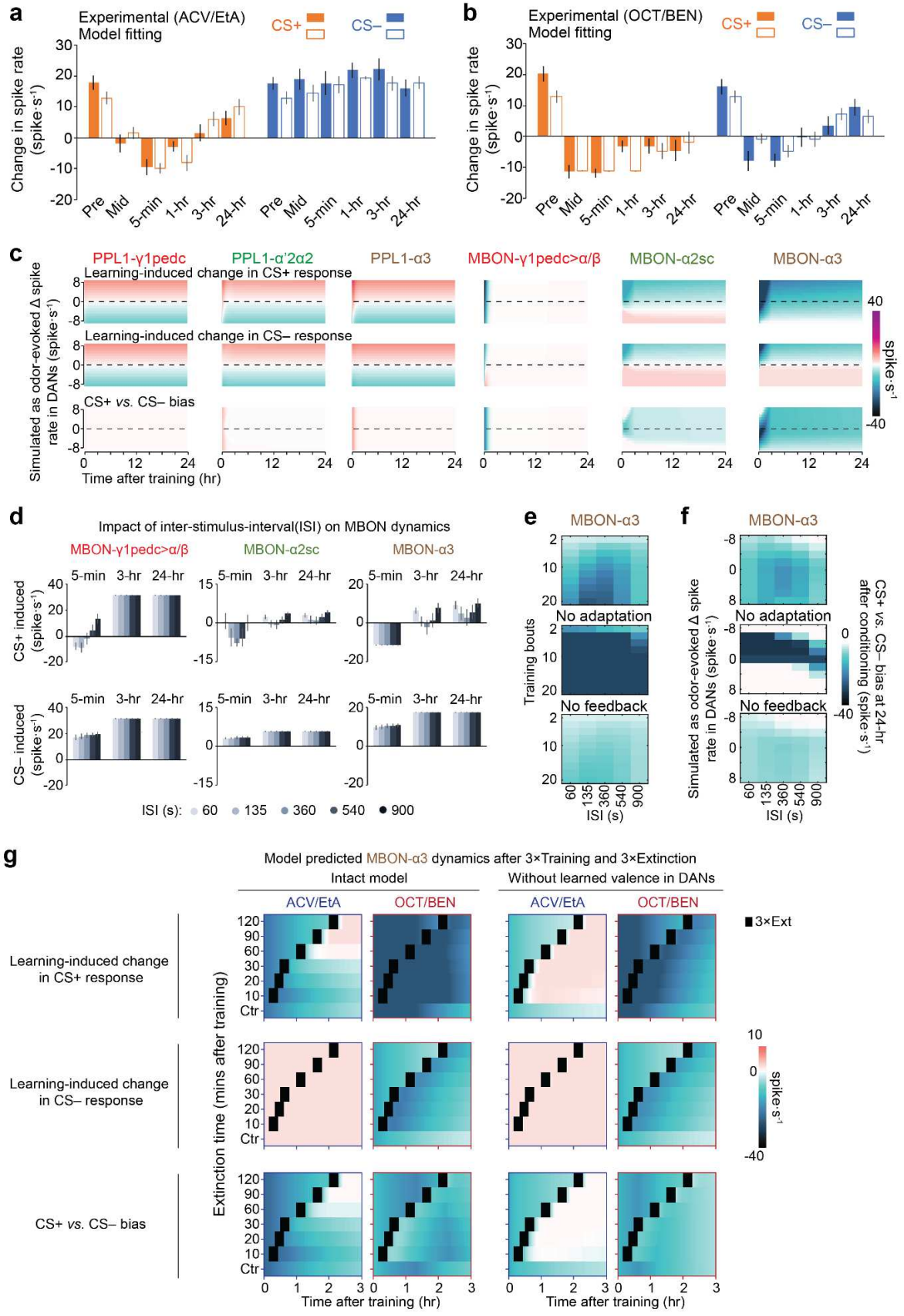

Extended Data Fig. 9 | A computational model of the mushroom body captures the interactions between learning units and yields predictions about the dynamics of memory storage and extinction.

a, b) Mean CS^-- and CS^+-evoked changes in spiking in MBON-α3 at different time points before, during and after olfactory conditioning, based on our experimental data (*solid bars*) or the computational model of the MB (*open bars*), for conditioning with attractive odor pairs (ACV and EtA), **a**, and repulsive odor pairs (OCT and BEN), **b**. For the experimental data, error bars show s.e.m. values over n = 12 flies. For the computational data, error bars span the 16%–84% C.I. based on results from 10,000 simulations (**Methods**).

c) We used the optimized computational model to examine conditioning-induced changes in odor-evoked spiking for the 3 PPL1-DANs and 3 MBONs in the model, following conditioning with one of 17 different hypothetical pairs of odors with varying innate valences as the CS^- and CS^+. Within each odor pair, the two odors have equivalent innate valences. In each of the plots, each row presents data for a single hypothetical odor or odor pair. The innate valence of each odor is specified by the change in DAN spiking that it evokes (*y*-axis values), relative to baseline spiking levels and prior to any associative conditioning. Using the model, we simulated 6 bouts of associative conditioning according to the protocol of **Fig. 3d**, using each of the 17 odors as either the CS^+ (top 6 plots) or the CS^- (middle 6 plots); these 12 plots show, as a function of time after training, the odor-evoked rates of PPL1-DAN and MBON spiking. The bottom 6 plots show how the biases between CS^+- and CS^--evoked spiking change as a function of time after training.

d) We used the computational model to evaluate how the inter-stimulus-interval (ISI) between CS^+ and CS^- presentations within a training bout influences MBON plasticity at different time points after training. Plots show the CS^+- (*top row*) and CS^--evoked (*bottom row*) spike rates in

each of the 3 MBONs in the model, at 5 min, 3 hr or 24 hr after 10 bouts of training using different ISI values (n = 10,000 simulations per ISI value; error bars span the 16%–84% C.I. percentiles). These computational studies used hypothetical odors with no innate valence for either the CS^+ or CS^-.

e) To explore how sensory adaptation and neural feedback from MBON-γ1pedc>α/β to the DANs influence the ISI-dependent plasticity, we used the optimized model to simulate the biases between CS^+- and CS^--evoked MBON-α3 spiking at 24 hr after different numbers of training bouts (*y*-axis values) occurring in immediate succession with different ISI values (*x*-axis values). These studies used hypothetical odor pairs with no innate valence. Plots show results from simulations in which the MB circuitry was intact (*top*), sensory adaptation was absent for both the CS^+ and CS^- odors (*middle*), or in which feedback signals from MBON-γ1pedc>α/β were absent (*bottom*).

f) We used the optimized model to simulate the biases between CS^+- and CS^--evoked MBON-α3 spiking at 24 hr after 10 training bouts of conditioning with one of 9 different hypothetical odors pairs with varying innate valence values (*y*-axis values). Plots show results from simulations in which the MB circuitry was intact (*top*), sensory adaptation was absent for both the CS^+ and CS^- odors (*middle*), or in which feedback signals from MBON-γ1pedc>α/β were absent (*bottom*).

g) To examine the effects of extinction training and the role of feedback signals from MBON-γ1pedc>α/β to the DANs, we used the optimized model to simulate extinction training (3 bouts of CS^+ and CS^- presentation but no US presentation) occurring at different times after the last conditioning bout. The plots show the model's predictions for the learning-induced changes in odor-evoked spiking in MBON-α3 across a 3-hr-duration following 3 bouts of conditioning. The different rows of each plot show the results for extinction sessions (marked with black

squares) occurring at distinct times after the last training bout; the bottom row shows results for simulations without extinction training. The simulations used pairs of odors that both had attractive innate valences (matched to those of apple cider vinegar, ACV, and 1% ethyl acetate, EtA) or both had aversive innate valences (matched to those of 1% 3-octanol, OCT, and 0.3% benzaldehyde, BEN). For the innately attractive odors, extinction training has the greatest effect when it occurs at substantial intervals after the end of conditioning. The left two columns show results from simulations using the intact model. The right two columns show results from simulations in which the feedback pathway from MBON-γ1pedc>α/β was inactivated.

Extended Data Fig. 10

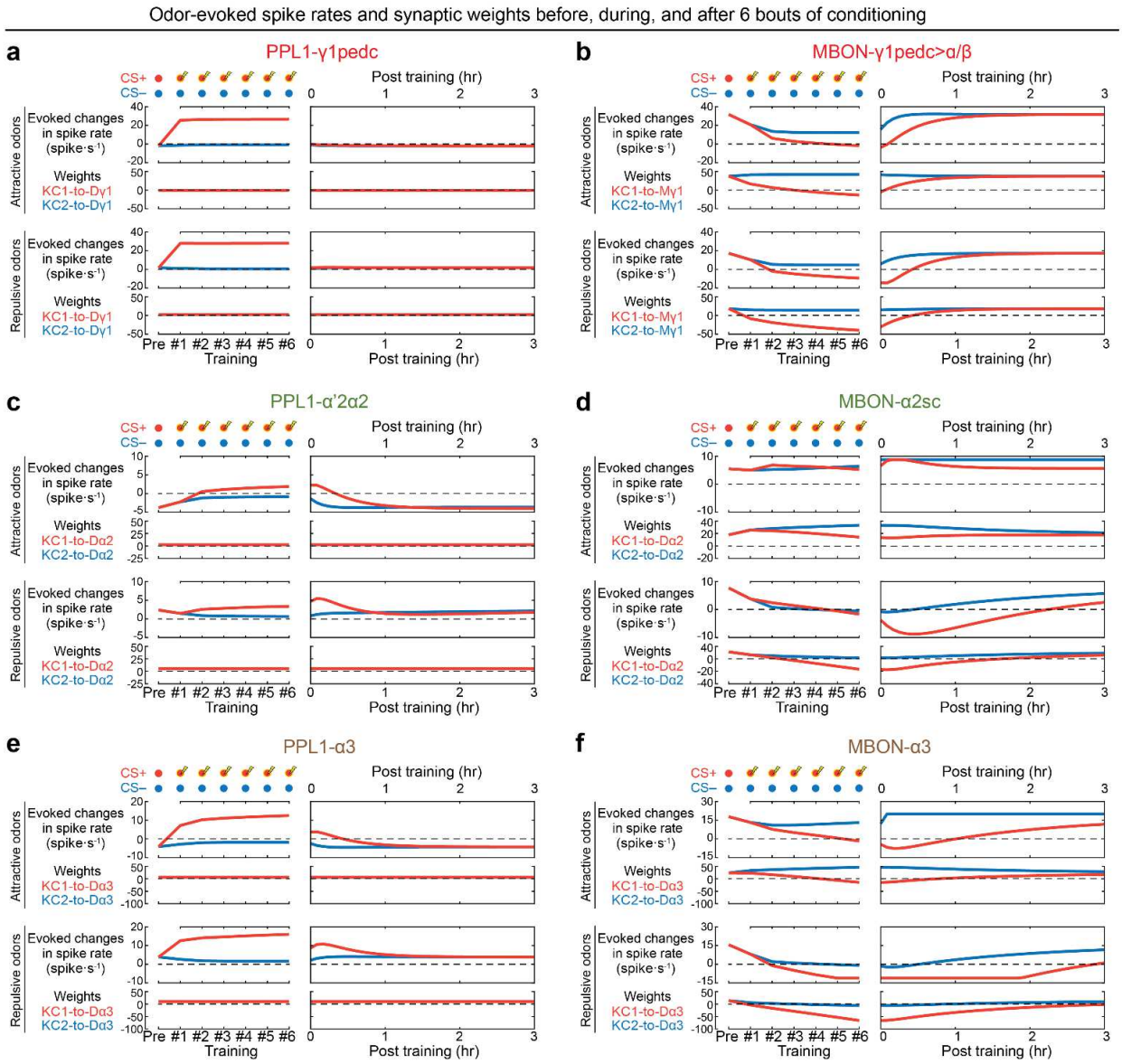

Extended Data Fig. 10 | Synaptic weight changes and stimulus-evoked spiking rates in the computational model of the mushroom body after 6 bouts of conditioning with attractive or repulsive odor pairs.

a–f) We used the optimized computational model to simulate the learning-induced changes in odor-evoked spiking rates and synaptic weights after 6 bouts of conditioning in the PPL1-γ1pedc (**a**), MBON-γ1pedc>α/β (**b**), PPL1-α'2α2 (**c**), MBON-α2sc (**d**), PPL1-α3 (**e**), and MBON-α3 (**f**) neurons. The simulations used pairs of odors that either both had attractive innate valences (top two rows of each panel; valences matched to those of apple cider vinegar, ACV, and 1% ethyl acetate, EtA) or both had aversive innate valences (bottom two rows of each panel; valences matched to those of 1% 3-octanol, OCT, and 0.3% benzaldehyde, BEN). The plots show model predictions for the learning-induced changes in odor-evoked spiking and synaptic weights at pre-conditioning (Pre) and during each of the 6 conditioning bouts (*left plots*), and across a 3-hr-interval after conditioning (*right plots*). The labels of the synaptic weights refer to the cell names, as defined in **Fig. 5a**. For the 6 conditioning bouts, we simulated neural responses to the paired presentation of the CS^+ odor and the US, whereas responses to CS^- odor were simulated in the absence of the US.

PPL1-γ1pedc elevated its spiking rate during paired presentations of the CS^+ and US, **a**, which led to reduced CS^+-evoked spiking by MBON-γ1pedc>α/β for up to 1 hr after training, **b**. Notably, CS^--evoked spiking by MBON-γ1pedc>α/β also decreased during conditioning, mainly due to sensory adaptation. In contrast, the CS^+-evoked spiking rates of the PPL1-α'2α2 and PPL1-α3 neurons, **c** and **e**, gradually increased across the 6 conditioning bouts and remained higher than CS^--evoked spiking rates up to 1 hr after training, due to the inhibitory feedback from MBON-γ1pedc>α/β. Under the combined influence of the innate and learnt odor valences

encoded by the PPL1-α'2α2 and PPL1-α3 neurons, the downstream MBON-α2sc and MBON-α3 neurons, **d** and **f**, exhibited valence-dependent spiking plasticity that persisted for an hour or more.

Extended Data Fig. 11

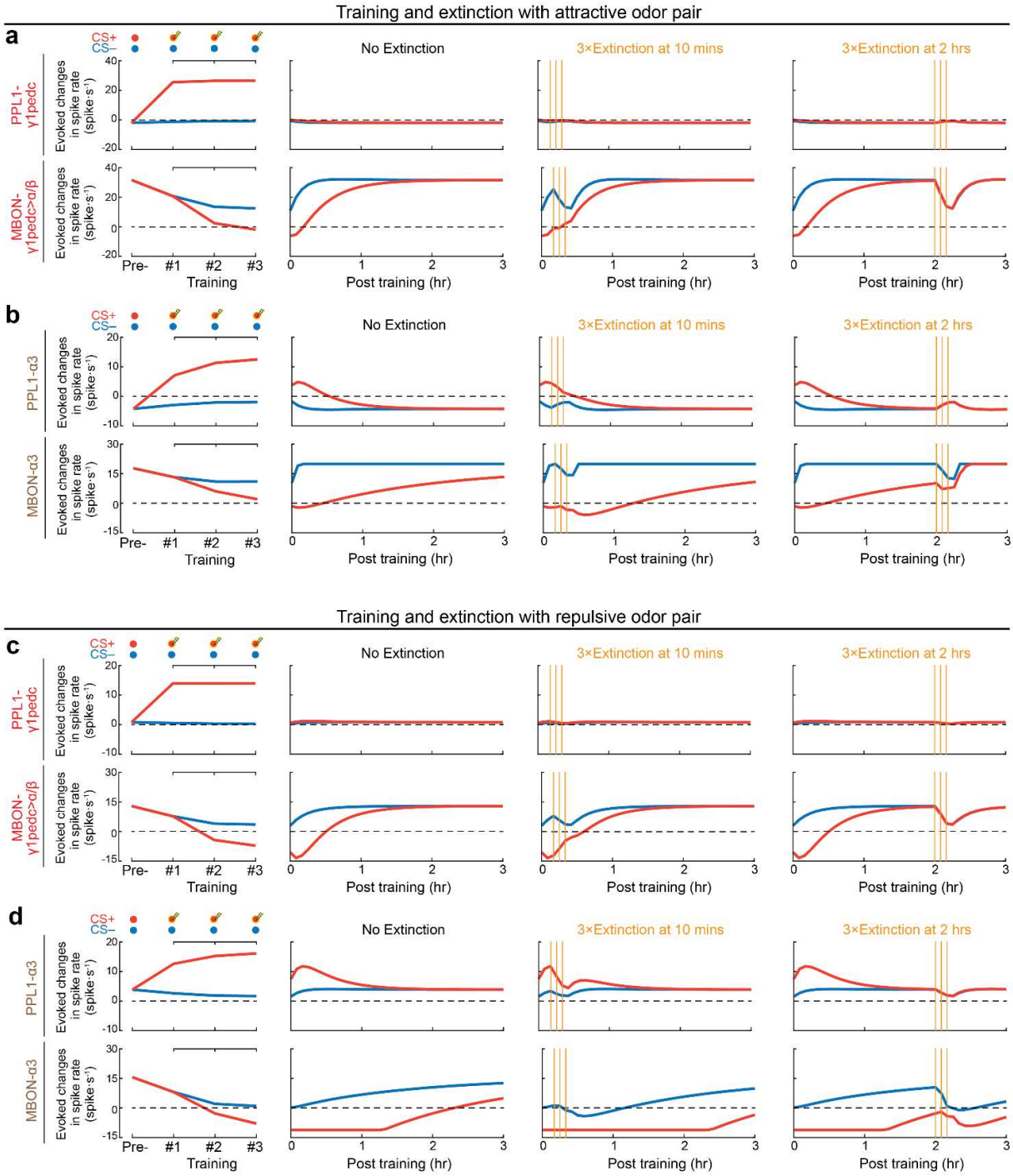

Extended Data Fig. 11 | Neural dynamics in short- and long-term memory modules during associative conditioning and extinction.

a,b) We used the optimized model to simulate the effects of different extinction training protocols (3 bouts of CS^+ and CS^- presentation but no US presentation; see **Fig. 5i**), in the short-term memory module (PPL1-γ1pedc and MBON-γ1pedc>α/β), **a**, and the long-term memory module (PPL1-α3 and MBON-α3), **b**. The simulations used pairs of odors that had attractive innate valences (matched to those of apple cider vinegar, ACV, and 1% ethyl acetate, EtA). The plots show model predictions for the learning-induced changes in odor-evoked spiking at a pre-conditioning time point (Pre) and during 3 successive training bouts (*left column*), across a 3-hr-duration after conditioning with either no extinction training (*middle left column*), or with extinction training at either 10 min (*middle right column*) or 2 hr (*right column*) after the end of conditioning. Vertical orange lines mark the times of 3 successive bouts of extinction training.

c,d) Plots analogous to those of panels **a** and **b** except that the odor pair used for conditioning had an aversive innate valence.

Notably, extinction training that occurs soon after associative conditioning can paradoxically extend the longevity of plasticity induced in the long-term memory by the associative conditioning. This effect arises due to the learnt valences that are encoded by PPL1-α3, which in turn result from the inhibitory feedback sent from the short-term memory module by MBON-γ1pedc>α/β. Owing to the learnt valence of the CS^+, an isolated presentation of an unpaired CS^+ soon after conditioning promotes extinction of the plasticity within the short-term memory module but reinforces the plasticity previously induced by associative conditioning within the long-term memory module.

Extended Data Fig. 12

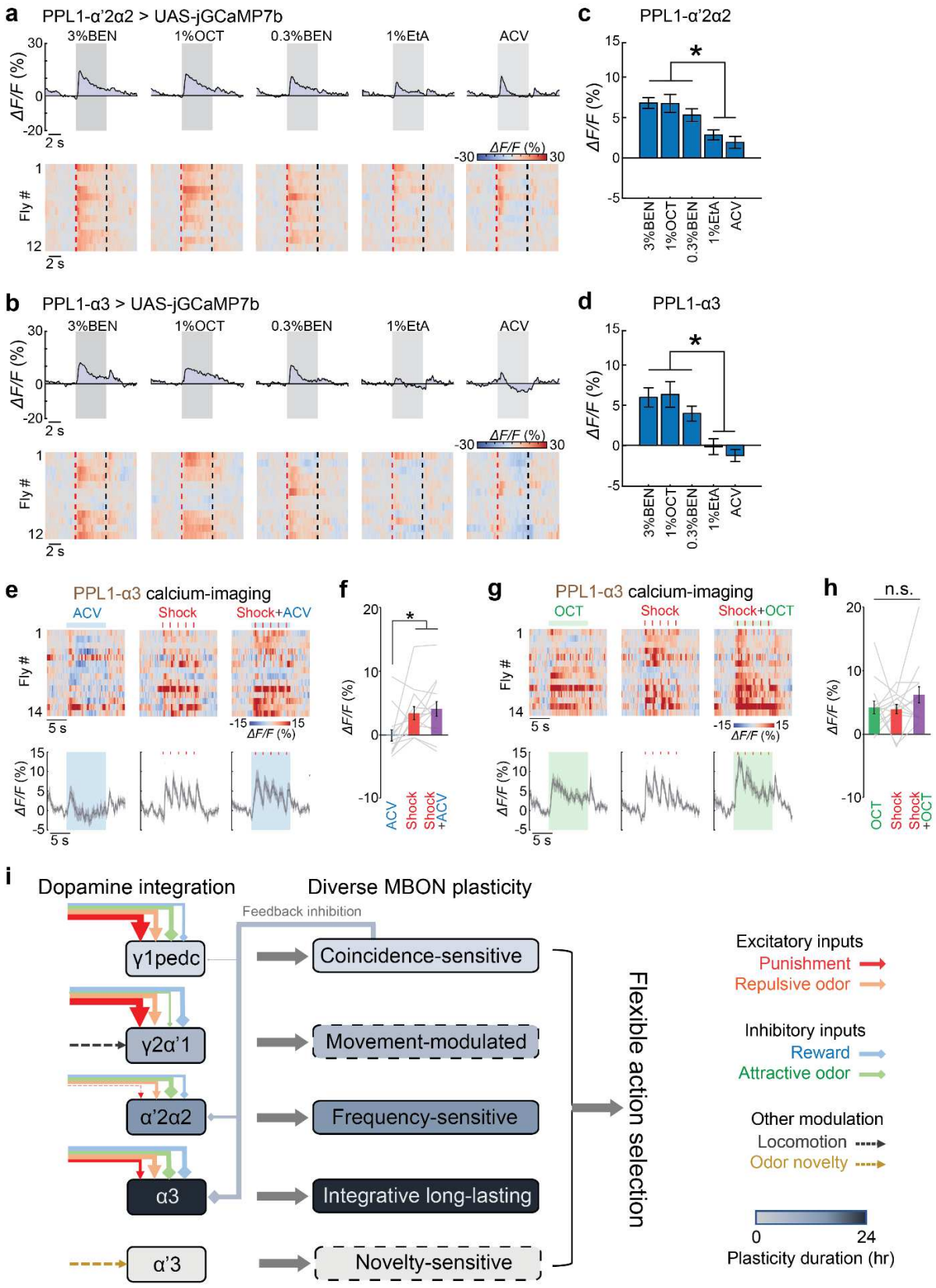

Extended Data Fig. 12 | Unlike voltage imaging, Ca^{2+} imaging does not accurately report decreases in spiking and thereby fails to capture the integration of valences encoded by the spiking of PPL1 dopamine neurons.

a,b) *Top plots*, Time-dependent mean fluorescence Ca^{2+} signals ($\Delta F/F$) evoked in the PPL1-α'2α2 (*R82C10-LexA>13×LexAop-jGCaMP7b*), **a**, and PPL1-α3 cells (*MB065B>20×UAS-jGCaMP7b*), **b,** by 5 different odors (3% BEN, 1% OCT, 0.3% BEN, 1% EtA, and ACV). Gray shading marks the duration of odor presentation. *Bottom plots,* Odor-evoked changes in Ca^{2+} activity in 12 individual flies. Each row shows data from a single fly. Vertical dashed lines mark the onset (red) and offset (*black*) of odor presentation. Comparison to **Extended Data Fig. 3f,g** shows that Ca^{2+} imaging poorly captures the bidirectional encoding of innate odor valences.

c,d) Mean changes in odor-evoked Ca^{2+} activity relative to baseline levels in PPL1-α'2α2, **c**, and PPL1-α3, **d**, averaged across the 5 s of odor presentation. Error bars: s.e.m. across 12 flies per neuron-type. (**P*<0.05; n = 12 flies; Friedman ANOVA followed by post-hoc Wilcoxon signed-rank tests with Holm-Bonferroni correction).

e) *Top*, Changes in Ca^{2+} activity ($\Delta F/F$) in the PPL1-α3 neuron immediately before, during and after 10-s-exposures to apple cider vinegar (ACV; horizontal blue line; *left*), 5 electric-shock pulses (each 0.2 s in duration with 1.8 s interval between pulses; red ticks mark the times of the individual shock pulses; *middle*), or the paired presentation of ACV and shocks (*right*) to n = 14 female flies (*MB065B>20×UAS-jGCaMP7b*; 1 trial per fly for each of the 3 stimulation conditions). *Bottom*, Traces showing the time-dependent mean Ca^{2+} activity, averaged over all 14 trials for each stimulus. Blue shading covers the periods of odor presentation. Gray shading on the time traces: s.e.m over 14 flies. Comparison to the data of **Fig. 4e,f** shows that Ca^{2+}

imaging poorly captures the ACV-evoked suppression of spiking and the encoding of the net valence of shocks paired with ACV presentation.

f) Mean ± s.e.m. odor-evoked changes in the Ca^{2+} activity of the PPL1-α3 neuron, as measured during 10-s-exposures to ACV (*blue bar*), 5 electric shocks (*red bar*), or the paired presentation of ACV and shocks (*purple bar*). (*P<0.05; n = 14 flies; Friedman ANOVA followed by post-hoc Wilcoxon signed-rank tests with Holm-Bonferroni correction).

g,h) Plots analogous to those of panels **e** and **f**, except that the odor presented (1% OCT) was innately repulsive.

i) Schematic showing how the parallel-recurrent circuitry of the mushroom body (MB) may allow the integration of innate and learnt valence signals in a heterogeneous manner across the different learning units. PPL1-DANs innervate different compartmentalized regions on Kenyon cells (KC) axons and form parallel learning units together with their corresponding downstream mushroom body output neurons (MBONs). Sensory stimuli with innate negative valences, such as punishments (*red*) and repulsive odors (*orange*), heterogeneously excite PPL1-γ1pedc, PPL1-γ2α'1, PPL1-α'2α2, and PPL1-α3. Whereas sensory stimuli with positive valences, such as rewards (*blue*) and attractive odors (*green*), inhibit the 4 PPL1-DANs. During associative conditioning with an aversive US, each individual PPL1-DAN may integrate the valences of stimuli presented concurrently and provide a distinctive teaching signal that drives a depression of KC→MBON synapses. Plasticity in MBON-γ1pedc>α/β lasts for ~1 hr and reduces the strength of the inhibitory feedback from MBON-γ1pedc>α/β to PPL1-α'2α2 and PPL1-α3, which in turn facilitates the formation of long-lasting plasticity in those learning units. In addition, the PPL1-γ2α'1 neuron is modulated by the fly's movement[25,62], whereas PPL1-α'3 seems to encode odor novelty[48]. Owing to the integration of the innate and learnt valences encoded by PPL1-DAN

spiking and to the varying durations of MBON plasticity, the MB's parallel-recurrent circuitry can enact diverse plasticity patterns that shape fly behavior in a flexible manner.

Video 1 | High-speed voltage imaging at single spike resolution in a behaving fly.

Bottom left, Video of a fly running in place on a trackball under the microscope objective lens that we used for high-speed fluorescence voltage imaging of the fly's neural activity. The frame acquisition rate of the fly behavior movie was 30 fps. *Bottom right*, Time traces of the fly's forward running speed and rotational speed on the trackball. *Top left*, Voltage-imaging movie, recorded simultaneously with the behavioral video, showing the fluorescence changes of the Ace2N-mNeon-v2 voltage indicator in a pair of MBON-γ1pedc>α/β neurons located in opposite hemispheres of the fly brain. The voltage movie was recorded at a frame rate of 500 fps. To synchronize playback with the behavior movie, we subsampled 1800 frames out of the 30,000 frame-long voltage movie and displayed it at 30 fps. *Top right*, Fluorescence traces and spike raster plots show the spiking dynamics of the two MBON-γ1pedc>α/β neurons.

Video 2 | Spike backpropagation into the dendritic tree of an MBON-γ1pedc>α/β neuron.

A movie of the spike-triggered average fluorescence responses ($\Delta F/F$) before, during and after firing of an action potential in the MBON-γ1pedc>α/β neuron of **Extended Data Fig. 2a**, imaged using the pAce voltage indicator in a behaving fly. The movie shows the time-dependent, mean fluorescence changes averaged over 846 identified spikes from –3 ms to 3 ms relative to the time of the action potential peak within the dendritic tree. Depolarization starts at about –1.5 ms in a region adjacent to one of the axon branches, propagates to the soma and other axon branches, and backpropagates into the dendritic tree. The interval between successive image frames is 50 μs, which we achieved through spline interpolations from the original 1000 fps acquisition rate. The playback speed is 10 fps. Scale bar: 10 μm.

Methods

Fly stocks

The FlyLight Project Team at Janelia Research Campus kindly provided the split-GAL4 *MB504B-GAL4*, *MB502B-GAL4*, *MB065B-GAL4*, *MB304B-GAL4*, *MB085C-GAL4*, *MB093C-GAL4*, *MB080C-GAL4*, *MB077B-GAL4*, and *MB542B-GAL4* flies. We obtained *R82C10-LexA* (#54981), *20×UAS-jGCaMP7b* (#79029), *13×LexAop-jGCaMP7b* (#80915), *UAS×RDL-RNAi* (#52903), and *UAS-TnT* (#28838) flies from the Bloomington Stock Center. Ron Davis (Scripps Institute) kindly provided *TH-LexA* flies, and David Anderson (Caltech) provided *20×UAS-CsChrimson-tdTomato* flies. We outcrossed all strains with w^{1118} wild-type flies for 5 generations to minimize differences in genetic background.

To create *20×UAS-Ace2N-mNeon-v2*, *20×UAS-pAce* and *13×LexAop-pAce* flies that express the Ace2.0 and pAce FRET-opsin voltage indicators[37,38], we synthesized codon-optimized *Ace2N-mNeon-v2* and *pAce* genes (GeneScript Biotech) with a *Drosophila* Kozak sequence before the start codon. We then sub-cloned the *Ace2N-mNeon-v2* and *pAce* cDNA into the XbaI and XhoI restriction sites of the *pJFRC7-20×UAS-IVS-mCD8::GFP* and *pJFRC19-13×LexAop2-IVS-myr::GFP* vectors (Addgene #26220 and #26224). After verifying the constructed plasmids *pJFRC7-20×UAS-IVS-Ace2N-mNeon-v2*, *pJFRC7-20×UAS-IVS-pAce*, and *pJFRC19-13×UAS-IVS-pAce* with sequencing, we used a commercial transformation service (Bestgene Inc) to create two transgenic fly lines for each construct by inserting them into two phiC31 docking sites, the attP40 on the second chromosome and VK00027 on the third chromosome, for further combination with GAL4 or LexA driver lines.

We performed all imaging and behavioral experiments using female flies (3–8 d old at the time of laser surgery). We raised flies on standard cornmeal agar media with a 12 hr light/dark

cycle at 25°C and 50% relative humidity. Before surgery or behavioral tests, we chose flies informally in a random manner from a much larger group raised together for all studies; there was no formal randomization procedure for selecting flies. **Extended Data Table 1** contains the lists of transgenic fly lines we created for this study, as well as the genotypes and total number of flies used in each imaging and behavior experiment and for each figure panel. When imaging flies with more than one fluorescently labeled neuron-type, in most cases we focused on one neuron-type per fly in order to achieve recordings with a sufficiently high signal-to-noise ratio (SNR). However, in a subset of flies we were able to image 2 or even 3 neuron-types concurrently with satisfactory SNR values. Therefore, the total number of flies that we imaged is less than the sum of the n-values reported in the figure panels.

Odorants

We tested flies' responses to the following monomolecular odors: Ethyl acetate (EtA; CAS# 141-71-6, Sigma-Aldrich Inc.), Isoamyl acetate (IAA; CAS# 123-92-2, Sigma-Aldrich Inc.), Benzaldehyde (BEN; CAS# 100-52-7, Sigma-Aldrich Inc.), 1-octen-3-ol (1O3O; CAS# 3391-86-4, Sigma-Aldrich Inc.) and 3-Octanol (OCT; CAS# 589-98-0, Sigma-Aldrich Inc.). We diluted EtA, IAA, 1O3O, and OCT into 1% and 10% concentrations and BEN into 0.3% and 3% concentrations (V/V) with mineral oil. We also tested a natural odor: apple cider vinegar (ACV; Bragg Inc.).

Mounting of flies for behavioral, voltage-imaging or optogenetic experiments

In brief, to mount flies for on-ball behavioral experiments or *in vivo* imaging studies, we anesthetized them on ice for 1 min. We then transferred them to the cooled surface (~4 °C) of an aluminum thermoelectric cooling block. While viewing the fly through a dissection microscope (Leica MZ6) and by using a multi-axis stage to manipulate the entire cooling block, we brought

the posterior of the fly's thorax into contact with a 125-μm-diameter fused silica optical fiber (Nufern; PLMA-YDF-10/125) on a custom-made plastic fixture that was secured on the mounting apparatus directly above the fly. We applied ~1 μL of ultraviolet (UV) light-curing epoxy (NOA 89, Norland) to the contact point between the fiber and the fly's thorax and cured the epoxy with UV light for 30 s. Finally, to reduce head motion, we fixed the fly's head to the thorax using UV epoxy, after which we considered the fly to be fully mounted.

Laser microsurgery

To create an imaging window in the fly cuticle, we used a laser microsurgery system based on a 193-nm-wavelength excimer laser (GamLaser; EX5 ArF), as detailed in our prior work[33,40,41]. After transferring a mounted fly to the surgery station, we created an optical window in the cuticle by laser drilling a 150-μm-diameter hole (30–40 laser pulses, delivered at 100 Hz, 36 mJ per pulse as measured at the specimen plane). This microsurgical procedure generally removed the cuticle, air sacs and fat bodies, exposing the underlying brain tissue. Occasionally, further rounds of laser dissection or manual cleaning of the cuticle were needed due to variations in head size and fly age. Immediately after surgery, we applied 1 μL of UV epoxy (NOA 68, Norland; Refractive index: 1.54; Transmission 420–1000 nm: ~100%) and cured it for 30 s to seal the cuticle opening; we did this under a dissection microscope while using a desktop ultrasonic humidifier (Air-O-Swiss; AOS 7146) to keep the local environment around the fly at ~60% humidity. After mounting the fly, we put a coverslip (22 × 22 mm, No. 0, Electron Microscope Sciences) above the fly's head and placed a small drop (~1 μL) of water between the coverslip and the fly cuticle.

High-speed fluorescence voltage imaging

To image neuronal voltage dynamics, we used a custom-built upright epi-fluorescence

microscope and a 1.0 NA water-immersion objective 20× (XLUMPlanFL, Olympus). We used a 503/20 nm excitation filter (Chroma), a 518 nm dichroic mirror (Chroma), and a 534/30 nm emission filter (BrightLine). Using the 500-nm wavelength module of a solid-state light source (Spectra X, Lumencor), we illuminated the sample with 3–7 mW/mm^2 of illumination at the specimen plane. We acquired images at 1000 Hz, using a scientific-grade camera (Zyla 4.2, Andor) and 2 × 2 pixel binning. For Ca^{2+} imaging experiments, we used the same setup and illumination conditions but acquired images at 100 Hz.

Odor delivery to awake flies

To deliver odors to flies' antennae, we used a custom-built olfactometer that delivered a constant airflow (200 mL/min) to the fly via either a control path (air passed through mineral oil) or via an odor path (air passed through mineral oil with dissolved odorant). Airflow and odors went through a probe needle (1.7-mm-inner-diameter, Grainger Inc.) placed at a 45 deg. angle in the horizontal plane and ~3 mm away from the fly's antennae on the right side (**Fig. 2e**). Each trial lasted for 15 s and odor was delivered from the 5th to the 10th second. For all experiments in which we studied a fly's responses to multiple different odors, we presented the odors in a pseudo-random order with intervals of at least 2 mins between odors. During neural imaging experiments, as we delivered odors we imaged neuronal voltage dynamics through the transparent window in the cuticle made above the brain's right hemisphere by laser microsurgery.

Electric shock and sucrose delivery

To deliver electric shocks to a fly, we glued a pair of electric wires (0.4 mm diameter; R26Y-0100; OK Industries) to both sides of the thorax with electrically conductive glue (Wire Glue). After the glue dried, the resistance between the two wires was 10–30 MΩ. During each 15-s-imaging-trial, we delivered 5 electric shocks (0.2-s-long, 20-V-pulses delivered 1.8 s apart)

using a constant voltage stimulator (STM200; Biopac Systems, Inc.) starting 5 s after trial onset.

To image neural responses to sucrose feeding, we positioned the tip of a microliter syringe (Microliter™#701; Hamilton) ~1 mm below the fly's proboscis. By manually pushing the microliter syringe to deliver ~1 μL of saturated sucrose solution, we allowed the fly to sample the liquid with its proboscis, inducing feeding. During each 15-s-imaging-trial, we delivered the sucrose solution from the 5th to the 10th second.

Measurements of fly locomotion on the trackball

To track the locomotion of individual flies walking on a trackball (**Fig. 2e–h**; **Fig. 3a–c**; **Fig. 4m,n**; **Extended Data Fig. 3b,c**; **Extended Data Fig. 7b–e**), we used a setup similar to that of prior studies[84–86]. Two optical USB pen mice (Finger System, Korea) were aimed at the equator of an air-suspended, hollow high-density polyethylene ball (6.35-mm diameter; ~80-mg mass; Precision Plastic Ball Co.). The pen mice were 2.3 cm away from the ball and tracked the ball's rotational motion at a readout rate of 120 Hz. We converted the pair of digital readouts from the pen mice into a forward displacement on the ball plus a rotational angle for each time bin, and then we computed the fly's forward and turning velocities using custom software written in Matlab (v2018b; MathWorks).

Olfactory conditioning on the trackball

After mounting flies and attaching electric wires to the thorax (see above), we positioned flies on the trackball using a three-dimensional translation stage. Before olfactory conditioning began, we allowed the flies to rest on the trackball for at least 30 min to minimize the impact of the cold anesthesia used during the mounting process. For all conditioning studies, we used two attractive odors, apple cider vinegar (ACV) and 1% ethyl acetate (EtA), each of which served as either the CS^+ or CS^- in a counterbalanced manner across the flies used in each group. A 1-hr memory

experiment comprised 1 training session and 3 testing sessions (**Fig. 3b,c**)

In the training session, we delivered 6 bouts of CS^+ and CS^- odor pairs to flies sequentially (30 s per odor exposure, with 135 s of fresh air between successive odors). During delivery of the CS^+ odor, we also administered to the fly 16 electric shock pulses of 20 V amplitude (each pulse of 0.2 s duration, with 1.8 s between successive pulses), starting 3 s after the onset of the CS^+ odor.

In each testing session, we delivered 3 bouts of CS^+ and CS^- odor pairs to flies (5 s per odor exposure, with 60 s of fresh air between presentations of the CS^+ and CS^- odors and also between bouts). We recorded the flies' forward and turning velocities on the trackball in the 3 testing sessions ('Pre', '5-min', '1-hr'). The 'Pre' session occurred 5 mins before the training session and determined the odor-induced behavior of the flies while they were still naïve. The '5-min' and '1-hr' memory testing sessions respectively began 5 mins and 1 hr after the end of the training session. In a 3-hr memory experiment (**Fig. 4m,n**; **Extended Data Fig. 7b–e**), the third testing session occurred 3 hr after the training session (referred to as '3-hr').

To minimize the bias of flies' turning behavior on the trackball, we delivered odors to the left side of flies' antennae in half of the experiments and to the right side in the other half. Positive values of the fly's walking speed represent forward-walking, whereas negative values represent backward-walking. Positive values of the rotational velocity indicate that the fly turned toward the direction of odor delivery, whereas negative values indicate the fly turned in the opposite direction.

Measurements of conditioning-induced neural plasticity

After mounting flies and attaching a pair of wires to deliver electric shocks to the thorax (see preceding section), we allowed flies to rest for >30 min before training so as to minimize the

impact of the cold anesthesia we had used during the mounting process. Each 1-hr imaging experiment to study memory comprised 2 training and 4 testing sessions (**Fig. 3d**).

Each fly first underwent 1 bout of imaging before conditioning (Pre), in which we examined the neuronal spiking responses to the 2 odors to be used during conditioning (CS^+ and CS^-; each odor presented for a duration of 5 s with an interval of 60 s between successive odors). Next, we subjected each fly to 3 bouts of training, in each of which the fly received a paired presentation of the CS^+ (30 s in duration) and the unconditioned stimulus (US, 16 pulses of 0.2-s-duration, 20-V-amplitude electric shock spaced 1.8 s apart; the first pulse started at 3-s after the onset of the CS^+), and an unpaired presentation of the CS^- (30 s in duration, with 135-s intervals between successive odors). Five minutes after the end of the training bouts, each fly underwent a mid-training (Mid) imaging bout to assess the odor-evoked spiking responses. At 5 min after the end of the Mid imaging bout, we subjected each fly to 3 more bouts of training. Then, the fly underwent another 2 imaging bouts at 5 min and 1 hr after the training, respectively.

In 24-hr memory imaging experiments (**Fig. 4a–d**), we used an identical protocol for odor and shock delivery as that in the 1-hr-experiments, except that we added two more testing sessions at 3 hr and 24 hr after training. We kept flies glued on the optical fiber across the entire 24 h period and fed them with sucrose water 3 min after the '3-hr' session and again at 30 min before the '24-hr' session.

In experiments studying memory extinction, we used 3 groups of flies: a control group that received memory training (3 bouts of CS^+/US association as in the training session of 1-hr-experiments), an 'early' extinction group that received memory training and then underwent an extinction session starting 10 min after the end of the training, and a 'late' extinction group

that received training and then underwent an extinction session starting 2 hr after training. For all 3 groups, we imaged the neural activity in 3 testing sessions ('Pre', '5-min', and '3-hr'). The 'Pre' session was 5 mins before the training session; the '5-min' and '3-hr' sessions respectively started 5 mins and 3 hr after the end of the training session. The extinction session involved 3 bouts of CS^+ and CS^- odor exposure as in the training session but without electric shocks.

Analyses of imaging data

To extract traces of neuronal voltage activity, we first used an algorithm, NoRMCorre[87], to correct computationally the raw (1 kHz) fluorescence videos (see **High-speed fluorescence voltage imaging** above) for lateral displacements of the brain. To improve the signal-to-noise ratios of the videos, we applied a denoising algorithm based on a singular value decomposition (SVD). This involved first reshaping the raw video into a matrix $\mathbf{Y} \in \mathbb{R}^{p \times d}$, where p is the total number of video frames and d is the number of pixels in the field of view. We then decomposed $\mathbf{Y}$ as a product, $\mathbf{Y} = \mathbf{UC}$, where $\mathbf{U}$ is a set of k low-rank components $\mathbf{U} \in \mathbb{R}^{p \times k}$, and $\mathbf{C} \in \mathbb{R}^{k \times d}$ are weighting coefficients. The components $\mathbf{U}$ are assumed to be semi-unitary, without loss of generality, and were obtained by computing the SVD of $\mathbf{Y}$. The number, k, of low-rank components that we retained in $\mathbf{U}$ was determined by requiring that the set of retained singular vectors captured >95% of the variance in the raw video. We then calculated the coefficients as $\mathbf{C} = \mathbf{U}^T\mathbf{Y}$. For each row of the coefficient matrix, after reshaping it back into a two-dimensional image we applied the BM3D image denoising algorithm[88], which applies a nonlinear thresholding operation to obtain a denoised set of coefficients, $\widehat{\mathbf{C}}$. We determined the denoised video as $\widehat{\mathbf{Y}} = \mathbf{U}\widehat{\mathbf{C}}$ and reshaped it back to its original dimensions.

After denoising the fluorescence videos, we manually selected 1 to 3 regions-of-interest (ROIs) that contained the anatomical structures of the targeted cell-types expressing the voltage

indicator (**Extended Data Fig. 1** shows ROIs for all fly lines used for imaging). We then computed spatially-averaged, time-dependent changes in relative fluorescence intensity, $\Delta F(t)/F_0$, where F_0 was the mean fluorescence in the ROI averaged over the entire video. Next, we computationally corrected the resulting fluorescence traces for photobleaching by parametrically fitting a sum of two exponential functions to the mean fluorescence trace, F_0, and then normalizing F_0 by the parametrically fitted trace. To identify neural spikes, we high-pass filtered the $\Delta F(t)/F_0$ trace by subtracting a median-filtered (40 ms window) version of the trace and then identifying as spikes the local peaks that surpassed a threshold value. Due to the distinct spiking rates and signal-to-noise ratios for different cell-types, we used different threshold values for spike detection in different cell-types (>3 s.d. for PPL1-DANs and MBON-α2sc, >2 s.d. for MBON-γ1pedc>α/β and MBON-γ2α'1, >2.5 s.d. for MBON-α'2, -α3 and -α3). We calculated the spiking rate using the number of spikes that occurred over within a sliding 100-ms window.

To computed mean spike waveforms, we temporally aligned each identified spike within a trial to the time at which its peak value of $\Delta F(t)/F_0$ occurred. We then performed a spline interpolation (10 μs sampling) of the mean waveform and from the resultant determined the spike amplitude.

We also used a signal detection framework to compute the spike detection fidelity, d', which characterizes the ability to correctly distinguish instances of a spike from background noise fluctuations within the fluorescence trace[37,42]. As described in our prior work[42], when we use N successive samples from a photodetector, $F = (F_1, F_2, \ldots, F_N)$, to detect spikes, the distribution of F follows Poisson statistics in the shot-noise-limited regime. We can use the distribution to express two mutually exclusive hypotheses: the null hypothesis, $H^{(0)}$, which posits the absence of a spike; and the alternative, $H^{(1)}$, which posits that a spike occurred at time zero.

The d' value was calculated as $d' = (\mu_L^{(1)} - \mu_L^{(0)})/\sigma_L$, in which μ_L and σ_L represent the mean and variance of the distributions of the log-likelihood ratio, $L(f)$, of the two hypotheses.

The mean, μ_L, and variance, σ_L, of the distribution of $L(f)$ under the null hypothesis $H^{(0)}$ of no spike having occurred and under the alternate hypothesis $H^{(1)}$ that a spike occurred are given by:

$$\mu_L^{(0)} = \frac{F_0}{\nu}\sum_{n=1}^{N} log(1 + s_n) - \frac{F_0}{\nu}\sum_{n=1}^{N} s_n$$

$$\mu_L^{(1)} = \frac{F_0}{\nu}\sum_{n=1}^{N} (1 + s_n) log(1 + s_n) - \frac{F_0}{\nu}\sum_{n=1}^{N} s_n$$

$$\sigma_L \approx \sigma_L^{(1)} \approx \sigma_L^{(0)} = \sqrt{\frac{F_0}{\nu}\sum_{n=1}^{N} log^2(1 + s_n)} \quad ,$$

where ν denotes the sampling rate, F_0 represents the baseline fluorescence intensity from time periods that contained no neural spike, and s_n is the mean fluorescence signal at each time bin within a time period that contains the averaged waveform of the identified spikes for each imaging trial ($N = 51$ bins; 1 ms per bin).

Odor classification

For odor classification analysis (**Fig. 2l**), we used PyTorch[89] (version 1.7.1; www.pytorch.org) to train computational classifiers that identified odors based on patterns of PPL1-DAN or MBON neural population activity. Since we imaged different cell-types in different flies, we first constructed datasets of neural population responses from 'virtual flies'[49] by combining data from the 5 subtypes of PPL1-DANs or the 6 subtypes of MBONs to produce aggregate PPL1-DAN or MBON population datasets. For each cell-type, we used recordings from 12 different real flies

and their neural responses to each of 5 odors. To construct a dataset of PPL1-DAN neural population odor-evoked responses for an individual virtual fly, we randomly selected 1 of the 12 real flies studied for each of the $N_{\mathrm{PPL1}} = 5$ different PPL1-DAN cell-types and combined their odor-evoked responses. This enabled us to create response datasets for 12^5 different virtual PPL1-DANs, each of which responded to $N_{\mathrm{Odors}} = 5$ different odors. We used an analogous approach to construct datasets of MBON neural population odor-evoked responses and combined the data from randomly selected flies for each of the $N_{\mathrm{MBON}} = 6$ different MBON-types. Although this approach would have allowed us in principle to create 12^6 different datasets of virtual MBON population responses, in practice we constructed only 12^5 such datasets so as to have an equal number of MBON and PPL1-DAN virtual flies. To create shuffled datasets, we took the same two sets of 12^5 virtual flies and within each set we randomly reassigned the neural responses across the set of odors.

To create classifiers of odor identity based on the odor-evoked neural population responses of virtual flies, we randomly assigned 90% of the virtual flies to a training set, 5% of the virtual flies to a validation set, and the remaining 5% to a testing set. We used the validation set to evaluate trained classifiers and tune hyperparameters, whereas we only used the testing set at the very end to determine the rate of correct classifications attained with the optimized classifier. We used linear support vector machines (SVMs)[90] to create a multiclass linear classifier of odor identity. To perform odor classification using the set of all $N_{\mathrm{Odors}} \cdot 12^5$ virtual PPL1-DAN odor-evoked responses, we created a vector classifier function, **f**, whose value for the i^{th} odor-evoked neural response ($1 \leq i \leq N_{\mathrm{Odors}} \cdot 12^5$) was

$$\mathbf{f}\,(x_i, W_{PPL1-DAN,}, b) = W_{PPL1-DAN}\, x_i + b\,,$$

where $W_{PPL-DAN}$ is a matrix of size $N_{\mathrm{Odors}} \times N_{\mathrm{PPL1}}$, x_i is a vector of size N_{PPL1} that expresses the

PPL1 responses of a specific virtual fly to one of the odors, and b is a bias vector of size N_{Odors}. For computational purposes, we rewrote f as

$$\mathbf{f}(x'_i, W) = Wx'_i,$$

where W is a matrix of size $N_{\text{Odors}} \times (N_{\text{PPL1}}+1)$ comprising $W_{PPL1-DAN}$ in its top N_{PPL1} rows and the vector b in its last row, and x'_i is a vector of size $(N_{\text{PPL1}}+1)$ comprising x_i in its first N_{PPL1} entries and 1 in its last entry. Given a set of odor-evoked neural responses, the multiclass linear classifier predicted the odor identity, j $(1 \le j \le N_{\text{Odors}})$, as $argmax_j \{\mathbf{f}(x'_i, W)\}$, *i.e.* according to which entry of the vector classifier function yielded the maximum value.

To train the model, we optimized W by using a hinge loss function that penalized incorrect odor predictions. For the i^{th} odor-evoked response $(1 \le i \le N_{\text{Odors}} \cdot 12^5)$, its contribution to the total loss was found by summing the penalties incurred for all incorrect classifications

$$loss_i(W) = \sum_{j \neq odor_{true,i}} max\left(0, \mathbf{f}\left(x'_i, W\right)_j - \mathbf{f}\left(x'_i, W\right)_{odor_{true,i}} + 1\right),$$

where the index j runs over the individual odors, $odor_{true,i}$ refers to the odor that evoked the *i'th* neural response and which is thus the correct classifier result for the *i'th* response, and 1 is used as a margin to help enforce successful classifications. To optimize W, we averaged the loss function across individual batches of $N_{batch} = 200$ odor responses randomly chosen without replacement from the full set of $N_{\text{Odors}} \cdot 12^5$ responses, with inclusion of an L_2 regularization penalty to minimize the entries of W:

$$loss(W) = \frac{1}{N} \sum_i \sum_{j \neq odor_{true,i}} max\left(0, \mathbf{f}\left(x'_i, W\right)_j - \mathbf{f}\left(x'_i, W\right)_{odor_{true,i}} + 1\right) + \lambda \sum_k \sum_l W_{k,l}^2 .$$

Here $\lambda = 10^{-4}$ is an L_2 regularization hyperparameter that we optimized empirically using the validation dataset. We then used the Adam optimizer to update the matrix elements of W:

$$W := W - \alpha \cdot Adam(\nabla_W loss(W)),$$

where $\alpha = 5 \cdot 10^{-4}$ is a hyperparameter that specifies the learning rate and that was optimized using the validation dataset, and $Adam(\nabla_W loss(W))$ refers to the Adam optimizer, an extension of stochastic gradient descent that provides superior convergence through adjustments of the learning rate during training. (We used the Adam optimizer's standard parameter values for adjusting the learning rate[91]). To train the classifier, we optimized W by updating its matrix elements across 10 full passes through the entire set of $N_{\text{Odors}} \cdot 12^5$ odor responses. Empirically, we found that additional training did not further improve classification accuracy. We used the same procedures and optimization parameters for training odor classifiers based on the set of odor-evoked MBON responses.

Finally, to test the performance of our classifiers, we divided the testing dataset of virtual flies into 120 different sub-testing sets each with 100 different virtual flies, each with 5 different odor responses. For each sub-testing set, we computed the classification performance as the sum of the number of correctly identified odors divided by 1000. The box-and-whisker plot of **Fig. 2l** shows the distribution of classification performance values across these 120 different datasets.

Optogenetic studies

To provide all-trans-retinal, an essential cofactor for CsChrimson activation[92], we dissolved all-trans-retinal powder in 95% ethanol to make a 20 mM stock and diluted it with fly food to 400 µM. We collected adult female flies (2 days old) and transferred them to the 400 µM retinal food for 3–5 days before optogenetics experiments (**Fig. 4m,n**). To the 'Light On' group, we delivered 30 pulses of 0.5-s red-light (625 nm, 0.5Hz, 25µW·mm^{-2}) during CS^+ and CS^- exposures by using a collimated LED (M625L4, ThorLabs), whereas the 'Light Off' group of flies did not receive these pulses of illumination.

Computational Model

We computationally simulated a model of the neural circuitry that controls associative conditioning-induced aversive behaviors in *Drosophila*. The model characterizes the interactions of KCs, MBONs and DANs in the 3 interconnected learning modules (γ1, α2 and α3) of the MB (**Fig. 5a**). The KCs sparsely encode the CS^+ and CS^- odor stimuli, and the DANs encode the electric shock punishments. Dopamine modulates the strengths of the synaptic connections between the KCs and the MBONs, thereby altering the strength of the associative memory. The MBONs gather signals from the KCs to control approach or avoidance motor behaviors (**Fig. 5a**). Our model uses a set of ordinary differential equations to capture how the MB neural activity patterns and synaptic weights change with time. The model thereby describes how associative information is stored and retrieved in the short-term (γ1 module) and long-term memory compartments (α2 and α3 modules) of the MB.

The **Supplementary Appendix** presents the differential equations in the model that characterize the neural spiking rates and synaptic weights. The network architecture (**Fig. 5a**) is based on the synaptic connections present in the fly brain connectome[32]. If the number of synapses between two neurons is <10 in the connectome, we set the corresponding synaptic weight term in the model to be zero. This approximation substantially reduced the number of parameters used in the model. We inferred the values of non-zero synaptic weights by parametric fits of the experimental data on neural spiking, without further consideration of the number of synapses between neurons.

Concurrent activation of KC and DAN modifies the synaptic weight of the KC to MBON connection according to an anti-Hebbian learning rule. The anti-Hebbian learning rule implies that the synaptic weight decreases if the punishment appears later than the odor; and the synaptic

weight increases if the punishment appears earlier than the odor, as shown in **Fig. 5b**. The dynamics of synaptic weights from KCs to MBONs can be described by the differential equations in Section 2 of the **Supplementary Appendix**.

The differential equations in Sections 1 and 2 of the **Supplementary Appendix** form a complete set that models the neural activity and synaptic weights in the three modules (γ1, α2 and α3) of the mushroom body. We simulated these differential equations using the MATLAB (Mathworks) function ode15s(), which solves the differential equations numerically. However, this approach is time-consuming and takes ~14 s to obtain results using each set of parameters. Therefore, we simplified the model using several approximations (see **Supplementary Appendix** for details): (1) We approximated the activation functions of KCs and DANs as linear functions; (2) We assumed that the membrane time-constants of KCs, DANs and MBONs ($\tau_{KC,i}$, $\tau_{MBON,j}$, and $\tau_{DAN,j}$) are sufficiently brief (~10 ms) to allow the spiking rates of KCs, DANs and MBONs to attain their steady-state values within associative conditioning and testing bouts; (3) We assumed that the resting intervals between training and testing bouts or between successive training bouts are much longer than the duration of the training and testing bouts (**Fig. 3a,d; Fig. 4l; Fig. 5i**), which allowed us to focus our analyses on discrete time points corresponding to the individual training and testing bouts; (4) We used time-averaged values of KC and DAN spiking rate changes to calculate the changes in the values of the synaptic weights between KCs and MBONs. With these approximations, we simplified the computational model into a recurrent set of equations (Section 3 of the **Supplementary Appendix**). The time needed to simulate each set of parameters for the simplified model was only ~0.02 s, a ~700-fold speedup over the time needed to simulate results for one parameter set of the full model.

By inputting the experimental conditions and model parameters ($\boldsymbol{\theta}$) into the simplified

recurrent equation model, we simulated the neural spiking rates of DANs and MBONs in our experiments. Then, we optimized the model's parameters by fitting the model outputs to our experimental data. (**Fig. 5c; Extended Data Fig. 9a,b**). We assumed that the measured spiking rates of neurons, under all experimental conditions, were governed by independent normal distributions. This assumption allowed us to estimate the optimized values of the model parameters and their confidence intervals (Section 4 and **Supplementary Table 1** in the **Supplementary Appendix**). Using the model and its optimized parameters, we predicted the neural firing rates and their confidence intervals for experiments that had not yet been done. These predictions well matched the subsequent experimental results (**Fig. 5g–k; Extended Data Fig. 9**).

Statistical analyses

We performed all statistical analyses using MATLAB (v2018b and v2020b; Mathworks) software. We chose sample sizes using our own and published empirical measurements to estimate effect magnitudes. For statistical testing, we performed non-parametric Kruskal-Wallis and Friedman ANOVAs, to avoid making assumptions about normal distributions or equal variances across groups. To perform *post hoc* pairwise statistical comparisons, we used two-sided versions of the Mann-Whitney U-test or the Wilcoxon signed-rank test with a Holm-Bonferroni correction for multiple comparisons.

Data availability

The data that support the findings of this study are available from the corresponding authors upon reasonable request.

Code availability

We used open-source image algorithms for motion correction (NoRMCorre[87]; https://github.com/flatironinstitute/NoRMCorre) and for image denoising (BM3D[88]; https://webpages.tuni.fi/foi/GCF-BM3D). We used the PyTorch[89] machine learning framework (v1.7.1; www.pytorch.org) for classification analysis. Matlab codes underlying the data analysis and the computation model are available upon request from the corresponding authors.

References

1. Choi, G. B. *et al.* Driving opposing behaviors with ensembles of piriform neurons. *Cell* **146**, 1004–1015 (2011).
2. Root, C. M., Denny, C. A., Hen, R. & Axel, R. The participation of cortical amygdala in innate, odour-driven behaviour. *Nature* **515**, 269–273 (2014).
3. Ramírez-Lugo, L., Peñas-Rincón, A., Ángeles-Durán, S. & Sotres-Bayon, F. Choice Behavior Guided by Learned, But Not Innate, Taste Aversion Recruits the Orbitofrontal Cortex. *J. Neurosci.* **36**, 10574–10583 (2016).
4. Sosulski, D. L., Bloom, M. L., Cutforth, T., Axel, R. & Datta, S. R. Distinct representations of olfactory information in different cortical centres. *Nature* **472**, 213–216 (2011).
5. Isosaka, T. *et al.* Htr2a-Expressing Cells in the Central Amygdala Control the Hierarchy between Innate and Learned Fear. *Cell* **163**, 1153–1164 (2015).
6. Paoli, M. & Galizia, G. C. Olfactory coding in honeybees. *Cell Tissue Res.* **383**, 35–58 (2021).
7. Marin, E. C., Jefferis, G. S. X. E., Komiyama, T., Zhu, H. & Luo, L. Representation of the glomerular olfactory map in the Drosophila brain. *Cell* **109**, 243–255 (2002).
8. Eschbach, C. *et al.* Recurrent architecture for adaptive regulation of learning in the insect brain. *Nat. Neurosci.* **23**, 544–555 (2020).
9. Eschbach, C. *et al.* Circuits for integrating learned and innate valences in the insect brain. *Elife* **10**, (2021).
10. Arber, S. & Costa, R. M. Networking brainstem and basal ganglia circuits for movement. *Nat. Rev. Neurosci.* **23**, 342–360 (2022).
11. Tye, K. M. Neural Circuit Motifs in Valence Processing. *Neuron* **100**, 436–452 (2018).

12. Heisenberg, M. Mushroom body memoir: from maps to models. *Nat. Rev. Neurosci.* **4**, 266–275 (2003).

13. Dolan, M.-J. *et al.* Communication from Learned to Innate Olfactory Processing Centers Is Required for Memory Retrieval in Drosophila. *Neuron* **100**, 651–668.e8 (2018).

14. Li, Q. & Liberles, S. D. Aversion and attraction through olfaction. *Curr. Biol.* **25**, R120–R129 (2015).

15. Schultz, W. Predictive reward signal of dopamine neurons. *J. Neurophysiol.* **80**, 1–27 (1998).

16. Schultz, W. Dopamine reward prediction-error signalling: a two-component response. *Nat. Rev. Neurosci.* **17**, 183–195 (2016).

17. Kim, H. R. *et al.* A Unified Framework for Dopamine Signals across Timescales. *Cell* **183**, 1600–1616.e25 (2020).

18. Watabe-Uchida, M. & Uchida, N. Multiple Dopamine Systems: Weal and Woe of Dopamine. *Cold Spring Harb. Symp. Quant. Biol.* **83**, 83–95 (2018).

19. Morrens, J., Aydin, Ç., Janse van Rensburg, A., Esquivelzeta Rabell, J. & Haesler, S. Cue-Evoked Dopamine Promotes Conditioned Responding during Learning. *Neuron* **106**, 142–153.e7 (2020).

20. Tian, J. *et al.* Distributed and Mixed Information in Monosynaptic Inputs to Dopamine Neurons. *Neuron* **91**, 1374–1389 (2016).

21. Engelhard, B. *et al.* Specialized coding of sensory, motor and cognitive variables in VTA dopamine neurons. *Nature* **570**, 509–513 (2019).

22. Aso, Y. *et al.* The neuronal architecture of the mushroom body provides a logic for associative learning. *Elife* **3**, e04577 (2014).

23. Aso, Y. & Rubin, G. M. Dopaminergic neurons write and update memories with cell-type-specific rules. *Elife* **5**, (2016).

24. Hige, T., Aso, Y., Modi, M. N., Rubin, G. M. & Turner, G. C. Heterosynaptic Plasticity Underlies Aversive Olfactory Learning in Drosophila. *Neuron* **88**, 985–998 (2015).

25. Cohn, R., Morantte, I. & Ruta, V. Coordinated and Compartmentalized Neuromodulation Shapes Sensory Processing in Drosophila. *Cell* **163**, 1742–1755 (2015).

26. Siju, K. P. *et al.* Valence and State-Dependent Population Coding in Dopaminergic Neurons in the Fly Mushroom Body. *Curr. Biol.* **30**, 2104–2115.e4 (2020).

27. Vrontou, E. *et al.* Response competition between neurons and antineurons in the mushroom body. *Curr. Biol.* **31**, 4911–4922.e4 (2021).

28. McCurdy, L. Y., Sareen, P., Davoudian, P. A. & Nitabach, M. N. Dopaminergic mechanism underlying reward-encoding of punishment omission during reversal learning in Drosophila. *Nat. Commun.* **12**, 1115 (2021).

29. Takemura, S.-Y. *et al.* A connectome of a learning and memory center in the adult Drosophila brain. *Elife* **6**, (2017).

30. Li, F. *et al.* The connectome of the adult Drosophila mushroom body provides insights into function. *Elife* **9**, (2020).

31. Raman, D. V. & O'Leary, T. Frozen algorithms: how the brain's wiring facilitates learning. *Curr. Opin. Neurobiol.* **67**, 207–214 (2021).

32. Scheffer, L. K. *et al.* A connectome and analysis of the adult Drosophila central brain. *Elife* **9**, (2020).

33. Huang, C. *et al.* Long-term optical brain imaging in live adult fruit flies. *Nat. Commun.* **9**, 872 (2018).

34. Chen, T.-W. *et al.* Ultrasensitive fluorescent proteins for imaging neuronal activity. *Nature* **499**, 295–300 (2013).

35. Vanwalleghem, G., Constantin, L. & Scott, E. K. Calcium Imaging and the Curse of Negativity. *Front. Neural Circuits* **14**, 607391 (2020).

36. Nakajima, R. & Baker, B. J. Mapping of excitatory and inhibitory postsynaptic potentials of neuronal populations in hippocampal slices using the GEVI, ArcLight. *J. Phys. D Appl. Phys.* **51**, (2018).

37. Gong, Y. *et al.* High-speed recording of neural spikes in awake mice and flies with a fluorescent voltage sensor. *Science* vol. 350 1361–1366 (2015).

38. Kannan, M. *et al.* Fast, in vivo voltage imaging using a red fluorescent indicator. *Nat. Methods* **15**, 1108–1116 (2018).

39. Kannan, M. *et al.* Dual polarity voltage imaging reveals subthreshold dynamics and concurrent spiking patterns of multiple neuron-types. *bioRxiv* 2021.10.13.463730 (2021) doi:10.1101/2021.10.13.463730.

40. Sinha, S. *et al.* Laser microsurgery for two-photon imaging in fruit flies. *Optics in the Life Sciences* (2011) doi:10.1364/ntm.2011.nmc6.

41. Sinha, S. *et al.* High-speed laser microsurgery of alert fruit flies for fluorescence imaging of neural activity. *Proceedings of the National Academy of Sciences* vol. 110 18374–18379 (2013).

42. Wilt, B. A., Fitzgerald, J. E. & Schnitzer, M. J. Photon shot noise limits on optical detection of neuronal spikes and estimation of spike timing. *Biophys. J.* **104**, 51–62 (2013).

43. Stuart, G., Spruston, N., Sakmann, B. & Häusser, M. Action potential initiation and backpropagation in neurons of the mammalian CNS. *Trends Neurosci.* **20**, 125–131 (1997).

44. Markram, H., Lübke, J., Frotscher, M. & Sakmann, B. Regulation of synaptic efficacy by coincidence of postsynaptic APs and EPSPs. *Science* **275**, 213–215 (1997).

45. Kim, Y.-C., Lee, H.-G. & Han, K.-A. Classical reward conditioning in Drosophila melanogaster. *Genes Brain Behav.* **6**, 201–207 (2007).

46. Krashes, M. J. & Waddell, S. Rapid consolidation to a radish and protein synthesis-dependent long-term memory after single-session appetitive olfactory conditioning in Drosophila. *J. Neurosci.* **28**, 3103–3113 (2008).

47. Huang, C., Wang, P., Xie, Z., Wang, L. & Zhong, Y. The differential requirement of mushroom body α/β subdivisions in long-term memory retrieval in Drosophila. *Protein Cell* **4**, 512–519 (2013).

48. Hattori, D. *et al.* Representations of Novelty and Familiarity in a Mushroom Body Compartment. *Cell* **169**, 956–969.e17 (2017).

49. Hige, T., Aso, Y., Rubin, G. M. & Turner, G. C. Plasticity-driven individualization of olfactory coding in mushroom body output neurons. *Nature* **526**, 258–262 (2015).

50. Zhao, C. *et al.* Predictive olfactory learning in Drosophila. *Sci. Rep.* **11**, 6795 (2021).

51. Bennett, J. E. M., Philippides, A. & Nowotny, T. Learning with reinforcement prediction errors in a model of the Drosophila mushroom body. *Nat. Commun.* **12**, 2569 (2021).

52. Springer, M. & Nawrot, M. P. A mechanistic model for reward prediction and extinction learning in the fruit fly. *eNeuro* (2021) doi:10.1523/ENEURO.0549-20.2021.

53. Jiang, L. & Litwin-Kumar, A. Models of heterogeneous dopamine signaling in an insect learning and memory center. *PLoS Comput. Biol.* **17**, e1009205 (2021).

54. Gkanias, E., McCurdy, L. Y., Nitabach, M. N. & Webb, B. The incentive circuit: memory dynamics in the mushroom body of Drosophila melanogaster. *bioRxiv* 2021.06.11.448104

(2021) doi:10.1101/2021.06.11.448104.

55. Tully, T. & Quinn, W. G. Classical conditioning and retention in normal and mutantDrosophila melanogaster. *Journal of Comparative Physiology A* **157**, 263–277 (1985).

56. Tully, T., Preat, T., Boynton, S. C. & Del Vecchio, M. Genetic dissection of consolidated memory in Drosophila. *Cell* **79**, 35–47 (1994).

57. Huang, C. *et al.* A permissive role of mushroom body α/β core neurons in long-term memory consolidation in Drosophila. *Curr. Biol.* **22**, 1981–1989 (2012).

58. Aso, Y. *et al.* Mushroom body output neurons encode valence and guide memory-based action selection in Drosophila. *Elife* **3**, e04580 (2014).

59. Krashes, M. J., Keene, A. C., Leung, B., Armstrong, J. D. & Waddell, S. Sequential use of mushroom body neuron subsets during drosophila odor memory processing. *Neuron* **53**, 103–115 (2007).

60. Jacob, P. F. & Waddell, S. Spaced Training Forms Complementary Long-Term Memories of Opposite Valence in Drosophila. *Neuron* **106**, 977–991.e4 (2020).

61. Yu, D., Akalal, D.-B. G. & Davis, R. L. Drosophila alpha/beta mushroom body neurons form a branch-specific, long-term cellular memory trace after spaced olfactory conditioning. *Neuron* **52**, 845–855 (2006).

62. Berry, J. A., Cervantes-Sandoval, I., Chakraborty, M. & Davis, R. L. Sleep Facilitates Memory by Blocking Dopamine Neuron-Mediated Forgetting. *Cell* **161**, 1656–1667 (2015).

63. Sweeney, S. T., Broadie, K., Keane, J., Niemann, H. & O'Kane, C. J. Targeted expression of tetanus toxin light chain in Drosophila specifically eliminates synaptic transmission and causes behavioral defects. *Neuron* **14**, 341–351 (1995).

64. Liu, W. W. & Wilson, R. I. Glutamate is an inhibitory neurotransmitter in the Drosophila olfactory system. *Proc. Natl. Acad. Sci. U. S. A.* **110**, 10294–10299 (2013).

65. Smolen, P., Zhang, Y. & Byrne, J. H. The right time to learn: mechanisms and optimization of spaced learning. *Nat. Rev. Neurosci.* **17**, 77–88 (2016).

66. Mery, F. & Kawecki, T. J. A cost of long-term memory in Drosophila. *Science* **308**, 1148 (2005).

67. Claridge-Chang, A. *et al.* Writing memories with light-addressable reinforcement circuitry. *Cell* **139**, 405–415 (2009).

68. Galili, D. S. *et al.* Converging circuits mediate temperature and shock aversive olfactory conditioning in Drosophila. *Curr. Biol.* **24**, 1712–1722 (2014).

69. Masek, P., Worden, K., Aso, Y., Rubin, G. M. & Keene, A. C. A dopamine-modulated neural circuit regulating aversive taste memory in Drosophila. *Curr. Biol.* **25**, 1535–1541 (2015).

70. Villar, M. E. *et al.* Different dopaminergic neurons signal absolute and relative aversive value in the Drosophila mushroom body. *bioRxiv* 2022.02.02.478814 (2022) doi:10.1101/2022.02.02.478814.

71. Liu, C. *et al.* A subset of dopamine neurons signals reward for odour memory in Drosophila. *Nature* **488**, 512–516 (2012).

72. Burke, C. J. *et al.* Layered reward signalling through octopamine and dopamine in Drosophila. *Nature* **492**, 433–437 (2012).

73. Berke, J. D. What does dopamine mean? *Nat. Neurosci.* **21**, 787–793 (2018).

74. Faghihi, F., Moustafa, A. A., Heinrich, R. & Wörgötter, F. A computational model of conditioning inspired by Drosophila olfactory system. *Neural Netw.* **87**, 96–108 (2017).

75. Wessnitzer, J., Young, J. M., Armstrong, J. D. & Webb, B. A model of non-elemental olfactory learning in Drosophila. *J. Comput. Neurosci.* **32**, 197–212 (2012).

76. Smith, D., Wessnitzer, J. & Webb, B. A model of associative learning in the mushroom body. *Biol. Cybern.* **99**, 89–103 (2008).

77. Bjork, R. A. & Allen, T. W. The spacing effect: Consolidation or differential encoding? *Journal of Verbal Learning and Verbal Behavior* vol. 9 567–572 (1970).

78. Appleton-Knapp, S. L., Bjork, R. A. & Wickens, T. D. Examining the Spacing Effect in Advertising: Encoding Variability, Retrieval Processes, and Their Interaction. *Journal of Consumer Research* vol. 32 266–276 (2005).

79. Cepeda, N. J., Pashler, H., Vul, E., Wixted, J. T. & Rohrer, D. Distributed practice in verbal recall tasks: A review and quantitative synthesis. *Psychol. Bull.* **132**, 354–380 (2006).

80. Sutton, M. A., Ide, J., Masters, S. E. & Carew, T. J. Interaction between amount and pattern of training in the induction of intermediate- and long-term memory for sensitization in aplysia. *Learn. Mem.* **9**, 29–40 (2002).

81. Gerber, B., Wüstenberg, D., Schütz, A. & Menzel, R. Temporal determinants of olfactory long-term retention in honeybee classical conditioning: nonmonotonous effects of the training trial interval. *Neurobiol. Learn. Mem.* **69**, 71–78 (1998).

82. Pagani, M. R., Oishi, K., Gelb, B. D. & Zhong, Y. The phosphatase SHP2 regulates the spacing effect for long-term memory induction. *Cell* **139**, 186–198 (2009).

83. Gkanias, E., McCurdy, L. Y., Nitabach, M. N. & Webb, B. An incentive circuit for memory dynamics in the mushroom body of Drosophila melanogaster. *Elife* **11**, (2022).

84. Savall, J., Ho, E. T. W., Huang, C., Maxey, J. R. & Schnitzer, M. J. Dexterous robotic manipulation of alert adult Drosophila for high-content experimentation. *Nat. Methods* **12**,

657–660 (2015).

85. Gaudry, Q., Hong, E. J., Kain, J., de Bivort, B. L. & Wilson, R. I. Asymmetric neurotransmitter release enables rapid odour lateralization in Drosophila. *Nature* **493**, 424–428 (2013).

86. Clark, D. A., Bursztyn, L., Horowitz, M. A., Schnitzer, M. J. & Clandinin, T. R. Defining the computational structure of the motion detector in Drosophila. *Neuron* **70**, 1165–1177 (2011).

87. Pnevmatikakis, E. A. & Giovannucci, A. NoRMCorre: An online algorithm for piecewise rigid motion correction of calcium imaging data. *J. Neurosci. Methods* **291**, 83–94 (2017).

88. Dabov, K., Foi, A., Katkovnik, V. & Egiazarian, K. Image denoising by sparse 3-D transform-domain collaborative filtering. *IEEE Trans. Image Process.* **16**, 2080–2095 (2007).

89. Paszke, A. *et al.* PyTorch: An imperative style, high-performance deep learning library. *Adv. Neural Inf. Process. Syst.* **32**, (2019).

90. Cortes, C. & Vapnik, V. Support-vector networks. *Mach. Learn.* **20**, 273–297 (1995).

91. Kingma, D. P. & Ba, J. Adam: A Method for Stochastic Optimization. *arXiv [cs.LG]* (2014).

92. Klapoetke, N. C. *et al.* Independent optical excitation of distinct neural populations. *Nat. Methods* **11**, 338–346 (2014).

Supplementary Files

This is a list of supplementary files associated with this preprint. Click to download.

- FinalAppendix.pdf
- ExtendedDataTable1.pdf
- Video1.mp4
- Video2.mp4